Motion Detection and Correction in Magnetic Resonance Imaging

Julian R. Maclaren

Department of Electrical and Computer Engineering

A thesis presented for the degree of
Doctor of Philosophy

University of Canterbury
Christchurch, New Zealand
January 2008

Abstract

Magnetic resonance imaging (MRI) is a non-invasive technique used to produce high-quality images of the interior of the human body. Compared to other imaging modalities, however, MRI requires a relatively long data acquisition time to form an image. Patients often have difficulty staying still during this period. This is problematic as motion produces artifacts in the image.

This thesis explores the methods of imaging a moving object using MRI. Testing is performed using simulations, a moving phantom, and human subjects. Several strategies developed to avoid motion artifact problems are presented. Emphasis is placed on techniques that provide motion correction without penalty in terms of acquisition time.

The most significant contribution presented is the development and assessment of the 'TRELLIS' pulse sequence and reconstruction algorithm. TRELLIS is a unique approach to motion correction in MRI. Orthogonal overlapping strips fill *k*-space and phase-encode and frequency-encode directions are alternated such that the frequency-encode direction always runs lengthwise along each strip. The overlap between pairs of orthogonal strips is used for signal averaging and to produce a system of equations that, when solved, quantifies the rotational and translational motion of the object. Acquired data is then corrected using this motion estimation. The advantage of TRELLIS over existing techniques is that *k*-space is sampled uniformly and all collected data is used for both motion detection and image reconstruction.

This thesis presents a number of other contributions: a proposed means of motion correction using parallel imaging; an extension to the phase-correlation method for determining displacement between two objects; a metric to quantify the level of motion artifacts; a moving phantom; a physical version of the ubiquitous Shepp-Logan head phantom; a motion resistant data acquisition technique; and a means of correcting for T_2 blurring artifacts.

Acknowledgements

During my time at the University of Canterbury, I have benefited from the guidance and support of Assoc. Prof. Phil Bones, Prof. Rick Millane, and Dr Richard Watts.

Phil's encouragement and enthusiasm have helped make my experience as a PhD student very enjoyable. I am extremely grateful for this. Phil and I share a interest in outdoor pursuits and, as well as working together, we have found time for several climbing trips: most recently, a side excursion from a conference in Lyon to Chamonix and up Mt Blanc. Rick has made numerous astute observations about my research and, in particular, his assistance with my published work has been invaluable. My writing style has improved significantly as the result of his suggestions. Lastly, (with a surname beginning with 'W', he gets this often) I would like to thank Richard for his continual support. His expertise on MRI has been essential to the success of this work. I have also enjoyed the time spent with Richard in Seattle and Berlin, attending meetings of the ISMRM.

Numerous others – too many to mention here – have been of great assistance to me. Gareth Leeper, from Christchurch Radiology Group, was very understanding and helpful when I wanted to use his scanner to image various strange objects. Thanks also to Bing Wu, who is partly responsible for the work reported in Appendix A.

I am grateful for the financial support I obtained from the Tertiary Education Commission through a Top Achiever Doctoral Scholarship. I also appreciate the assistance of the Canterbury Branch of the Royal Society, for helping to fund my attendance to a conference in Europe in 2005, and the International Society for Magnetic Resonance in Medicine (ISMRM), for student stipends to attend their meetings in 2006 and 2007.

Finally, I would like to thank my family and friends for their support. They were tolerant enough to allow me to explain MRI to them on numerous occasions, despite presumably not sharing my level of enthusiasm for the subject!

Contents

Abbreviations

Abbreviations used in this thesis are listed here for easy reference.

2DFT	two-dimensional Fourier transform
CNR	contrast-to-noise ratio
CT	computed tomography
DBE	difference in background energy
DFT	discrete Fourier transform
DWI	diffusion-weighted imaging
EPI	echo planar imaging
EPIC	environment for pulse programming in C
FE	frequency encode
FFT	fast Fourier transform
FID	free induction decay
fMRI	functional magnetic resonance imaging
FOV	field-of-view
FSE	fast spin echo
GE	General Electric (Medical Systems)
GRAPPA	generalized autocalibrating partially parallel acquisitions
GRASE	gradient- and spin-echo
IEEE	Institute of Electrical and Electronic Engineers
ISMRM	International Society for Magnetic Resonance in Medicine
MR	magnetic resonance
MRI	magnetic resonance imaging
MSE	mean squared error
NMR	nuclear magnetic resonance
NMSE	normalised mean squared error
PD	proton density
PE	phase encode
PET	positron emission tomography
PROPELLER	periodically rotated overlapping parallel lines with enhanced reconstruction

PSF	point spread function
RF	radio frequency
SENSE	sensitivity encoding
SMASH	simultaneous acquisition of spatial harmonics
SNR	signal-to-noise ratio
TRELLIS	translation and rotation estimation using linear least-squares and interleaved strips

Chapter 1

Introduction

This chapter contains three sections: an overview of the research and its objectives; a summary of the author's contributions, including a list of relevant publications; and a guide to the structure of this thesis.

1.1 Overview and objectives

Motion of the patient during an MRI scan can cause severe artifacts in the final image. Such motion is commonplace as MRI requires a long data acquisition time to form an image, typically of the order of minutes. Even healthy volunteers can have difficulty remaining motionless for the required time. The situation is exacerbated by the claustrophobic environment within the scanner which makes many people feel anxious, resulting in more motion. Some groups of patients, such as very young children or patients with tremors, are especially problematic.

Numerous 'partial solutions' to this problem are available: physical restraints and sedation are used frequently; rapid imaging techniques and other sequences less prone to the effects of motion are common; and various motion correction approaches have become widespread. Unfortunately, all such methods currently in use have their disadvantages. Furthermore, as technology improves, the resolution in MRI improves and the sensitivity to motion increases.

The aim of the research presented here is to contribute to a better understanding of how motion artifacts in MRI might be ameliorated. This thesis describes the development, testing and evaluation of novel algorithms to detect and compensate for motion effects in MRI. In particular, the goal is to assess the feasibility of an algorithm that can provide motion correction without penalty in terms of acquisition time. Acquisition time is of great im-

portance in MRI, not only for reasons of patient comfort, but also due to the high cost of scanner time.

1.2 Thesis contributions

The most significant contribution to the field made by this thesis is the **TRELLIS algorithm.** TRELLIS adopts a novel approach to motion correction and the results presented demonstrate that this method is feasible. The technique has several advantages over existing methods, as are described. Other contributions include:

The extension to the phase-correlation method. This has been developed in order to quantify translational motion in MRI. It also has applications in areas other than MRI, however, when the displacement of an object between two images must be determined with subpixel accuracy.

The DBE metric. A numerical measure is needed to indicate the severity of motion artifacts present in an image. Provided that a reference image is available and the object is of limited extent, it is shown that a measure related to the amount of energy outside the support can be used to objectively assess the presence of motion-induced artifacts.

The physical Shepp-Logan phantom. The numerical version of the Shepp-Logan head phantom is widely used in computer simulations for medical imaging. A physical Shepp-Logan head phantom has been constructed to validate simulations performed using the numerical version.

A means of correcting T_2 blurring artifacts. A novel approach to reducing the effect of T_2 decay is presented. This complements the particular data acquisition strategy used by the TRELLIS algorithm.

Other, more minor, contributions can be found throughout this thesis. These include innovations such as a **pneumatically operated moving phantom** and a **system of simulating motion effects in MRI**. Such developments are by no means unique; however, the approach taken may well be original and of benefit to others in the future. Also worthy of mention, is the **asymmetric sequential acquisition**, a motion-resistant sequence related to the TRELLIS algorithm.

Finally, the results of a brief experiment to test an approach using **parallel imaging for motion correction** are reported. Results are promising, and this is a strong candidate for future work.

The following publications have resulted from this work:

- J. R. Maclaren, P. J. Bones, R. P. Millane, and R. Watts,"MRI with TRELLIS: a novel approach to motion correction", *Magnetic Resonance Imaging*, in press.
- Julian R. Maclaren, Philip J. Bones, R. P. Millane, and Richard Watts,"A modified view ordering for artifact reduction in MRI", In *Proceedings of the IEEE Engineering in Medicine and Biology Society*, Lyon, 2007, pp. 2053–2056.
- Philip J. Bones and Julian R. Maclaren, "Improved bulk rotation detection and correction in MRI", In *Proceedings of the IEEE Engineering in Medicine and Biology Society*, Lyon, 2007, pp. 2106–2109.
- P. J. Bones and J. R. Maclaren, "Artifact reduction in magnetic resonance imaging", In *Signal Recovery and Synthesis on CD-ROM*, The Optical Society of America, SMA6, 2007.
- J. Maclaren, P. Bones, R. Millane, and R. Watts, "TRELLIS motion correction: initial results in vivo", In *Proceedings of the International Society for Magnetic Resonance in Medicine*, Berlin, 2007, p. 3426.
- P. J. Bones, J. R. Maclaren, R. P. Millane, and R. Watts, "Quantifying and correcting motion artifacts in MRI", In *Image Reconstruction from Incomplete Data IV*, Proceedings SPIE, vol. 6316, 2006, pp. 6316–08.
- J. Maclaren, P. Bones, R. Millane, and R. Watts, "TRELLIS MRI: a novel approach to motion correction", In *Proceedings of the International Society for Magnetic Resonance in Medicine*, Seattle, 2006, p. 3194.
- P. Bones, J. Maclaren, R. Millane, and R. Watts, "An extension to the phase-correlation method applied to MRI motion correction", In *Australasian Physical & Engineering Sciences in Medicine*, vol. 28(4), 2005, p. 286.
- J. R. Maclaren, P. J. Bones, R. P. Millane, and R. Watts, "Correcting motion artifacts in magnetic resonance images", In *Proceedings of Image and Vision Computing New Zealand*, Dunedin, 2005, pp. 120–125.
- J. R. Maclaren, P. J. Bones, R. P. Millane, and R. Watts, "Correction of translational motion artifacts in magnetic resonance imaging", In *Proceedings of the Fifth IASTED International Conference on Visualization, Imaging, and Image Processing*, Benidorm, 2005, pp. 448–452.

The work described in this thesis has been also been presented by the author in various forms:

- Poster presentation, "A modified view ordering for artifact reduction in MRI", presented at the 29th Annual International Conference of the IEEE EMBS, Cité Internationale, Lyon, France, 23–26 August, 2007.
- Poster presentation, "TRELLIS MRI: initial results in vivo", presented at the 15th Scientific Meeting, of the International Society for Magnetic Resonance in Medicine, 21–25 May 2007.
- Oral presentation, "Keep still please: the correction of motion artifacts in MRI", Departmental Seminar, Department of Electrical and Computer Engineering, University of Canterbury, 9 March 2007.

- Oral presentation, "Keep still please: the correction of motion artifacts in MRI", IET Present around the World competition (NZ final), 24 February 2007.
- Oral presentation, "Motion correction in MRI", Van der Veer Brain Institute for Parkinson's and Brain Research, Brain Research Forum No. 19, 4 December 2006.
- Oral presentation, "The correction of motion artifacts in magnetic resonance imaging", Australasian High Energy and Medical Physics Conference, 17–20 October 2006.
- Oral presentation, "Keep still please: the correction of motion artifacts in MRI", IET (Canterbury Branch) short papers competition, 14 September 2006.
- Oral presentation, "Correcting motion artifacts in magnetic resonance images", ENEL619 lecture, 14 August 2006.
- Oral presentation, "Correcting motion artifacts in magnetic resonance images", IEEE (New Zealand South Section), Postgraduate Presentations, 19 July 2006.
- Poster presentation, "TRELLIS MRI: a novel approach to motion correction", presented at the 14th Scientific Meeting of the International Society for Magnetic Resonance in Medicine, 6–12 May 2006.
- Oral presentation, "Correcting motion artifacts in magnetic resonance images", presented at Image and Vision Computing New Zealand, University of Otago, Dunedin, New Zealand, 28–29 November 2005.
- Oral presentation, "The correction of translational motion artifacts in magnetic resonance imaging", presented at the Fifth IASTED International Conference on Visualization, Imaging, and Image Processing, Benidorm, Spain, 7–9 September 2005.

1.3 Thesis structure

The reader is assumed to have a basic knowledge of image processing but not a background in magnetic resonance imaging; hence, fundamental principles of MRI are presented in this thesis. Chapter 2, *Magnetic Resonance Imaging*, introduces these essential background concepts, including a brief introduction to MR physics and the principles behind image reconstruction. An outline of the historical development of MRI is also presented.

Chapter 3, *Motion in MRI*, examines the problem of imaging a moving object. Background literature is reviewed and current correction techniques are explained. The chapters that follow are *MR Phantoms* and *MR Image Artifact Metrics*. Here, tools to help assess motion correction techniques are developed. First, *MR Phantoms* discusses how motion can be both simulated and generated in practice in a repeatable and reliable fashion. Then *MR Image Artifact Metrics* reports on the development of techniques to provide a numerical and impartial means of assessing the resulting images.

Chapters 6–8 present a new motion-correction pulse sequence and reconstruction algorithm, known as TRELLIS. Chapter 6, *TRELLIS: A Motion Correction Algorithm*, describes the workings of this new technique. Chapter 7, *TRELLIS: Simulations*, presents the results of a number of computer simulations performed to test the algorithm. Chapter 8, *TRELLIS: Implementation and Results*, then documents the implementation of the algorithm on an MRI scanner. Results obtained using this implementation are presented here also.

Chapter 9, *Reduced Motion Sensitivity*, presents a new pulse sequence that is resistant to the effects of motion. This is actually a 'by-product' of the TRELLIS algorithm, but stands alone as provides a means of reducing motion effects without any post-processing of data.

A summary of the work presented in this thesis is provided in the *Conclusion* chapter, as are recommendations for future research.

Appendix A, *Motion Correction using Parallel Imaging*, suggests an alternative technique to TRELLIS. This uses multiple receive coils and existing parallel imaging reconstruction algorithms to correct for motion. Initial results are presented. Appendix B describes a brief attempt to quantify the head motion of human subjects using an optical tracking system. Appendices C provides a mathematical derivation of the T_2 deblurring approach used in this thesis. Finally, Appendix D contains the information and consent forms used when conducting experiments with human subjects.

Chapter 2

Magnetic Resonance Imaging

The history, physics and imaging principles of MRI are discussed in this chapter with an emphasis on information that will aid understanding of the work presented later in this thesis.

For further general information, a vast amount of literature is available. A lucid description of MRI from a clinical perspective is given in McRobbie et al. [1]; this would be a good choice for a reader with little existing knowledge of the subject. A free alternative is an online book by J. Hornak, which explains the basic principles of MRI [2]. This is a useful reference, mainly because it is so readily available. In the author's opinion, however, Nishimura's *Principles of Magnetic Resonance Imaging* [3] gives by far the best introduction.[1] It is clear and concise without glossing over the more technical details. For specific information about a particular pulse sequence (more about these later), the *Handbook of MRI Pulse Sequences* by Bernstein et al. [4] is indispensable.

A number of works by the original pioneers of MRI – who are mentioned in the following section – are also available. A good summary is given by Mansfield's Nobel Lecture [5] which makes interesting reading. In print, Liang and Lauterbur [6] is a good description of MRI from a signal processing perspective.

2.1 History of MRI

MRI has an interesting history. For this reason, a summary of its development over the past fifty years or so is included here. This section also serves as a gentle introduction to MRI for the reader who has no previous experience in the field. The following is largely

[1] At the time of writing, this book is out of print, but it can be ordered directly from the author (Prof. Nishimura, Stanford University) for a very reasonable price.

taken from an essay by the author, *MRI: The product of a century of progress*, submitted to the Institute of Engineering and Technology (IET) 'Write Around the World' Competition.

The ability to see inside the human body is a miracle of modern technology. Historically, the best a doctor could do to visualise the internal organs was to prod the patient from the surface or to cut them open and look inside. In some cases these were valid and effective techniques, although often distressing for the subject. Even early imaging techniques were very invasive. For example, a procedure called 'pneumoencephalography' was used until recently. This involved draining cerebrospinal fluid from around the brain and replacing it with air to improve contrast in an X-ray image. This was very unpleasant for the patient. Fortunately, today we have alternatives: magnetic resonance imaging (MRI) is one of these.

The development of MRI has been a global effort. Key concepts have come from scientists and engineers from the UK, the USA, France, Germany, Austria and Switzerland as well as other parts of the world. The scientific understanding and engineering capability built up over the last hundred years has come together to make MRI possible. The combination of powerful computers and the physical phenomenon of nuclear magnetic resonance (NMR) has opened doors that we would once never have believed existed.

2.1.1 The early stages

One of the earliest contributors to the field of MRI was Joseph Fourier, a French mathematician and physicist. It was he who proposed, in 1822, that a function could be represented by a series of sinusoids. The resulting mathematical transformation, later named the Fourier transform, forms the basis of MRI today. At the time of Fourier (who was an important official in Napoleon's regime [7]), the concept of imaging the human brain simply did not exist. Fourier could not have had the slightest inkling where his ideas would lead, although he knew he had developed a powerful new tool.

Many years later, in 1895, German physicist Wilhelm Röntgen (Fig. 2.1) discovered X-rays and, in 1901, received the first Nobel Prize in Physics. Although this discovery did not directly lead to MRI, it was the beginning of the new era of medical imaging. From then on, it no longer required such a leap of imagination to consider using alternative tools for such a purpose. This 'conceptual jump' often delays the implementation of new technology.

The first real step towards MRI was Austrian physicist Wolfgang Pauli's prediction of the existence of nuclear spin in 1924. Nuclear spin is a concept central to the development of MRI.[2] Around 20 years later, Isidor Isaac Rabi (also originally from Austria) received the

[2]Spin is a fundamental property possessed by protons, neutrons and electrons although the term is a little confusing: in reality, it has nothing to do with something actually 'spinning around'. Nevertheless, this is a useful concept whenever MRI needs to be explained simply.

(a) (b)

Figure 2.1 Early medical imaging: (a) Wilhelm Röntgen and (b) one of his original X-ray images (taken 23 January 1896).

Nobel Prize in Physics for his method of measuring this spin in molecular beams and thus determining the magnetic properties of atoms. His ideas were revolutionary for chemical analysis and provided a crucial stepping stone in the development of MRI.

In 1946, nuclear magnetic resonance (NMR) in liquids and solids was independently observed by both Felix Bloch (Swiss) and Edward Purcell (American) [8, 9]. They discovered that a signal is emitted from a sample in a magnetic field irradiated with electromagnetic energy of a particular frequency. In 1952, they both received the Nobel prize for their efforts. At the time, an influential newspaper was quoted as saying:

> *[Nuclear magnetic precession] won't revolutionize industry or help the housewife* - Boston Herald, 1952 [1]

The Boston Herald was mistaken: NMR has revolutionised several branches of science and changed our daily lives (although most people don't realise it). This is not only due to MRI, but also thanks to its power as a chemical analysis tool – a chemistry laboratory would now not be considered complete without an NMR machine. Discoveries relating to NMR are now responsible for a total of six Nobel prizes across three disciplines: chemistry, physics and medicine.

Nuclear magnetic resonance, as used in MRI, can be explained using a simple analogy, depicted in Fig. 2.2. Consider a hydrogen nucleus (a single proton in a hydrogen atom). Under a strong magnetic field, this proton aligns itself parallel to the field, much the way a spinning top aligns itself vertically under the influence of the Earth's gravitational field. If a spinning top is 'pushed' slightly, it begins to precess, that is, to wobble as it spins. This also applies to the proton. If another, smaller, magnetic field is applied via an electromagnetic pulse, the proton begins to precess around an axis aligned with the main magnetic field.[3]

[3]This description of NMR is an analogy only; a more complete explanation is given in Section 2.2.

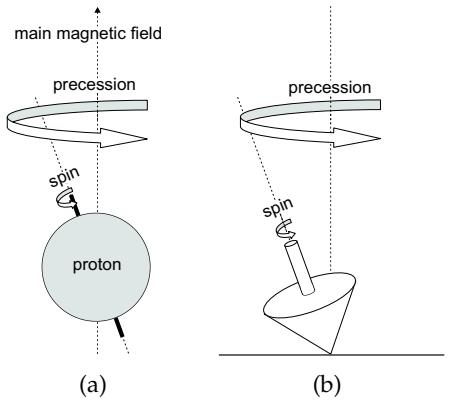

Figure 2.2 A precession analogy: (a) a spinning proton precessing about the axis of the main magnetic field; (b) a spinning top precessing about the axis of Earth's gravitational pull.

A spinning top might take around 1 s to precess about its axis of rotation, giving it a precession frequency of 1 Hz. In the case of the proton, however, the precession period is only a few nanoseconds at the field strengths commonly used in MRI. This produces a precession frequency in the order of megahertz – similar to that of FM radio transmission and in the radio frequency (RF) part of the electromagnetic spectrum. As the precessing proton also has a charge, a signal is emitted at the same frequency as the precession frequency (more on this in Section 2.3).

Although the emitted signal can be detected using a simple coil of wire, it dies away quickly with time as the collection of protons are all precessing at slightly different frequencies. Thus, their cumulative signal decays to zero as they get out of phase.

Then, in 1950, American physicist Erwin Hahn made a discovery that provided a simple solution to this problem. The phenomenon he discovered is known as *spin echo* (described in detail in Section 2.2). If you apply two RF pulses to a sample, you get a signal back, delayed by the time interval between the two pulses. This makes the signal from the proton much easier to measure than otherwise. Initially, Hahn thought this echo was caused by some sort of error in his experiment; however, he came to realise that the true cause was the rephasing of slowly dephasing spins. In the words of a well-known science fiction writer:

> *The most exciting phrase to hear in science, the one that heralds new discoveries, is not Eureka! (I found it!) but rather, "hmm.... that's funny...."* – Isaac Asimov

The application of NMR to the biological world started immediately when Bloch inserted his finger into his magnet and observed a large resonance signal [10]! In 1956, Erik Odeblad from Sweden published NMR studies of of living cells and excised animal tissue [11]. Odeblad continued working on tissues throughout the 1950s and 1960s. While he applied

NMR to a range of tissue types he never looked at cancerous tissue. In 1971, however, Raymond Damadian showed that the nuclear magnetic relaxation times of tissues and tumors differed in mice. This was a fundamental discovery in that NMR became known as not only a tool for chemistry but also one that could be used to detect disease. The US Patent Office granted Damadian a patent for the design shown in Fig. 2.3. Note that it is not an imaging device – its aim was purely to detect the presence of cancerous cells. His proposed method, however, has never successfully been implemented.

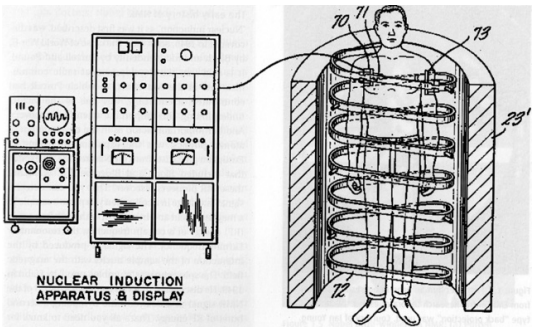

Figure 2.3 Damadian's invention for detecting cancer (US Patent and Trademark Office, patent number 3789832).

2.1.2 From NMR to MRI

Why was NMR used for so long in analytical chemistry before being applied to imaging? The problem was that an NMR signal could provide information about the type of material in a sample, but the exact location of the signal source was unknown. With no spatial information it is impossible to form an image.

Eventually a solution was devised. In the 1970s, Paul Lauterbur [12] (American), Richard Ernst (Swiss) and Peter Mansfield (British) all independently demonstrated the imaging potential of NMR, and MRI was born.[4] In 1978 the first image of a human head was taken. The key to this sudden burst of success was something known as *spatial encoding*. Spatial encoding is described in detail in Section 2.2.

Ernst received the Nobel Prize in Chemistry in 1991, and Lauterbur and Mansfield were awarded the Nobel Prize in Medicine in 2003 for 'their discoveries concerning magnetic resonance imaging'. The press release [13] went on to say: 'Paul Lauterbur ... discovered the possibility to create a two-dimensional picture by introducing gradients in the magnetic field. Peter Mansfield ... showed how the signals could be mathematically analysed, which made it possible to develop a useful imaging technique.' The decision to award Lauterbur and Mansfield the Nobel prize was the source of much controversy. The cause

[4] MRI was originally know as 'NMRI' (nuclear magnetic resonance imaging); however, the 'nuclear' was dropped from the name due to its unfortunate connotations at the time.

was not because Lauterbur and Mansfield were undeserving recipients, but because Damadian thought the prize should also have been awarded to him. Believing that he had been treated unfairly, he put full-page advertisements in a number of international newspapers protesting the decision. This controversy is recalled by many – even those who remember nothing else about MRI.

The first scanners reached the market by 1982 but only became widely available in the 1990s. By 2003 there were around 75 million scans performed per year using 10 000 MRI machines worldwide [2]. Fig. 2.4 shows a modern MRI scanner and an image.

(a) (b)

Figure 2.4 Modern MRI: (a) a scanner at St George's Radiology (Christchurch, New Zealand), and (b) an image of the author's brain acquired using it.

Today, MRI has gone beyond merely mapping physical structure. Knowledge of structure alone gives us only a tiny piece of the whole picture. This observation was also made many years ago:

> *We anatomists are like the porters of Paris, who are acquainted with the narrowest and most distant streets, but who know nothing of what takes place in the houses* – Bernard le Bovier de Fontenelle, French author and philosopher, 1657–1757

Now, it is possible to gain an idea of the function of organs as well, especially the brain and blood vessels. Functional MRI (fMRI) was developed around 1992 [14]. This technique, which 'highlights' active areas of the brain, has much to offer the field of neuroimaging. A more detailed description of the potential of MRI for neuroscience can be found in review articles such as [15].

2.2 Physics of NMR

Nuclear magnetic resonance, or NMR, is the physical phenomenon behind MRI. It can be described in a quantum mechanical sense, or classically, using the concept of precession as mentioned earlier. The quantum mechanical version is often used at the atomic scale as it can describe the behaviour of individual protons. For a large collection of nuclei, however, a classical description is more convenient and intuitive. Apart from the following paragraph, the classical approach is used here. For a quantum mechanical treatment, refer to [16].

Atoms containing an odd number of protons or neutrons possess a property called 'nuclear spin'. The atom most relevant to the human body is hydrogen (^{1}H) due to its abundance in water (H_2O) and in lipids. The (^{1}H) nucleus consists of only a single proton and thus has a net spin. Normally randomly orientated, this spin is quantised when placed in a magnetic field (see Fig. 2.5) and can adopt one of only two possible orientations: parallel or anti-parallel. The parallel state has a slightly lower energy associated with it and therefore more protons adopt this orientation. The exact ratio can be calculated using Boltzmann statistics and is dependent on the strength of the external magnetic field and the temperature [1]. At field strengths used in MRI, the difference between the two states is only a few protons per million. Each spin acts like a small magnetic dipole. Thus, a net magnetisation vector, denoted **M**, is generated from the small imbalance between the parallel and anti-parallel states.

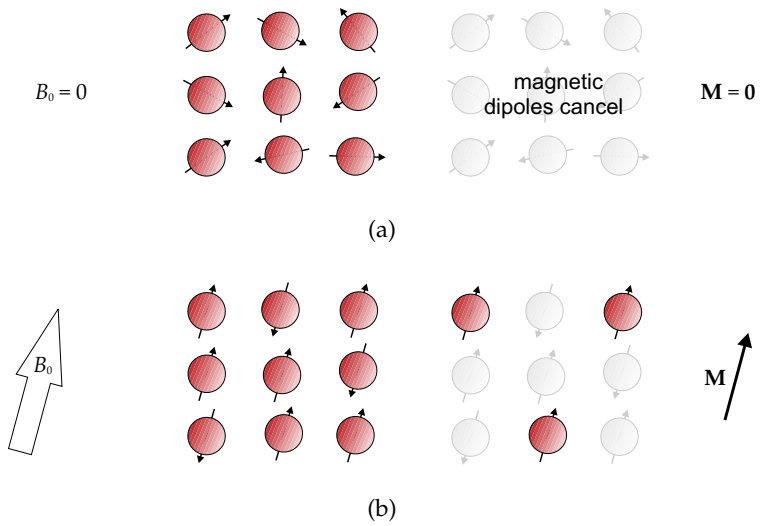

Figure 2.5 A depiction of spin polarisation. Under no external field (a), proton spins are randomly orientated; thus, their individual magnetic dipoles cancel and their net magnetisation is zero. Under an external magnetic field (b), however, they become polarised. The slight tendency of spins to adopt the lower energy orientation then produces a net magnetisation vector, **M**. Here, the proportion of spins adopting the parallel ('spin up') state is greatly exaggerated.

It is now useful to introduce a coordinate system commonly used in MRI. By convention [3], the main magnetic field, referred to as B_0, is usually defined as being in the z-direction (also known as the longitudinal direction). This is also the orientation of the patient table, shown in Fig. 2.6 (a), and the direction along which the patient lies. The x- and y-directions are arbitrary.

The B_0 field is both extremely uniform (normally the field inhomogeneity is only a few parts per million) and extremely strong (normally 1.5 T or 3.0 T). It is measured in units of tesla (T), where 1 T is equal to 10 000 gauss. For comparison, the Earth's magnetic field is strength is around 0.5 gauss. As shown in Fig. 2.5, the B_0 field produces a net magnetisation vector, **M**. The magnitude and direction of **M** can be represented by Fig. 2.6(b).

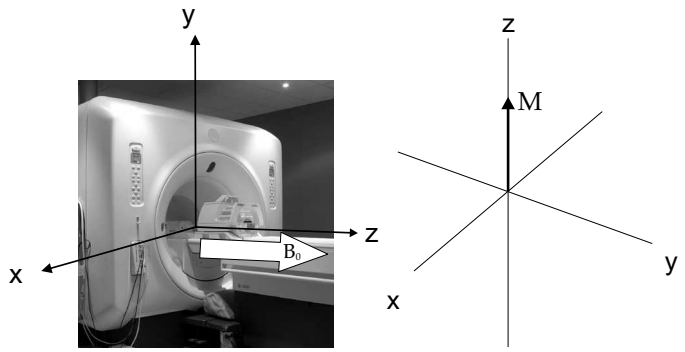

Figure 2.6 The coordinate system used in this thesis: (a) the main magnetic field, B_0, acts in the z-direction through the bore of the magnet; (b) this produces a magnetisation vector, **M**, in the same direction.

2.3 Signal generation

A hydrogen proton can absorb a photon of a particular energy. Quantum mechanically, this is determined by the energy required to enable a transition between the proton's two spin states. Classically, the addition of this energy to a collection of protons can be viewed as causing the net magnetisation vector to be 'pushed' out of alignment with the main magnetic field. It then begins to precess. This behaviour can be described by the *Bloch equation without relaxation*,

$$\frac{d\mathbf{M}}{dt} = \mathbf{M} \times \gamma \mathbf{B} \, , \tag{2.1}$$

where $\times$ represents the vector cross-product and γ is known as the gyromagnetic ratio with units of MHz/T. The cross product operator indicates that the rate of change of **M**

is perpendicular to both **M** and **B**; this implies precession about the direction of the main magnetic field. The rate of precession, ω, can be derived from Eq. (2.1) as follows. In the absence of any field other than B_0, the only non-zero component of **B** lies in the z-direction. Given a net magnetisation purely in the z-direction. Eq. (2.1) can then be expanded to

$$\begin{pmatrix} \frac{\partial M_x}{\partial t} \\ \frac{\partial M_y}{\partial t} \\ \frac{\partial M_z}{\partial t} \end{pmatrix} = \gamma \begin{pmatrix} M_x \\ M_y \\ M_z \end{pmatrix} \times \begin{pmatrix} 0 \\ 0 \\ B_z \end{pmatrix} .$$

Evaluating the cross-product term gives

$$\frac{\partial M_x}{\partial t} = \gamma M_y B_z \tag{2.2}$$

$$\frac{\partial M_y}{\partial t} = -\gamma M_x B_z \tag{2.3}$$

$$\frac{\partial M_z}{\partial t} = 0 .$$

By rearranging Eq. (2.3) in terms of M_x and substituting this into Eq. (2.2), it can be seen that

$$\frac{\partial^2 M_y}{\partial t^2} = -\gamma^2 B_z^2 M_y .$$

This is the equation for simple harmonic motion and the solution gives the angular precession frequency of the magnetisation vector under the influence of the magnetic field B_0,

$$\omega_0 = \gamma B_0 . \tag{2.4}$$

Eq. (2.4) is known as the Larmor equation and is fundamental to MRI. As is shown later, the proportionality of the precession frequency to the strength of the external magnetic field is the key concept in image formation. For hydrogen protons in water, γ has a value of 42.58 MHz/T. The value of γ differs between water and fat by 3.5 ppm – a phenomenon

known as the *chemical shift* [3].

The effect on the magnetisation vector of applying RF energy at this frequency is depicted in Fig. 2.7(a). The net magnetisation is pushed towards the transverse (x-y) plane while it precesses at the Larmor frequency about the z-axis. Often in MRI, however, the situation is instead depicted under the 'rotating frame of reference' in Fig. 2.7(b). Here, the coordinate system itself is taken as spinning around the z-axis at the Larmor frequency; thus, the magnetisation vector is no longer precessing with respect to the axes. This system is used henceforth in this thesis, thereby avoiding the need to show the precession of **M** explicitly. The magnitude of the RF pulse determines the flip angle, α. An RF pulse is normally named after the value of α that it produces: for example, a 90° pulse refers to one that pushes **M** completely into the x-y plane ($\alpha = 90°$).

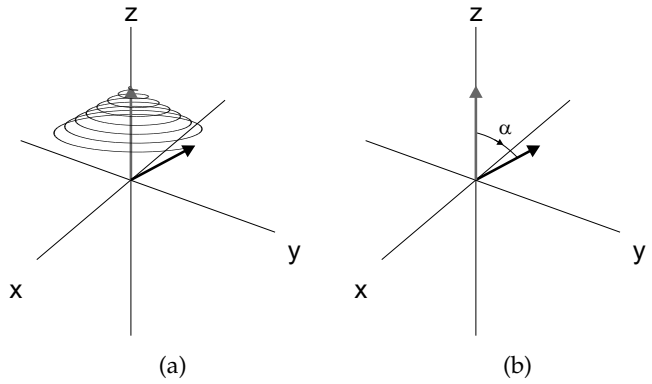

Figure 2.7 The behaviour of the magnetisation vector after the introduction of an RF pulse. In (a), the magnetisation vector precesses about the z-axis before eventually returning to its equilibrium state. The same is shown in (b), except a rotating coordinate system is used. The angle, α, is known as the *flip angle*; its magnitude is determined by the magnitude of the RF pulse.

After completion of the RF pulse, the magnetisation vector will continue precessing at the Larmor frequency. Due to Faraday's law of induction, a signal is generated in an RF receiving coil (arranged perpendicular to the B_0 field) by the transverse component of the magnetisation vector. The frequency of the received signal is that of the precession frequency, ω_0. Individual spins gradually dephase, resulting in a decreasing signal intensity over time. This is known as *free induction decay* (FID).

The spin system eventually returns to an equilibrium state; that is, the magnetisation vector realigns with the B_0 field. The longitudinal or *spin-lattice* relaxation time, T_1, is a measure of how long this takes to occur. Physically, the T_1 decay corresponds to an exchange of energy between the precessing protons and the surrounding lattice. After application of a 90° excitation pulse, M_z is reduced to zero: all magnetisation now lies in the transverse plane. The recovery of M_z to its equilibrium state, where $M_z = M_0$, can then be expressed

as

$$M_z(t) = M_0(1 - e^{-t/T_1})\,. \tag{2.5}$$

Another simultaneous, but independent, effect is the decay of the measured signal, that is, the decay of the component of magnetisation that lies in the transverse plane, M_{xy}.[5] This decay time is quantified by T_2, the transverse or *spin-spin* relaxation time. This decay is more rapid than T_1 decay and is caused by the dephasing of spins leading to a cancellation of their transverse magnetisation. This dephasing arises from spins experiencing slightly different local magnetic fields and therefore precessing at slightly different frequencies, as governed by Eq. (2.4). Again taking a 90° excitation pulse as an example, the T_2-governed decay of M_{xy} from M_0 back to zero is given by

$$M_{xy}(t) = M_0 e^{-t/T_2}\,. \tag{2.6}$$

Eqs (2.5) and (2.6) are illustrated in Fig. 2.8.

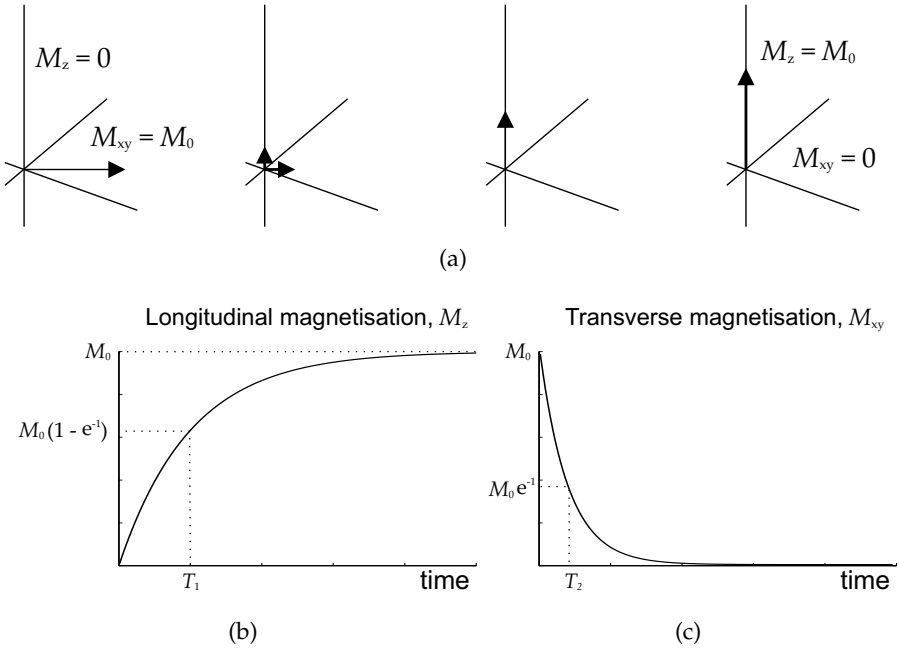

Figure 2.8 Net magnetisation (a) and signal decay resulting from T_1 effects (b) and T_2 effects (c). As shown, T_1 is normally significantly longer than T_2. Although T_1 and T_2 decay occur simultaneously, they are independent of each other.

[5] The spinning top analogy breaks down here due to the independence of T_1 and T_2 decay. The horizontal and vertical components of the main axis of a top are directly related (by Pythagoras' theorem and vector algebra); not so for the magnetisation vector in MRI.

As mentioned in Section 2.1, directly measuring the signal after application of the RF pulse is problematic. The solution is to generate an echo. There are several ways to do this, but the spin-echo pulse sequence is used here as an example (Fig. 2.9). First, a 90° RF pulse is applied at the Larmor frequency, ω_0. After this is switched off, free induction decay occurs as spins dephase. Then, after a certain time period, $T_E/2$, a 180° RF pulse is applied. After a further interval of $T_E/2$, there is an echo. This results from spins that were gradually moving out of phase before the application of the 180° pulse, now moving back into phase with each other. When these spins rephase, they produce a signal once again, centred at the time T_E after the initial 90° pulse. This is known as the *echo time*. For a more detailed description of the spin-echo phenomenon, the reader is referred to any of the reference books mentioned at the beginning of this chapter.

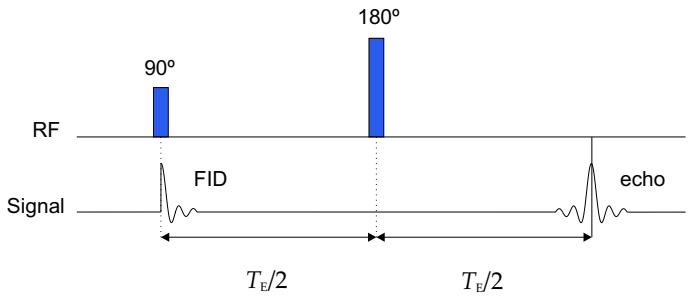

Figure 2.9 The spin-echo phenomenon. An echo is produced if a 90° RF pulse is followed by a 180° RF pulse. Both pulses must be at the Larmor frequency.

Thus, using a combination of the very strong static magnetic field, B_0, and an RF pulse, a signal has been generated from the tissue at time T_E after the first pulse. The echo can be easily detected and measured using a coil of wire: often the same coil used to apply the RF pulses (i.e., a transmit/receive coil).

2.4 Image formation

If all hydrogen nuclei in the body were excited simultaneously as described and the resulting signal recorded, image reconstruction would not be possible. This could be likened to using a digital camera and attempting to form a picture by summing the values of all individual pixels in the image sensor. The result would be meaningless. The key to generating an image is matching the received signal to the location of its source. In MRI, this is known as *spatial encoding*.

Spatial encoding is achieved using three gradient coils fixed inside the scanner, each capable of generating of a magnetic field in the z-direction, that varies linearly in magnitude in one of the x-, y- or z-directions. These field gradients are denoted G_x, G_y and G_z. Mathe-

matically, they are defined as:

$$G_x = \frac{\partial B_z}{\partial x} , \qquad G_y = \frac{\partial B_z}{\partial y} , \qquad G_z = \frac{\partial B_z}{\partial z} .$$

The magnitude of the field in the z-direction, for example, is then given by:

$$B_z(z) = B_0 + G_z z . \tag{2.7}$$

Similar equations apply to $B_z(x)$ and $B_z(y)$.

The first step in the spatial encoding process is *slice selection*. This involves selectively exciting spins in a single two-dimensional (2-D) plane through the three-dimensional (3-D) object. This is achieved using a magnetic field gradient that adds to the main magnetic field as shown in Eq. (2.7). The magnitude of this gradient field, and the centre frequency and bandwidth of the RF pulse, can be adjusted to select the position and thickness of the excited slice (Fig. 2.10). This slice can be at any angle as the three gradient coils can be used together to produce a linear field gradient in any direction. If only G_z is used, however, then the resulting slice is known as *axial* or *transverse* (it is a transverse slice of the brain shown in Fig. 2.4(b)) and G_z becomes the *slice select gradient*. Other perpendicular slices are known as *coronal* or *sagittal*; a slice at any other angle is referred to as *oblique*.

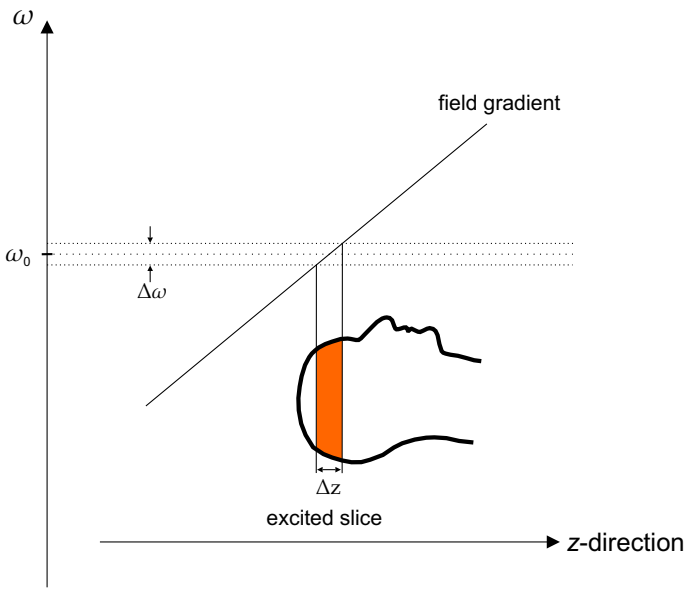

Figure 2.10 Slice selection (axial): the position of the excited slice and its thickness, Δz, can be controlled using a magnetic field gradient (G_z, in this case – see Eq. (2.7)) and the bandwidth and centre frequency of the applied RF pulse. The range of magnetic field strengths that result in excitation is determined by the range of frequencies in the RF pulse (the bandwidth) and Eq. (2.4).

After slice selection, spins have only been excited in a single slab of thickness, Δz, so all received signal has been localised to that slab. The problem of spatial encoding has now in effect been reduced to two dimensions. The next step takes advantage of the fact that any image can be represented as a series of 2-D sinusoids summed together (i.e., a Fourier series).

It is also possible to work backwards, that is, to take a series of spatial frequencies and then add them together to form an image. In spatial encoding in MRI, each sinusoidal component is measured and then all components are combined. To achieve this, spins are deliberately arranged in a succession of 'wave patterns' across the selected slice. If slice selection is in the z-direction, then this is achieved using G_x and G_y, the magnetic field gradients operating in the x- and y-directions, respectively. If a gradient is switched on in a particular direction, then spins across the object in that direction accumulate a phase difference. If both gradients are on, then phase differences accumulate in a diagonal direction. The signal measured at any one point in time is a single value, and is the vector sum of all the spins in the excited slice. It therefore reflects the contribution to the final image of the corresponding sinusoid (Fig. 2.11).

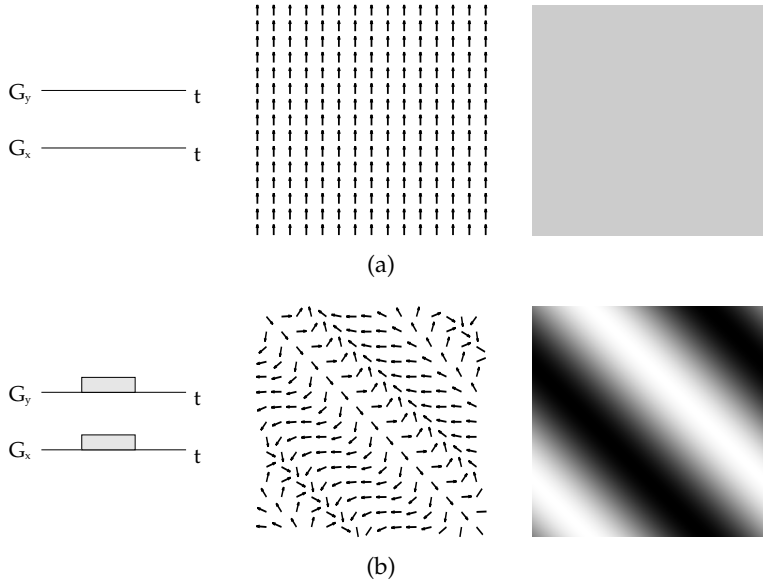

Figure 2.11 Spatial encoding using gradients. With gradients switched off (a), spins all align with the main magnetic field and the received signal is the vector sum of all these. This equates to the average value across the image, or its 'DC component'. When a gradient is applied (b), spins speed up or slow down across the object generating a sinusoidal spin pattern. The received signal then gives the amplitude and phase of this sinusoidal variation across the object and, therefore, the image.

Each spatial frequency component through the object is measured individually and represented by a data point in *k*-space: a complex-valued array normally of the same dimen-

sions as the final image.[6] The *k*-space data is complex because each sinusoidal component requires both a magnitude and a phase to describe it.

As each wave function must be measured individually, spins must be excited a number of times (typically hundreds). Unfortunately, it is necessary to wait for spins to relax between excitations in order to produce enough signal for the next excitation. The resulting time between excitation pulses is known as the repetition time, T_R (Fig. 2.12). Also shown in Fig. 2.12 are the gradient fields, the RF excitation pulse and the signal generated in the imaged object. Normally, the x-direction is referred to as the *frequency-encode* or *readout* direction while the y-direction is referred to as the *phase-encode* direction. This terminology can be confusing, however, so is avoided at present.

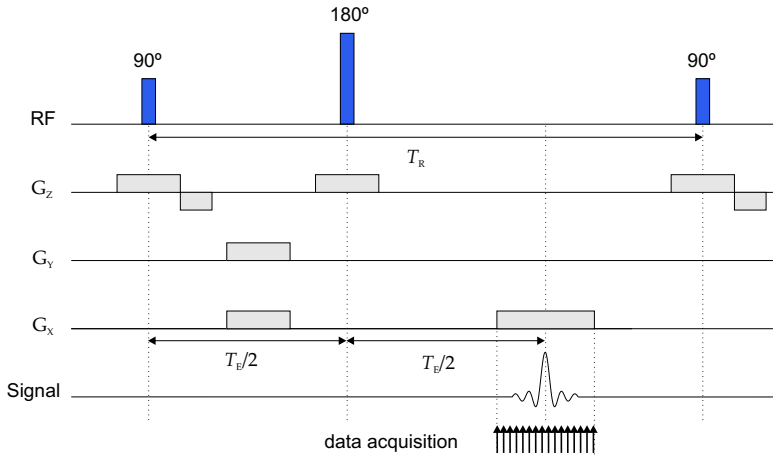

Figure 2.12 A simplified pulse sequence diagram showing the RF pulses, gradient fields and received signal for the spin echo pulse sequence. The echo time, T_E, and the repetition time, T_R, are also shown.

The acquisition order of the points in *k*-space is referred to as a *k-space trajectory*. Fig. 2.13(a) and (b) show a possible pulse sequence and the resulting *k*-space trajectory. In this case, G_z is the slice select gradient, explaining its presence during application of both RF pulses. Spins in the excited 2-D plane are then manipulated using the G_x and G_y gradients. The application of G_x and G_y change the angle and frequency of the sinusoidal arrangement of spins across the object (refer back to Fig. 2.11). This can be thought of as moving the point of data acquisition in *k*-space, as each *k*-space point represents a specific spatial frequency.

The problem with the system depicted in Fig. 2.13 (a) and (b) is that only a single point in *k*-space has been acquired after the RF excitation shown. Clearly the acquisition of all points will take a considerable time. A common solution to this problem is to apply a gradient during data acquisition (Fig. 2.13(c)). This results in a constantly changing spin pattern

[6]The origins of the term '*k*-space' appear to be in the field of solid-state physics. The earliest mention of *k*-space in MRI literature known to the author is in a 1982 paper: 'NMR chemical shift imaging in three dimensions' [17].

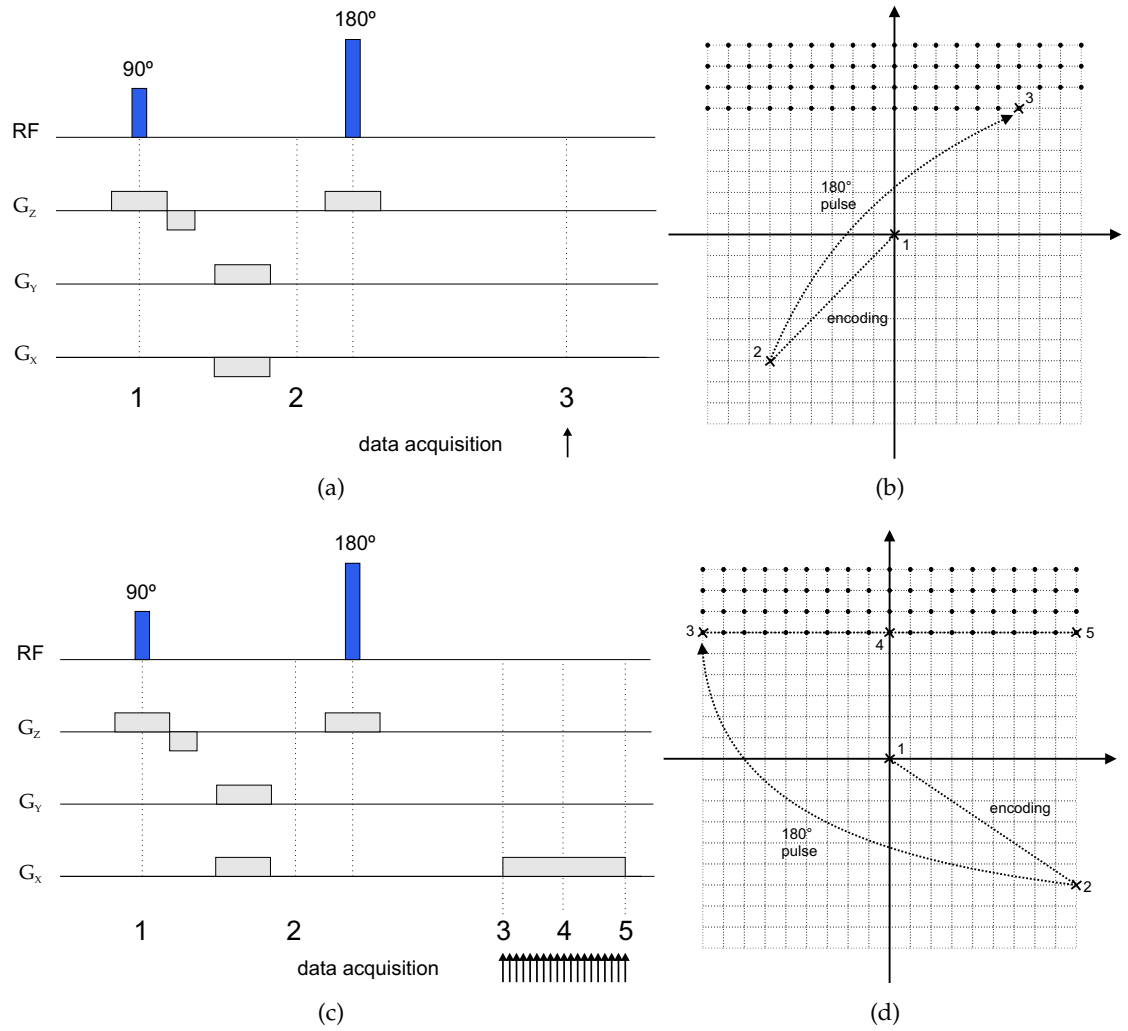

Figure 2.13 Examples of possible pulse sequences (a) and (c) and their resulting *k*-space trajectories. In (a), a single point in *k*-space is acquired; clearly it will take a long time to fill *k*-space using such a system. The sequence shown in (c), however, acquires an entire line of *k*-space for each RF excitation.

and thus movement of the data acquisition point in *k*-space (Fig. 2.13 (d)) enabling a whole line of data to be acquired for each RF excitation.

Most trajectories involve collecting data directly onto the Cartesian grid; however, this is not always the case. It is possible to collect points onto some other sampling system and then interpolate them back so that the inverse Fourier transform (implemented using the FFT) can be applied to reconstruct the image. A good example of this is spiral imaging (this is discussed in Section 3.3.2). The number of possible trajectories is limitless. Research has even been carried out applying a missile guidance trajectory [18] design approach to a 3-D *k*-space trajectory.

2.4.1 The Bloch equation and the Fourier transform

The above description of image formation in MRI is relatively qualitative. A more mathematical description follows.

The behaviour of the nuclear magnetisation vector, $\mathbf{M}(t)$, is governed by the Bloch equation. This was given earlier in Eq. (2.1), neglecting the effects of T_1 and T_2 relaxation. Including these effects, the Bloch equation is

$$\frac{d\mathbf{M}}{dt} = \mathbf{M} \times \gamma\mathbf{B} - \frac{M_x\mathbf{i} + M_y\mathbf{j}}{T_2} - \frac{(M_z - M_0)\mathbf{k}}{T_1} \ , \tag{2.8}$$

where $\times$ represents the vector cross-product; **i**, **j** and **k** are the unit vectors in the x-, y- and z-directions, respectively; **B** represents the vector sum of the main magnetic field (B_0), the applied RF field and the gradients (G_x, G_y and G_z); γ is the gyromagnetic ratio (see Eq. (2.4)); and M_0 is the magnitude of the equilibrium magnetisation arising from the B_0 field.

The Bloch equation can be solved (refer to [3]) to relate the transverse nuclear magnetisation distribution, $m(x, y)$, to the measured signal at a particular time, $s(t)$, namely,

$$s(t) = \int_x \int_y m(x, y) e^{-i2\pi[k_x(t)x + k_y(t)y]} dx dy \ , \tag{2.9}$$

where $k_x(t)$ and $k_y(t)$ are given by

$$k_x(t) = \frac{\gamma}{2\pi} \int_0^t G_x(\tau) d\tau \ ,$$
$$k_y(t) = \frac{\gamma}{2\pi} \int_0^t G_y(\tau) d\tau \ .$$

Eq. (2.9) is immediately recognisable as a Fourier transform. Samples of $s(t)$ therefore correspond to samples in *k*-space, that is, samples of $F(k_x, k_y)$. Given the *k*-space data, we can use the inverse Fourier transform to reconstruct an image, i.e.,

$$f(x,y) = \int_{-\infty}^{\infty}\int_{-\infty}^{\infty} F(k_x,k_y)e^{i2\pi(k_x x+k_y y)}dk_x dk_y \ , \tag{2.10}$$

where $F(k_x, k_y)$ is the acquired *k*-space data and $f(x, y)$ is the reconstructed image. In practice, however, the *k*-space data is discrete as it is sampled and stored in an array, and so the inverse discrete Fourier transform (DFT),

$$f(x,y) = \sum_{k_x=0}^{N_{kx}-1}\sum_{k_y=0}^{N_{ky}-1} F(k_x,k_y)e^{i2\pi(k_x x+k_y y)} \ , \tag{2.11}$$

is used, for which x, y, k_x and k_y all take integer values and N_{kx} and N_{ky} are the *k*-space matrix sizes in the x- and y-directions respectively. Eq. (2.11) is referred to from now on as the *inverse 2DFT* while the forward transform will be referred to as the *2DFT*. A rapid implementation of these transforms exists; this is the *Fast Fourier Transform (FFT)*. To enable the use of the FFT, all samples must be on a regular Cartesian grid. The dimensions of *k*-space (and therefore the dimensions of the final image) are typically a power of two, although this is not always the case.

2.5 Image contrast

An X-ray image is a 'map' of the imaged tissue's X-ray attenuation. An MR image, however, is a map that indicates one of many possible tissue properties or a combination of several. When imaging is configured to show one particular property over the others, the reconstructed image is *weighted* by that property. Three weightings are intrinsic: T_1, T_2 and proton density (PD).

The time constant T_1 defines the time taken for the longitudinal magnetisation to return to its equilibrium value after application of an RF pulse (refer back to Eq. (2.5)). To obtain an image weighted by this property, both the repetition time, T_R, and the echo time, T_E, are kept relatively short. Keeping T_E short ensures that T_2 decay has little influence on the signal strength. Keeping T_R short, however, has the opposite effect for T_1 as the longitudinal relaxation does not have time to fully recover between excitations. The extent to which it does recover – and the resulting signal strength – is governed by the T_1 of the tissue; thus, an image weighted by T_1 is formed. Water has a long T_1 so magnetisation does not fully recover if a short T_R is used; therefore, water appears dark. Fat has a shorter T_1 so the longitudinal magnetisation has time to recover; therefore, fat appears bright on the final

image.

To obtain a T_2-weighted image, both the repetition time, T_R, and the echo time, T_E, are long. A long T_R means that all longitudinal magnetisation recovers between excitations. Thus, T_1 does not influence the final image contrast. A long T_E means that significant signal dephasing and decay occurs. The exact amount depends on the T_2 of the tissue; therefore, the resulting image is T_2 weighted. As water has a long T_2 it appears bright on a T_2 weighted image while fat, with a shorter T_2, appears dark.

Proton density refers to the number of hydrogen protons per unit volume of tissue. To generate a PD-weighted image, the T_R must be long and the T_E must be short. This results in minimal T_1 weighting (longitudinal magnetisation recovers fully between excitations) and minimal T_2 weighting (there is little time for T_2 signal decay using a short T_E). Without T_1 or T_2 weighting, the image is weighted by the density of protons as these are the source of the NMR signal. The relationship of T_E and T_R to the image weighting is summarised in Table 2.1. As seen in Table 2.2, however, the difference in PD between tissues is not as significant as it is for T_1 or T_2, so a PD-weighted image has relatively poor contrast.

Image weighting	T_R	T_E
T_1	short	short
T_2	long	long
PD	long	short

Table 2.1 The relationship of image weighting to the repetition time, T_R, and the echo time, T_E.

The choice of weighting depends on the anatomy being scanned and the diagnostic information required. Fluids are very dark in T_1 images, while fat-based tissues are very bright. The boundaries between different tissue types are very clear so this type of scan is sometimes known as an 'anatomy scan' [1]. In T_2 images, fluids are bright and fat-based tissues are grey. In abnormal tissue there is often an increase in water content. As this abnormal fluid shows up bright against a dark background, a T_2-weighted image is excellent for identifying pathology and is sometimes termed a 'pathology scan'.

An example showing the same sagittal slice but with different image weightings is given in Fig. 2.14. The T_R and T_E values used to produce the images shown are given; the choice of these values is influenced by a number of factors, however, including the main magnetic field strength of the scanner.

A number of other image contrast mechanisms are available; this flexibility is one reason why MRI is such a powerful imaging modality. For example, images can be weighted to

Tissue type	T_1 (ms)	T_2 (ms)	Proton density (relative to CSF)
White matter	600	80	0.65
Grey matter	950	100	0.8
CSF	4500	2200	1.0
Fat	250	60	0.9

Table 2.2 Approximate PD, T_1 and T_2 values for different tissue types at 1.5 T [16]. Bone produces little signal in MRI.

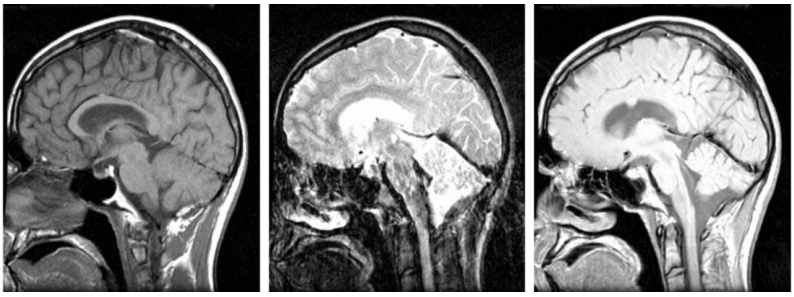

(a) (b) (c)

Figure 2.14 The same sagittal slice imaged using different weightings: (a) T_1 ($T_R = 400$ ms, $T_E = 14$ ms), (b) T_2 ($T_R = 1500$ ms, $T_E = 100$ ms) and (c) PD ($T_R = 1500$ ms, $T_E = 14$ ms). Images are from MDPH406 course notes, 2005, University of Canterbury.

show the diffusion of water molecules; this can reveal information about tissue structure on a microscopic scale. When applied to the brain and with the inclusion of direction information, this can show the orientation of white matter fibre tracts.[7]

2.6 Properties of *k*-space

This section introduces the properties of *k*-space that are referred to later in this thesis. This is by no means a complete treatment, however. For further information, an excellent description of concepts relating to *k*-space in MRI is given in [20].

2.6.1 Signal energy distribution

High spatial frequency information is found around the edge of *k*-space while lower spatial frequency information is located near the centre. Fig. 2.15 illustrates this point using a photo (Ama Dablam, Nepal) taken by the author. If an image is reconstructed without the periphery of *k*-space, then it is lacking in detail; if an image is reconstructed without the centre of *k*-space, then it is lacking in contrast. It should also be clear from Fig. 2.15 that

[7] This is a fascinating topic but well outside the scope of this thesis. The reader is referred to Watts et al. [19] for an excellent overview and some amazing images generated using this technique.

most of the signal energy is found at the centre of *k*-space. In fact, the *k*-space magnitude shown is displayed on a logarithmic scale – without this scaling, all that would be visible is a bright point in the centre.

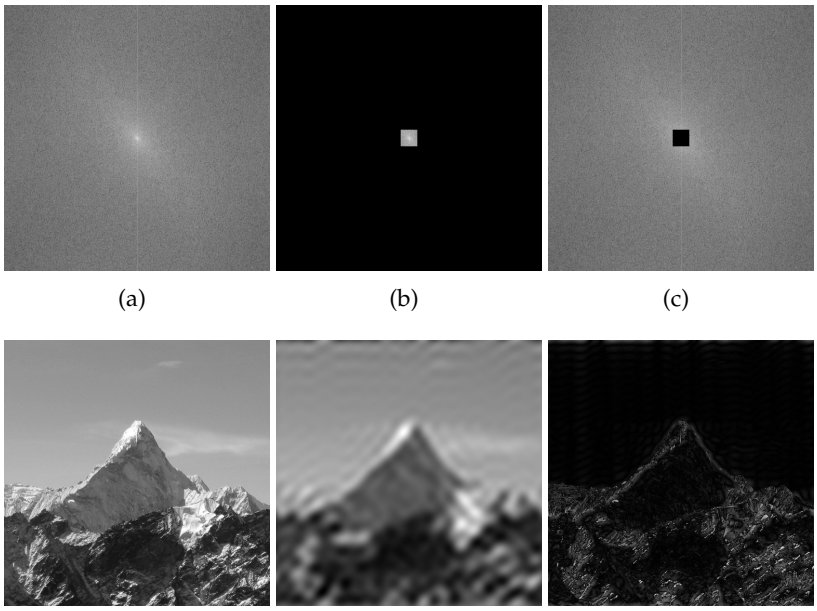

Figure 2.15 The distribution of spatial frequencies in *k*-space: (a) is the *k*-space equivalent (log of magnitude values) of the image in (d). If only the central portion of *k*-space is taken (b) and an image reconstructed (e), the result retains most of its contrast but is very blurred. If, however, the periphery of *k*-space is used in the reconstruction and the centre omitted (c), the resulting image (f) contains all its original sharp edges but little contrast.

2.6.2 Noise in *k*-space

Although the distribution of signal energy in *k*-space is weighted extremely heavily towards the centre, this is not the case for noise. Noise in MRI is considered to be white and Gaussian distributed, that is, of zero mean and with equal power at all frequencies within the readout bandwidth. Noise is present due to random fluctuations in electrical current in the receive coil electronics and the object being imaged [16, 1].

In the MRI community, several different ways of measuring the signal-to-noise ratio (SNR) are common. One definition is the ratio of peak signal amplitude to noise standard deviation (the noise standard deviation is equivalent to its root mean squared value since white noise has zero mean). This definition is convenient when determining the SNR of a magnitude image (when *k*-space has already been inverse Fourier transformed and the magnitude taken). Noise can be readily quantified by using regions of the image outside the support region of the object. In this case a conversion factor (≈ 0.655) must be used to obtain the standard deviation of the underlying Gaussian-distributed white noise from the

Raleigh-distributed noise in the magnitude image. A derivation of this value is provided in [16].

This work, however, deals largely with *k*-space data and largely (as far as experiments involving SNR are concerned) with simulations. Thus, it is possible to evaluate the signal energy, S_E, and the noise energy, N_E, separately. Therefore, the definition of SNR used here is the ratio of signal energy to noise energy, that is,

$$\text{SNR (dB)} = 10 \log \frac{S_E}{N_E} \ , \tag{2.12}$$

where the conventional definition of 'energy' is used, that is,

$$S_E = \sum_{p=0}^{N_{kx}-1} \sum_{q=0}^{N_{ky}-1} |s(p,q)|^2 \ ,$$
$$N_E = \sum_{p=0}^{N_{kx}-1} \sum_{q=0}^{N_{ky}-1} |n(p,q)|^2 \ ,$$

where $s(p,q)$ is the uncorrupted signal, and $n(p,q)$ the Gaussian-distributed noise, at point (p,q) in *k*-space.

Parseval's theorem for the Fourier transform states that the energy computed in one domain is equal to the energy computed in the other. Here, the signal energy computed in the Fourier domain (*k*-space) is therefore equal to the signal energy computed in the image. The same applies to the noise energy. Thus, the SNR can be computed in either domain as shown in Eq. (2.12) and will yield the same result.

There are occasions in this thesis when simulated data, with SNR calculated as shown in Eq. (2.12), are compared to data acquired using an MRI scanner. The SNR for the scanner data can also be estimated by dividing the signal energy by the noise energy. The noise energy is approximated by taking an region of area A, outside the support region of the object in the image, computing the energy within this region, and scaling this by the ratio of the full image size to A. The signal energy is simply taken as the total energy in the image: a reasonable approximation because the signal energy is usually much greater than the noise energy.

The SNR is influenced by a number of imaging parameters, most of which can be controlled

by the scanner operator. In some situations, it is common to measure the *k*-space data more than once and compute the average value to improve the SNR. The number of signal averages is denoted N_{SA}, and is of particular relevance to this thesis. It is related to the SNR by

$$\text{SNR} \propto \sqrt{N_{SA}} \, . \tag{2.13}$$

Thus, if two images are taken and averaged ($N_{SA} = 2$), then the SNR will improve by a factor of $\sqrt{2}$.

2.6.3 Hermitian symmetry

Another important property of *k*-space data is that it exhibits Hermitian symmetry, that is, it is equal to its own conjugate transpose: for a matrix F containing data in *k*-space, $F = F^H$, where the ^{H} superscript indicates the conjugate transpose operation. This is true if and only if the image is real.

Hermitian symmetry is used in *half-Fourier imaging*, where an image is reconstructed after collection of only half the *k*-space data. The main penalty is a slight drop in SNR by around 30 %. More exactly, SNR is modified by the factor $1/\sqrt{2}$ (substitute $N_{SA} = 1/2$ into Eq. (2.13) to see this). In practice, however, imperfections exist which violate the Hermitian symmetry of the *k*-space data to some extent. Thus, slightly more than half of *k*-space is typically acquired to provide enough information to estimate, and correct for, these effects.

2.6.4 Translation and rotation properties

Translation of the imaged object affects the phase of the *k*-space data. If the object is translated a distance (x_0, y_0) from a reference position during data acquisition, a phase offset is generated in the data which is linearly dependent on the *k*-space location, that is,

$$\begin{aligned} f(x, y) &\longleftrightarrow F(k_x, k_y) \\ f(x - x_0, y - y_0) &\longleftrightarrow F(k_x, k_y) e^{-i2\pi(k_x x_0 + k_y y_0)}. \end{aligned} \tag{2.14}$$

where $\longleftrightarrow$ represents the two-dimensional Fourier transform. Eq. (2.14) is known as the Fourier shift theorem.

It is also useful to examine the effect in *k*-space of rotating the object within the field-of-

view. Take, for example, a point (x, y) within an image. If this point is rotated by an angle θ about the centre of the image, its new coordinates, (x', y'), are given by

$$\begin{bmatrix} x' \\ y' \end{bmatrix} = \begin{bmatrix} \cos\theta & \sin\theta \\ -\sin\theta & \cos\theta \end{bmatrix} \begin{bmatrix} x \\ y \end{bmatrix} .$$

A property of the two-dimensional Fourier transform is, however,

$$f(x\cos\theta - y\sin\theta, x\sin\theta + y\cos\theta) \longleftrightarrow F(k_x\cos\theta - k_y\sin\theta, k_x\sin\theta + k_y\cos\theta) . \quad (2.15)$$

Eq. (2.15) indicates that if an object is rotated, the *k*-space data representing that object is also rotated by the same angle. This is a well-known property of the Fourier transform [21,22] and is sometimes referred to as the Fourier rotation theorem. Fig. 2.16 demonstrates this property using an image.

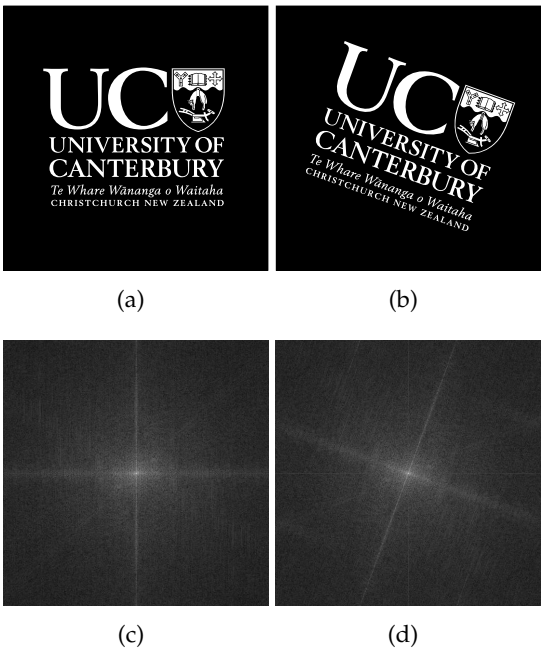

Figure 2.16 A demonstration of the effect of rotating an object on its Fourier transform. If the object is rotated by angle θ, then its Fourier transform also rotates by angle θ.

Chapter 3

Motion in MRI

This chapter draws on the general concepts presented in the previous chapter and focuses on the problem of imaging a moving object. The first section, *The effects of patient motion*, explains how motion of the object causes artifacts in the image. The remaining three sections, *Motion prevention*, *Motion effects avoidance* and *Motion correction*, describe three general approaches to solving this problem. These sections review background literature and describe specific techniques. Finally, conclusions are drawn that provide direction for the research.

3.1 The effects of patient motion

The data acquisition time in MRI varies depending on the particular sequence used. It is, however, often of the order of minutes, meaning that there is a high chance the patient will move during the acquisition. A number of types of motion can adversely affect the final image:

- Large-scale/bulk motion: motion of the entire object being imaged, such as the head or torso of a patient.
- Respiration: motion caused by the breathing of the patient.
- Cardiac motion: motion of the heart muscle and major blood vessels.
- Blood flow: blood moving through an otherwise stationary slice.
- Gastrointestinal peristalsis: motion of the intestine and its contents due to peristalsis.

Of these five, the last four have somewhat satisfactory solutions. Motion from respiration can sometimes be prevented by breath-holding [4]; however, for longer scans techniques such as respiratory gating [23] or respiratory ordered phase encoding (ROPE) are used [24]. Similarly, the problem of cardiac motion is commonly mitigated by cardiac gating [25]. Blood flow effects can be reduced using techniques such as gradient moment nulling [4]. Peristalsis can be temporarily 'frozen' for a short time during imaging using antiperistaltic drugs such as hyoscine butylbromide [1].

Most of the above techniques have been available for many years: a summary is available in a 1986 review article by Bellon et al. [26]. Bulk motion is, however, still a major problem in MRI. This thesis focuses on bulk motion that occurs *during* a single acquisition sequence, not motion occurring *between* sequences; the latter can be corrected for using image registration techniques.

The author performed a simple experiment to quantify the head motion of healthy subjects trying to remain motionless. Results of this experiment are given in Appendix B.

3.1.1 Motion artifacts

For simplicity of analysis, attention is restricted to motion consisting of rigid-body translation and rotation within the slice being imaged and therefore involving the x- and y-dimensions only. As shown in Eq. (2.14), if a body is translated a distance (x_0, y_0) from a reference position during data acquisition, a phase error is generated in the data. Similarly, as shown in Eq. (2.15), if the body is rotated from a reference position, acquired lines in *k*-space are correspondingly rotated from their nominal orientation.

Data acquisition is extremely rapid in the frequency-encode (FE) direction so motion is effectively 'frozen' for this time. Thus, inconsistencies which exist in *k*-space due to motion only occur between lines in the phase-encode (PE) direction.

Inconsistencies in the PE direction result in ghosting or blurring in the same direction in the image (Fig. 3.1). Here, ghosting is defined as repeated versions of the image or part of the image while blurring is similar to motion blur in a photograph. Blurring is caused by a wide central peak in the point spread function (PSF). Ghosting is generated by more widely spread oscillations in the PSF. The reconstructed image, $f(x, y)$, is related to the PSF, $h(y)$, and the ideal image, $g(x, y)$, by

$$f(x, y) = g(x, y) \otimes h(y), \tag{3.1}$$

where $\otimes$ represents the convolution operation.

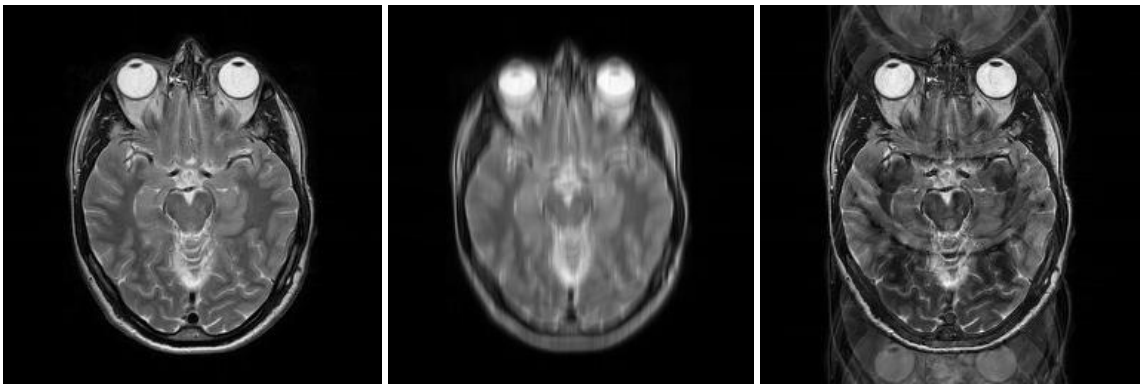

(a) (b) (c)

Figure 3.1 A demonstration of blurring and ghosting using simulated motion: (a) a normal image; (b) a blurred image; and (c) an image showing ghosting. The effects in (b) and (c) occur mainly in the phase-encode direction (vertical in these examples).

Although not the focus of this thesis, it is worth mentioning that multiple-shot diffusion MRI (clinically important for the assessment of stroke patients) is especially sensitive to motion [27]. Head motion is also a particular problem in fMRI as it can corrupt the signal induced by brain activation [28].

3.1.2 Case study: research into babies born under the methadone programme in NZ

The Christchurch Methadone Programme involves substituting methadone in place of other opioid drugs. Pregnant women are regularly admitted to this programme. Research is now being carried out, however, to determine the effect of methadone during pregnancy on the child. One study in Christchurch, New Zealand, aims to answer the question: "Does dose matter?", or more specifically, whether a 15 mg or 180 mg dose of methadone affects the outcome for the child.

MRI is used to determine the volume of different areas of the brain in the newborn child, as well as performing fibre tracking and checking for anatomical changes. The study involves three groups of babies, imaged between two weeks and two months after birth:

- Babies born pre-term. These move very little and can normally be held in place with a cushion.
- Normal babies. This forms the control group. Motion is problematic unless the baby is asleep.
- Methadone babies. According to the research nurse involved, these babies cause severe motion problems and therefore require the most scanner time.

Imaging is carried out on a 1.5 T scanner (GE Medical Systems) at Southern Cross Radiology in Christchurch. Images acquired include: T_1 sagittal, coronal dual echo, coronal FSPGR, axial T_2, and diffusion tensor imaging. The data acquisition time for each of these sequences is between 3 and 9 minutes; this is the time that the baby must remain motionless.

Currently, the only motion prevention method used is a vacuum cushion that holds the baby in place. Imaging methadone babies takes typically twice as long as imaging a normal baby due to scans having to be repeated. The images shown in Fig. 3.2 are from one such baby.

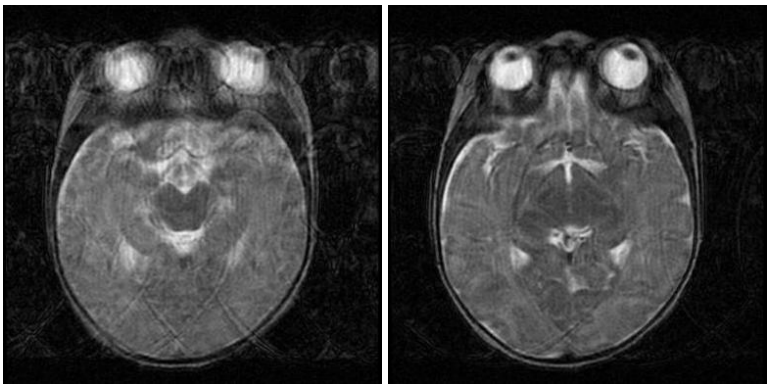

(a) (b)

Figure 3.2 The effects of motion. An axial head image of a child (two months old) showing (a) severe motion artifacts and (b) mild motion artifacts (Lianne Woodward, Child Development Research Group, University of Canterbury).

A further motion-related issue has recently arisen in the study. It would be beneficial to image using a 3 T scanner (recently installed in Christchurch) due to better SNR and resolution. This is problematic, however, as the acoustic noise generated by a 3 T scanner is up to 20 dB greater than that produced by a 1.5 T system. The noise level can easily reach 130 dB SPL [29,30] so high-quality hearing protection is essential. Even with this, however, the extra noise is expected to cause greater motion problems, largely due to the reduced chance of babies sleeping through the procedure.

3.2 Motion prevention

The most obvious – and the most commonly used – approach to avoiding motion artifacts in MRI is preventing motion of the subject. Most examinations use at least one of the techniques described here.

3.2.1 Physical restraints

In MRI, the patient is almost always immobilised using a physical restraint: often cushions, bean bags or foam packed around the head within the head coil. These methods are easy to use and cause little distress to the patient; however, the level of immobilisation achieved is low.

Several other types of physical restraint exist. Bite bars are sometime used; these involve making a dental mold and then having the subject hold it firmly in their mouth [31, 32]. As the mold is custom-made, it fits the user well and can greatly reduce motion. The inconvenience of constructing a personalised restraint is a major disadvantage, however. In addition, the presence of an object in the mouth of a patient can increase swallowing, leading to an increase in head motion [33].

Edward et al. [33] report success using a plaster cast head holder. Again, this is custom-made and uses the head of the subject as a mold; hence, it exerts an even pressure on the skull and fits comfortably. Considerably lower levels of translational and rotational head motion are achieved compared to restraining straps and subject tolerance of this device is reportedly good. Unlike some systems, the subject can remove themselves from the scanner at any time - knowledge that this is possible undoubtedly reduces patient anxiety. The main disadvantage is the time (and resulting expense) involved in preparing each cast, which then needs to set overnight. Although possibly useful for research, this system would not be accepted clinically for this reason.

In general, physical restraints often cause problems by adding to patient discomfort and feelings of claustrophobia. Claustrophobia is a major problem in MRI and patients sometimes need to have 'breaks' during their scan if they suffer from this. Any restraint must also be easy to use: if a system can only be used on a well-behaved and fully conscious patient, then it is of limited use clinically. Physical restraints are also often inappropriate for use in fMRI as they may interfere with the study itself.

3.2.2 Sedation

Sedation of the patient may be considered in some cases to avoid motion. There are, however, several disadvantages associated with sedation. Monitoring sedated patients adds an unwanted complication to the scan and often requires the presence of an anaesthetist. Although in widespread clinical use, it is unacceptable for use on normal volunteers (for research) due to safety concerns. For example, sedation of children for MRI and CT is associated with risks of hypoxemia [34, 35]. One of these studies, by Malviya et al. [34], also showed that excessive motion was still present in 12 % of sedated children. Furthermore, sedation cannot be used for functional MRI (fMRI) due to the potential for interfer-

ing with experimental results. According to local radiographers, less than 3 % of patients in Christchurch are sedated for their scan: this course of action is used only when all other alternatives fail.

3.2.3 Training

It is possible to train subjects to hold themselves still prior to their scan. While this is time-consuming, scanner time can be saved due to a reduction in repeated scans.

Slifer et al. [36] trained subjects to lie still in a simulator constructed from an inactive scanner. The situation was made as realistic as possible: taped scanner noise was played at high volume and a standard head support and restraining straps were used. Subjects (all children) watched a video which was halted whenever their head motion exceeded a certain threshold. Over time, this threshold was gradually reduced. This proved to be an effective technique. While this approach has potential for studies of healthy subjects, it could not be generalised to acutely ill patients.

3.3 Motion effects avoidance

Some methods of imaging in MRI are less prone to motion artifacts than others. Of course the use of these comes at a cost: normally overall image quality or resolution. Nevertheless, if patient motion is anticipated, the scanner operator may decide that this trade-off is worthwhile.

3.3.1 Fast imaging

If data acquisition in MRI were as rapid as taking a simple chest X-ray (for example), patient motion would not be problematic. MRI is extremely slow, however. Nevertheless, there are many ways that acquisition time can be reduced; a good comparison of these methods is presented by Li and Mirowitz [37]. Such a comparison is useful because there is normally a trade-off between acquisition time and image quality. Thus, it is often the case that although an image may be free of motion artifacts, it is badly degraded due to other effects.

Fast spin echo (FSE), first introduced by Hennig et al. in 1986 [38], is one rapid imaging technique that produces images with relatively little distortion.[1] While conventional spin echo sequences produce only a single echo per 90° excitation pulse, FSE uses multiple 180° refocusing pulses to produce multiple echoes for each excitation pulse (Fig. 3.3). This

[1] FSE is also known as RARE (rapid acquisition with relaxation enhancement) or TSE (turbo spin echo).

substantially reduces imaging time by acquiring multiple lines of *k*-space in a single T_R period.

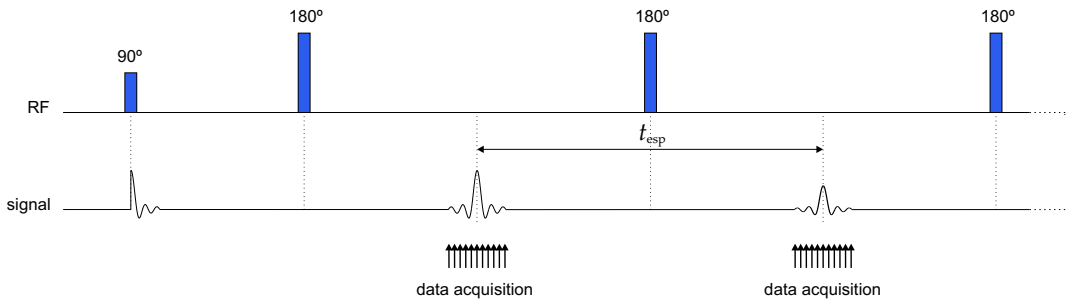

Figure 3.3 Applied RF pulses and received signal for the fast spin echo (FSE) sequence. Multiple 180° pulses produce multiple echoes; combined with the appropriate gradient fields, this corresponds to acquiring multiple lines of *k*-space rapidly. The signal strength drops with each echo, however, due to T_2 effects.

The number of echoes in FSE is known as the *echo train length* (N_{etl}). Each 90° pulse followed by N_{etl} 180° pulses is often referred to as a *shot*. Signal decay due to T_2 effects limits the number of *k*-space lines that can be acquired in a single shot: in practice, this number rarely exceeds 32. Nevertheless, if 32 lines of *k*-space are acquired in each T_R period this reduces imaging time over a standard spin echo sequence by a factor of 32 – a significant reduction.

Motion artifacts still affect images acquired using FSE. Imaging time for multiple-shot FSE is reduced over conventional spin echo sequences but is still of the order of tens of seconds. Single shot FSE, that is, the acquisition of all *k*-space data in a single RF excitation can provide a solution. Due to T_2 signal decay problems mentioned above, however, image resolution is severely limited.

Another rapid imaging technique is echo planar imaging, or EPI. EPI was one of the first pulse sequences to be developed [39] but is still one of the fastest: an entire image can be acquired in less than 100 ms. It achieves such a short acquisition time by using a series of gradient-echo trains, that is, it uses gradient-refocusing rather than RF-refocusing as is used for FSE. EPI, however, is extremely prone to image artifacts. It is discussed in more detail in Section 8.1.2.

Although not described here, other rapid imaging techniques exist. These present a similar trade-off to that provided by FSE and EPI: imaging time (and motion effects) can be reduced dramatically, but resolution and general image quality suffer.

3.3.2 Radial imaging

Rather than acquiring data in *k*-space directly onto a Cartesian grid (refer back to Fig. 2.13), it is possible to use a radial *k*-space acquisition. Such acquisitions are inherently more robust to motion artifacts than Cartesian methods [40]. The reasons for this are in part explained in Chapter 9 of this thesis. A number of radial schemes have been proposed: notable recent examples are WHIRL [41] (an extension to TWIRL [42]), ROSE [43] and STAR [40].

In spiral imaging (Fig. 3.4), data acquisition begins at the *k*-space centre and gradually moves outwards. Good results have been obtained using spiral techniques for fMRI [44]. Spirals can also be interleaved [45], meaning that it is not necessary to acquire all *k*-space data in a single shot. Radial imaging can also be extended to three dimensions. For example, Shu et al. [46] have demonstrated the effectiveness of their 'Undersampled Spherical Shells' trajectory.

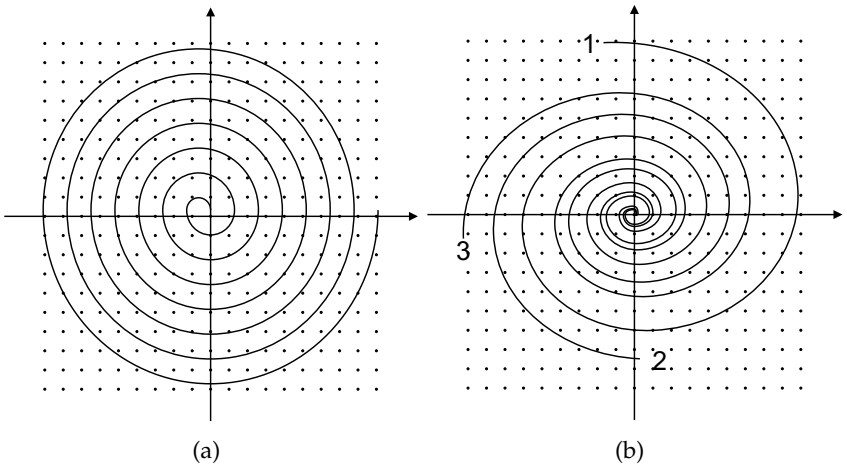

Figure 3.4 Two possible spiral acquisitions: (a) single-shot and (b) an interleaved scheme with three shots, numbered from 1 to 3. Data is acquired at points lying on the spiral. A gridding algorithm is then normally used to calculate values on the Cartesian grid so that the inverse DFT can be applied.

Some major problems affect radially acquired acquisitions. One is off-resonance blurring [4], although methods to reduce this do exist [47]. Also, radial methods commonly oversample the centre of *k*-space; this can be a disadvantage as it is an inefficient use of sampling time (the central *k*-space data already has a high SNR compared to data at the *k*-space periphery). Furthermore, if a non-Cartesian trajectory is used, data must then be gridded in order to reconstruct an image using the FFT.

In terms of motion effects, radial imaging does have something to offer. The central *k*-space data is often all acquired in the same time period so discontinuities here due to

motion are less likely. Thus, obvious ghosting across the image is rare with spiral imaging. Contributing to this effect is the fact that discontinuities are unlikely to cause a periodic modulation across *k*-space. This topic is investigated in more detail in Chapter 9.

3.4 Motion correction

The third approach to avoiding motion artifacts is to allow motion to occur, quantify it, and then discard or correct corrupted data. A number of correction techniques have been attempted and a few are now regularly used in a clinical environment. Such methods often involve a combination of sequence design and post-processing.

3.4.1 Navigator echoes

The first mention of navigator echoes in the literature was in 1989 by Ehman and Felmlee [48, 49]. Since then, navigator echoes have been used extensively in the research community, but are not widely available on clinical scanners to correct for head motion. They are used routinely, however, for cardiac motion.

In the simplest implementation of the technique, a line of data in *k*-space is repeatedly sampled during acquisition of the remainder of the *k*-space data. Post-processing of the navigator data reveals information about the motion of the object. Data collected during periods of motion can then be discarded, based on the assumption that it has been corrupted. This system is not very efficient: in cases of severe motion, most acquired data may need to be discarded.

If navigator echoes are used to correct motion-corrupted data, rather than just discarding it, a further step is required. This often involves the rotation and phase correction of *k*-space data. If data is rotated, it may then need to be regridded onto the Cartesian coordinate system so that the Fourier transform can be applied. Various methods for doing this exist specifically for use with navigator echoes [50].

Navigator techniques have been successfully combined with spiral imaging. One example by Moriguchi et al. [51] uses a circular 'navigator ring' that is identical for each interleaved spiral in the trajectory. Data in the navigator ring can be compared to identify rigid-body rotations and translations that occurred between acquisition of each interleaved spiral.

Recent attempts have also been made to combine parallel imaging with navigator echoes. One approach by Bydder et al. [52] uses SMASH (simultaneous acquisition of spatial harmonics) to obtain navigator information. Instead of using SMASH to reduce acquisition time, it is used to produce redundant data. This can then be compared to data measured

at a different time to determine motion parameters. Parallel imaging can also be used to synthesise missing *k*-space data [53] once motion has been determined using navigators.

Many modified versions of navigator echo techniques exist [54, 55] but none make use of all the collected data for motion correction purposes, reducing scan efficiency. Some techniques do obtain motion information from *some* of the data that will eventually be used for image reconstruction. Such sequences are often referred to as 'self-navigating' (see [56] for example). The most well-known of these is PROPELLER MRI. This is the topic of the next section.

3.4.2 PROPELLER

Perhaps the most widespread motion-correction technique available is PROPELLER (Periodically Overlapping Parallel Lines with Enhanced Reconstruction) MRI, first proposed by Pipe [57]. PROPELLER MRI has subsequently been shown to be effective in reducing motion artifacts in both simulations [58, 59] and clinical trials [60] (initially T_2-weighted imaging only). Since work began on this thesis, the PROPELLER sequence has been installed on three of the four MRI scanners in Christchurch.

A description of the original implementation of PROPELLER, as first described by Pipe, is given here in brief. It consists of six distinct steps:

1. Data acquisition
2. Phase correction
3. Rotation correction
4. Translation correction
5. Through-plane motion detection
6. Final reconstruction

Data acquisition in PROPELLER is normally described as radial (rather than Cartesian). Although data are collected in rectangular strips using FSE, the strips (often referred to as 'blades') are rotated about the centre of *k*-space (Fig. 3.5). This results in a region of overlap between each strip near the origin. This is used to obtain information about the motion of the object (steps 3 to 5 above).

The first step in reconstructing an image from the PROPELLER data is phase correction. This ensures that each *k*-space strip is centred exactly on the *k*-space origin. This is achieved

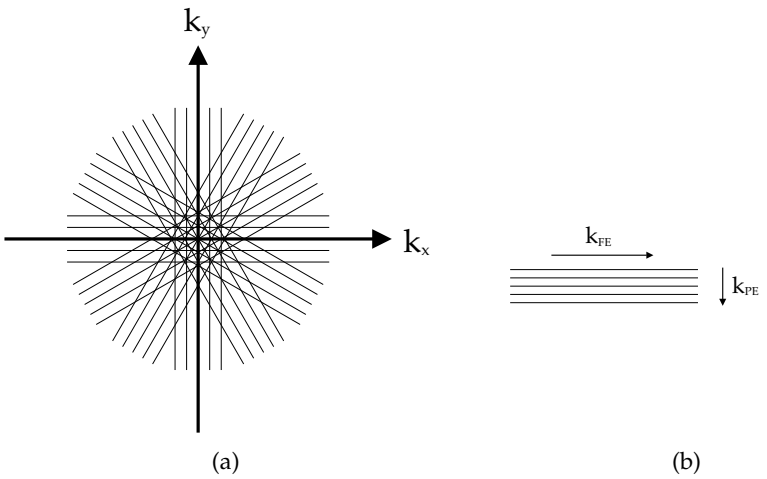

Figure 3.5 (a) The *k*-space trajectory used by PROPELLER. It consists of a number of concentric, rectangular strips. The centre of *k*-space is heavily oversampled while the periphery is minimally sampled. (b) The frequency-encode direction runs lengthwise along each strip, which is acquired using FSE.

by windowing each strip with a pyramid function and removing the phase of the windowed data from the original data in image space (refer to [57] for specific details).

The next step is bulk rotation correction. A correlation approach is used, whereby the correlation of each strip with the 'weighted average' of all strips is found as a function of rotation angle. A second-order polynomial is fitted to this function and the peak is taken to be the angle of rotation for the given strip. The strip coordinates in *k*-space are then rotated to correct for this.

Translational motion is quantified by again comparing the data in the central circle between strips. An average data set from all strips is formed and used to generate a low-resolution image. A similar image is produced for each individual strip. Translation parameters are then estimated by finding the location of the maximum value of the convolution of the two images. Removing the corresponding linear phase from each strip in *k*-space then corrects for this.

Through-plane detection and correction in PROPELLER merely involves discarding strips that do not match well with the average data set. Poor correlation is assumed to indicate through-plane motion or any other effect previously unaccounted for.

A number of improvements to the original PROPELLER algorithm have been suggested. Some of the more recent and notable suggestions include:

- Undersampling of *k*-space combined with PROPELLER [61]. The aim here is to im-

prove acquisition time: PROPELLER takes approximately 50 % longer than multiple-shot FSE to fill *k*-space. The problem is that undersampling is also possible for multiple-shot FSE (half-Fourier imaging, for example) so such methods are unlikely to reduce the gap between the two techniques in terms of speed.

- Improved approaches to motion detection in PROPELLER, such as that proposed by Patch et al. [62]. A system to change the order of rotation and translation detection has been proposed [63]. Also, the effect of changing the various PROPELLER parameters on motion correction has been studied [64].

- The combination of parallel imaging (discussed in more detail in Appendix A) with PROPELLER [65, 66].

- The use of EPI for acquiring the PROPELLER blades [67,68]. EPI has also been used to acquire PROPELLER blades with the frequency-encode and phase-encode directions reversed [69]. This is an interesting approach and one that may be applicable to the TRELLIS technique discussed later in this thesis.

- Approaches to generate T_1-weighted images using PROPELLER [70, 71].

- The application of PROPELLER to diffusion-weighted imaging [72, 73, 67]. This is of particular interest due to the sensitivity of DWI to motion. PROPELLER DWI has been shown to be advantageous in some situations [74].

- Improved methods of gridding and image reconstruction from PROPELLER *k*-space data [75].

PROPELLER is not used only for the correction of head motion. It has also been applied to imaging of the pelvis [76], with no resulting penalty over respiratory-triggered fast spin echo (RT-FSE) but with less motion tolerance than single-shot fast spin echo (SS-FSE). Diffusion-weighted PROPELLER has also been shown to be promising for imaging abdominal organs [77].

Despite its success, and the high level of interest it has generated, PROPELLER is not without its disadvantages. The original version takes longer to acquire data than conventional scans by a factor of $\pi/2$ [57]. Hence, it may sometimes be better to use a faster scanning technique to minimise the motion occurring during the scan time. This conclusion is somewhat supported by research such as that presented by Forbes et al. [78] where PROPELLER is compared to a single-shot fast spin-echo (SS-FSE) sequence. In this case it was found that the two sequences provide equal motion insensitivity although PROPELLER did provide better assessment of the brain tissue characteristics.

Other disadvantages include ring artifacts [79] and coloured noise problems [80]. The latter was also noted by Tamhane et al. [81], who compared the effect of noise at high spatial frequencies between PROPELLER and Cartesian sampling methods. As stated in Pipe's original paper, '...the oversampling also results in increased SNR' [57]. This is, of course, true. The trouble is that the noise is then no longer white but instead is coloured. The increased SNR is due to oversampling at the centre of *k*-space. Thus, SNR is improved here (where it is already high) and not at the edges of *k*-space (where the noise floor may approach the level of the signal).

3.4.3 Motion tracking and correction

It is possible to monitor subject motion using some external mechanism and use this information to correct for motion, either after the scan (retrospective correction) or during the scan (real-time correction).[2] Although neither of these approaches are widely used in practice, several successful systems have been implemented.

Motion tracking with retrospective correction requires both an external tracking system and a system of post-processing the data to correct for detected motion. Real-time motion correction offers an added benefit. Motion of the imaged object is monitored throughout the scan and the scanner gradients are simultaneously adjusted to 'track' the object using the knowledge of its motion. This is achieved by passing the six parameters representing position and orientation in a 3-D space to the scanner (Fig. 3.6). No special post-processing is then needed.

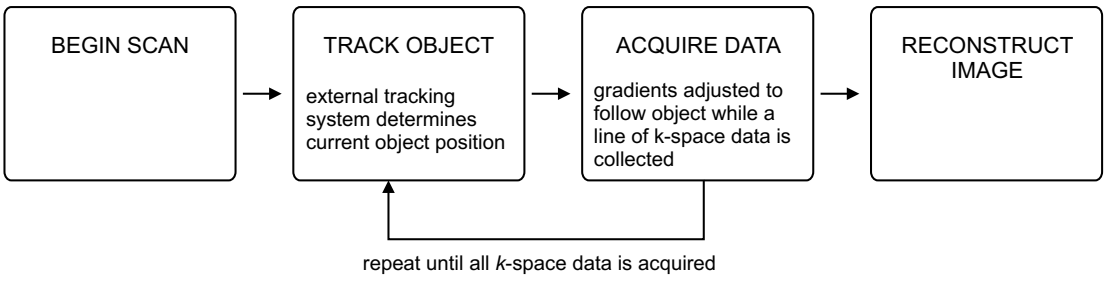

Figure 3.6 A flowchart depicting a possible real-time tracking system to prevent motion artifacts. The gradient fields are adjusted to follow the object being scanned. No special post-processing is required to reconstruct the final image from the *k*-space data.

The general concept of real-time gradient adjustment has existed since at least 1997 [82]. Since then, some progress has been made towards producing a useful system.

An early example was by Derbyshire et al. [83], where motion tracking of the subject was carried out using three 'locator coils', containing a copper sulfate solution to provide a

[2] Real-time correction is commonly referred to as 'prospective' motion correction; however, the author finds this terminology misleading so will avoid it here.

signal, in a fixed triangular configuration. A feedback system was used to update the scan plane. This system demonstrated real-time motion correction between images, but no attempt was made to correct for motion within an image.

As early as 1999, work was carried out using a laser detection device to track motion [84]. Three lasers and three solid-state position detectors were used. Each laser illuminated a reflector on the head of the subject. The angle of reflection then indicated the position of the head and the gradients were adjusted to compensate. In this case good results were claimed; however, no experimental data or images were presented in this single-page abstract.

In 2000, Thesen et al. [28] published their technique known as PACE (Prospective Acquisition CorrEction). This was designed to help with head motion in fMRI. Again, however, this method deals with the registration of entire images. In 2003, Peshkovsky et al. [85] demonstrated subject tracking using a deuterium crystal. This was rotation correction on a single axis only, however. Ultrasound has also been used to track motion in conjunction with MRI [86]. One obvious disadvantage is the extra hardware required and the resulting complexity and expense.

One study in 2005, by Tremblay et al. [87], used a tracking system that reflected infrared light off markers attached to the subject. This was used in conjunction with a retrospective correction system. While this was between whole images (for fMRI purposes) rather than within an image, the tracking system proved itself as an effective means of monitoring subject motion.

More recently, in 2006, Zaitsev et al. [88, 89] demonstrated a system using cameras to track a optical marker held in the mouth of a patient. A dental cast was used to provide better contact between the mouthpiece and the subject (similar to methods designed to restrain the patient - see Section 3.2.1). This produced excellent results. The question remains, however, as to whether or not this system would work for a genuinely uncooperative patient. Also, the system requires a clear view down the scanner bore to the optical marker. Perhaps an endoscopic system, such as that used in eye-tracking for MRI [90], could be applied to solve this problem.

Unlike navigator echoes or the PROPELLER sequence, the real-time tracking and gradient adjustment approach has the advantage of not requiring redundant sampling of k-space, hence saving acquisition time. It can also be applied to any existing pulse sequence and would be a good for correcting through-plane motion as it would for in-plane motion. The question is, why has it not been taken up clinically? One obvious disadvantage is that the motion must be genuinely 'rigid body'. For example, if the motion of a marker fixed to the outside of the skull does not accurately reflect brain motion for some reason,

then this approach will fail. Another disadvantage is the need for calibration. In MRI, the operator can select any slice of their choice without moving the patient (assuming that the appropriate receive coil is fitted at the time). This advantage could be lost with the addition of items such as cameras, lasers, detectors or mirrors. To be clinically useful any system must be reliable and easy to use, even with an uncooperative patient.

It would seem that this approach may well be successful in the future. The problems lie not in the technical development of a working prototype but rather in the physical construction of a system capable of performing reliably in the clinic.

3.4.4 Post-processing techniques

Various mathematical approaches have been proposed to correct motion effects in images after data collection, such as those presented by Yang and Smith [91] and Bourgeois et al. [92]. Unfortunately, such techniques are normally very limited: sometimes a motion-free reference image is required; sometimes motion is restricted to one dimension, or other simplifications or assumptions made that do not hold in practice.

An autofocus method has been proposed by Atkinson et al. [93]. This can reduce motion artifacts using an optimisation procedure that finds the patient motion that minimises a focus criterion – entropy in the image, in this case. Results obtained have shown some improvements in motion artifact levels. A similar technique has also been combined with parallel imaging [94].

A technique has also recently been published by Batchelor, Atkinson et al. [95] which represents the problem of motion corruption using a matrix equation: this gives the corrupted image in terms of the ideal version. The goal then becomes the inversion of the system; this would give the ideal image given the corrupted version as in input. The inversion is performed using the LSQR routine in MATLAB® (this uses a conjugate gradient approach). This requires a cost function to assess the image and to allow the algorithm to converge (again, entropy is used).

The type of sequence the above technique is applied to is multiple-shot imaging, where the object moves between shots. The authors claim that the main disadvantage of this approach is computation time. Convergence also seems to be a possible problem, however. A starting estimate of the motion needs to be provided to obtain good correction. In addition, the motion parameters must be highly constrained. For example, the only in vivo result provided is an axial image of two legs. The motion is constrained to the movement of one leg relative to the other.

The methods discussed above have the advantage that, in most cases, no sequence modifi-

cation is required. Results so far, however, have not been as promising as the other methods mentioned in this chapter and it seems that there is some way to go before these methods will be clinically useful for correcting bulk head motion.

3.5 Conclusions

Motion problems have plagued MRI since its introduction. Satisfactory solutions have been developed for some types of motion, such as cardiac motion or respiration. Rigid-body motion, however, still poses a problem. Such motion causes inconsistencies in *k*-space, which leads to artifacts in the final image. A number of methods to alleviate this problem have been proposed; some of these are currently used clinically. Table 3.1 provides a summary of the main methods.

Technique	Main advantages and disadvantages
Physical restraints	Simple and fairly easy to use but can add to patient discomfort. Not completely effective.
Sedation	Very effective in some cases but has safety concerns.
Training	Safe and effective but only suitable in very specific cases.
Fast imaging	A useful technique but suffers from poor image quality.
Radial imaging	Some robustness to motion but not completely effective. Increased acquisition time.
Navigator echoes	Increased acquisition time. Limited success for rigid-body head motion.
PROPELLER	Highly effective in some situations. Increased acquisition time and relatively poor SNR for high spatial frequencies.
Real-time tracking	No special post-processing required. An external tracking mechanism is needed.
Post-processing	No sequence modification required but success is limited so far. Computation time can be a limiting factor.

Table 3.1 A brief summary of strategies used to help reduce artifacts from rigid-body head motion.

This thesis describes the development of an imaging method that aims to avoid the disadvantages of some of the techniques listed in Table 3.1. In particular, the focus is on deriving an acquisition method with no external hardware requirements but without an increase in acquisition time over conventional scans. More specifically, the aim is to find a technique that can use all the collected data for *both* image reconstruction and motion detection.

Chapter 4

MR Phantoms

As described in the previous chapter, a wide variety of techniques have been proposed to ameliorate the effects of patient motion in MRI. It is important to have a means to test and compare different techniques. Such testing must be repeatable, and in this respect phantoms (test objects that can be imaged) are preferable to human subjects. Phantoms can be divided into two categories: computational phantoms and physical phantoms. This chapter discusses both.

4.1 Computational phantoms

The analytical Shepp-Logan head phantom (Fig. 4.1) is useful for simulation purposes. The phantom was originally designed to be 'a reasonable model of a section of the skull' [96]. The bright region on the outer edge, for example, is analogous to bone, while the small circular feature at the bottom centre represents a tumor. The grey levels in the original version, shown in Fig. 4.1(a), were chosen to represent the radiographic density variations in the human brain, as the phantom was originally developed for X-ray imaging. In MRI, radiographic density is not the measured parameter and therefore the original grey levels are inappropriate. For this research, the modifications made by Pan and Kak [97] are useful: these provide improved contrast for viewing purposes. The phantom shown in Fig. 4.1(b) is generated using the parameters in Table 4.1 which are taken directly from [97]. Unless stated otherwise, the analytical phantom used throughout this thesis is generated using these parameters, although in some cases the dimensions are scaled.

MATLAB® code written to analytically generate the k-space data corresponding to the Shepp-Logan head phantom is based on that written by Blakeley [98]. This was modified by the author to allow the introduction of motion during data acquisition.

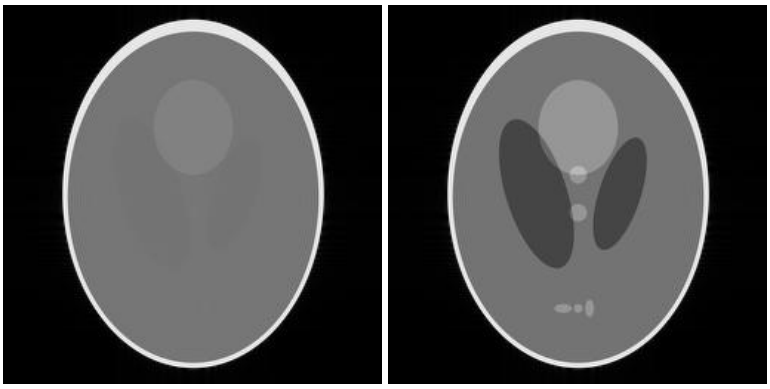

(a) (b)

Figure 4.1 The Shepp-Logan head phantom in (a) and (b) consists of the sum of 10 ellipses and is useful in medical imaging because its Fourier transform can be calculated analytically. The parameters originally specified produce the phantom in (a) as they correspond to density variations in human tissue. The parameters given in Table 4.1 produce the phantom in (b); this is much more convenient for display purposes.

ellipse	centre coordinates	major axis	minor axis	rotation angle	grey level
a	$(0, 0)$	0.92	0.69	$90°$	1.0
b	$(0, -0.0184)$	0.874	0.6624	$90°$	-0.5
c	$(0.22, 0)$	0.31	0.11	$72°$	-0.2
d	$(-0.22, 0)$	0.41	0.16	$108°$	-0.2
e	$(0, 0.35)$	0.25	0.21	$90°$	0.15
f	$(0, 0.1)$	0.046	0.046	$0°$	0.15
g	$(0, -0.1)$	0.046	0.046	$0°$	0.15
h	$(-0.08, -0.605)$	0.046	0.023	$0°$	0.15
i	$(0, -0.605)$	0.023	0.023	$0°$	0.15
j	$(0.06, -0.605)$	0.046	0.023	$90°$	0.15

Table 4.1 Ellipse parameters from Pan and Kak [97] used here to generate the Shepp-Logan phantom in Fig. 4.1(b).

4.1.1 Motion

A simulator was developed by the author that generates a motion-corrupted *k*-space data set using the analytical Shepp-Logan phantom. This can then be transformed into the corresponding motion-corrupted image using the inverse DFT.

The simulator accepts a number of parameters, some of which can be modified using a graphical user interface (Fig. 4.2). These parameters fall into three main categories:

- Phantom parameters: phantom size (relative to the field-of-view); *k*-space matrix size, N_{kx} and N_{ky}, (equivalent to the final image resolution); and the SNR.

- Acquisition parameters: the order in which *k*-space data is acquired (i.e., the *k*-space trajectory).
- Motion parameters: rotation and translation (x- and y-directions).

Based on these inputs, the simulator computes *k*-space data points corresponding to the Shepp-Logan phantom specified. When motion is simulated, the position of the phantom varies between *k*-space values. The position used in the calculation of each *k*-space data value is determined by the specified *k*-space trajectory and the motion parameters.

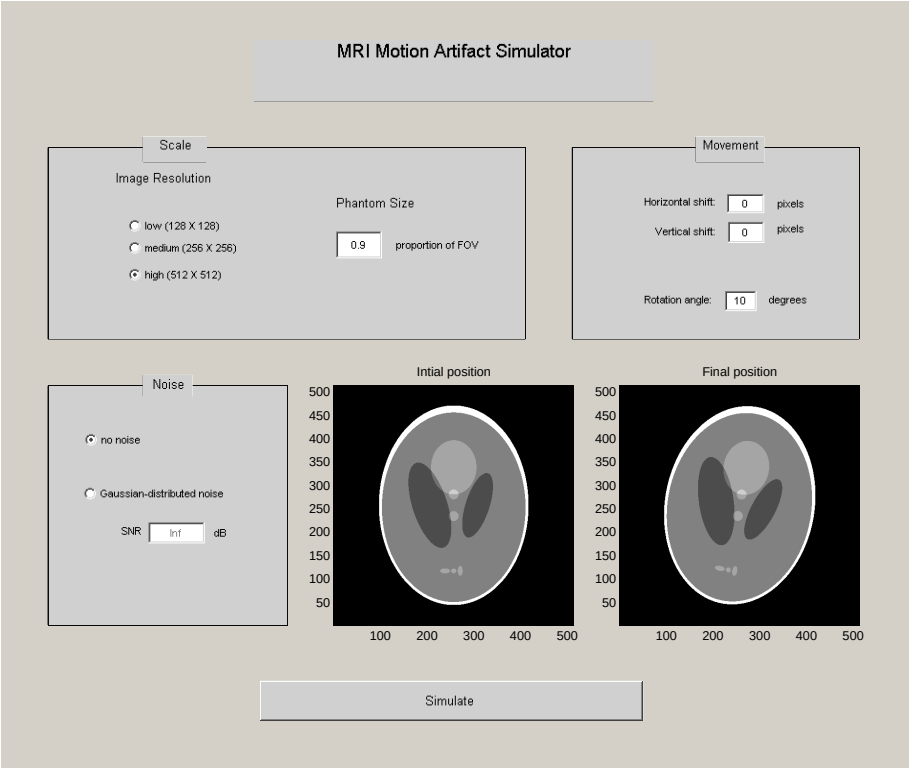

Figure 4.2 The MRI motion artifact simulator developed by the author. Frequently used parameters can be modified here; other options, such as the selection of different trajectories, can be altered by changing settings within the MATLAB® code.

Pseudo-random Gaussian white noise is added directly to the *k*-space data. Initially, the complex noise component for each point in *k*-space, (u, v), is generated using

$$n(u, v) = x_1 + ix_2 \ , \tag{4.1}$$

where both x_1 and x_2 are samples of a normally distributed random variable with zero mean and a variance of one. The total noise energy required is computed by rearranging Eq. (2.12) and using the SNR specified by the user. The set of values generated using

Eq. (4.1) are then scaled so that the total noise energy required is achieved.

4.2 Physical phantoms

Physical phantoms are often used in medical imaging, and in MRI in particular, for quality assurance purposes. They are useful for verifying parameters such as the SNR, contrast-to-noise ratio (CNR), geometric distortion, and slice profile. They also provide a means to assess image sharpness, since the phantom may be made with virtually perfect boundaries between materials. Phantoms for MRI often use dilute solutions to provide a signal, with T_1 and T_2 normally shortened compared to water to reduce imaging time and to be more comparable with tissue. This is commonly done by adding paramagnetic metal ions (often nickel, manganese or copper) to the water.

Although commercial phantoms were readily available for this research, none were suitable for use in experiments simulating motion (moving phantoms are discussed later in this section). A phantom was therefore designed and built by the author. One slice of this phantom is modeled on the Shepp-Logan analytical head phantom: this enables direct comparison between the physical phantom and the computational version (where *k*-space data can be computed exactly, as described earlier).

The phantom is constructed of polycarbonate layers glued together and mounted inside an acrylic cylinder. Each layer was laser cut to achieve a precise shape. The resulting 3-D surface has varying thickness as shown in Fig. 4.3 (a). The phantom contains dilute copper sulfate ($CuSO_4$) solution to generate a signal. Polycarbonate and acrylic produce zero signal – this difference results in images with good contrast. Copper sulfate was selected for its low toxicity (compared to $NiCl_2$, for example) and availability. Specifically, the solution was 1.25 g/L $CuSO_4.5H_2O$ (5 mmol), with the concentration chosen to reduce T_1 and T_2 to levels consistent with achieving a realistic contrast in a reasonable acquisition interval. Although T_1 and T_2 values have not been directly measured, the author estimates a T_2 of approximately 250 ms using values reported for copper sulfate solution of this concentration at 1.5 T [99].

The range of intensities required to produce a good approximation to the Shepp-Logan phantom are generated through the partial volume effect (when a voxel contains more than one type of tissue or material). To achieve this, the phantom must be imaged using a slice thickness of 10 mm and all polycarbonate layers must be contained within one slice. A reconstructed image of the physical Shepp-Logan phantom is given in Fig. 4.3(b). The small imperfection at the base of the phantom is caused by an air bubble in the copper sulfate solution.

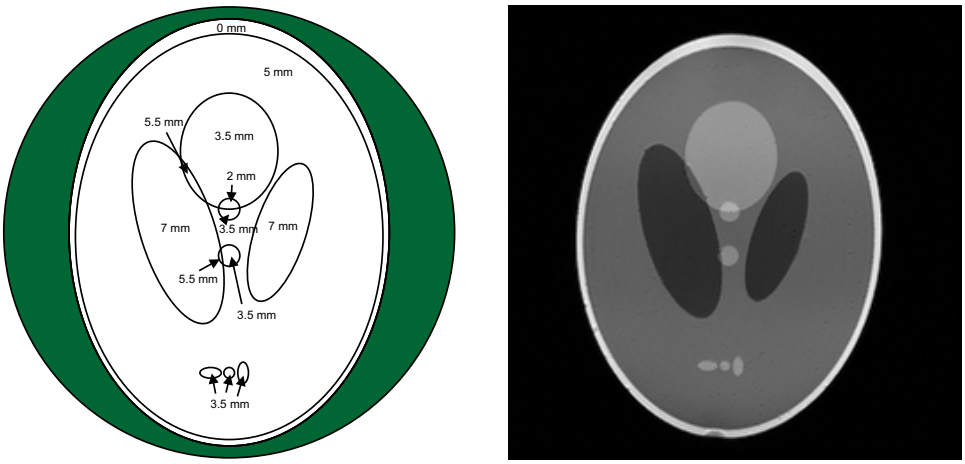

(a) (b)

Figure 4.3 The physical Shepp-Logan phantom construction (a) showing thicknesses of polycarbonate in the imaged slice. The shaded region surrounding the outer ellipse is made of acrylic. When scanned using a slice thickness of 10 mm, the image shown in (b) results.

The layers of polycarbonate combined occupy less than half the depth of the cylinder. The remaining space contains two further circular disks featuring imageable shapes: a kiwi on one disk; and a fern leaf and 'NZ' on the other (Fig. 4.4). Sufficient spare depth remains to allow a uniform circular disk containing only fluid to be imaged as well.

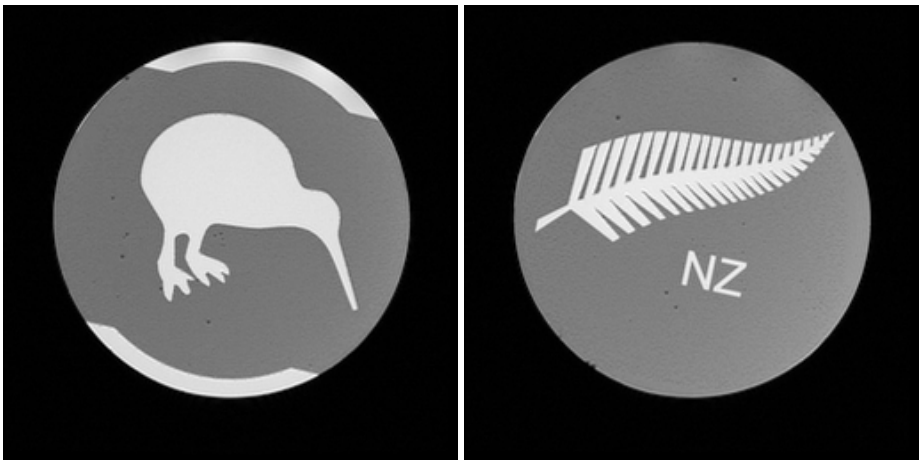

(a) (b)

Figure 4.4 MR images of the two additional slices in the phantom constructed by the author.

An experiment was performed to compare images generated using the analytical Shepp-Logan phantom with those obtained by scanning the physical version. The phantom was imaged on a 1.5 T scanner (GE Medical Systems) using a fast spin echo sequence (FSE-XL, 256 $\times$ 256 resolution, N_{etl} = 3). Images were reconstructed directly from the raw data

without explicit filtering of k-space.

Fig. 4.5 compares an image of the analytical Shepp-Logan phantom to the image of the physical phantom shown earlier in Fig. 4.3(b). The SNR used in the generation of the analytical phantom was 34.7 dB, chosen to match the SNR in the image of the physical phantom. Likewise, the analytical phantom was rotated by 2.2° to match the physical version. It is evident, from both the image-space and k-space magnitudes, that the two phantoms are very similar. In *k*-space there appears to be less obvious structure and lower magnitude in the higher frequency components of the physical phantom compared to the analytical version.

Another interesting difference is the reduced amount of Gibbs ringing in the physical phantom compared to the analytical phantom. This discrepancy is apparent in both the phase-encode and frequency-encode directions. A cross-section shows this more clearly than the images themselves: an example is given in Fig. 4.5(e) and (f). This is taken horizontally through both images on the left side of the outermost ellipse (marked with a black line on the images).

To investigate this further, a second comparison between a simulation and a physical phantom is made (Fig. 4.6). A slice containing uniform copper sulfate solution confined within the circular cylinder was imaged simultaneously with the Shepp-Logan phantom already discussed (multiple slices were acquired in the same scan). An analytical version of this object was computed by calculating the Fourier components of a circular region of a similar size and then adding noise. The analytical *k*-space data set in Fig. 4.6(c) is very similar to the physical data set in Fig. 4.6(d). Cross-sections from the images in Fig. 4.6(a) and Fig. 4.6(b) are shown in Fig. 4.6(e) and (f). Again, the position of the cross-section is marked with a black line. The images exhibit very similar amounts of Gibbs ringing.

Why are Gibbs artifacts reduced for the physical Shepp-Logan phantom compared to simulations but not for the circular disk imaged during the same scan? The author suggests this is because the laser-cut edges of the polycarbonate sheets are slightly rounded, whereas perfectly sharp edges are modeled in the analytical version. In the case of the circular disk, edge sharpness is defined by the smoothness of the inner wall of the acrylic tube. This is presumably very smooth. Thus, the edge of the disk is very sharp; hence, high frequency components play a greater part in the Fourier representation of this object, truncation of *k*-space is more pronounced, and Gibbs ringing results.

The above suggests that the (infinitely) sharp edges in the analytical Shepp-Logan phantom are unrealistic in a physical object and that this difference is of some practical significance. This may be important for researchers who use the analytical Shepp-Logan phantom in simulations involving Gibbs ringing, such as in [100]. Multiplying the magnitude of the

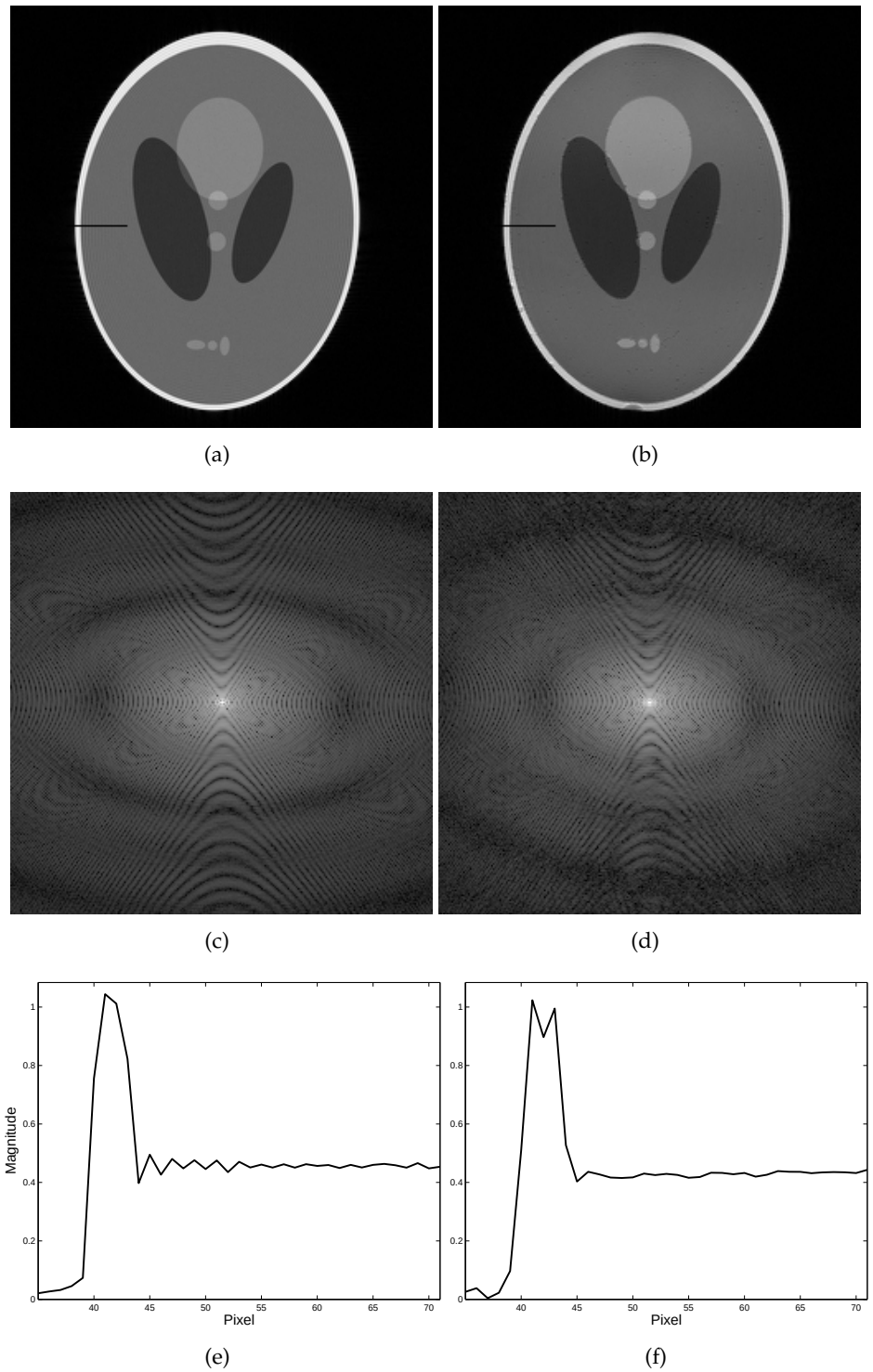

Figure 4.5 A comparison between images of the analytical and the physical phantom: (a) and (c), the analytical phantom magnitude in image-space and k-space; (b) and (d), the physical phantom magnitude in image-space and k-space. A log scale is used to show k-space magnitudes. The resolution in both cases was 256×256. Cross-sections of (a) and (b) (position indicated by the black horizontal lines) are shown in (e) and (f) respectively. Gibbs ringing is more apparent in (e) than in (f).

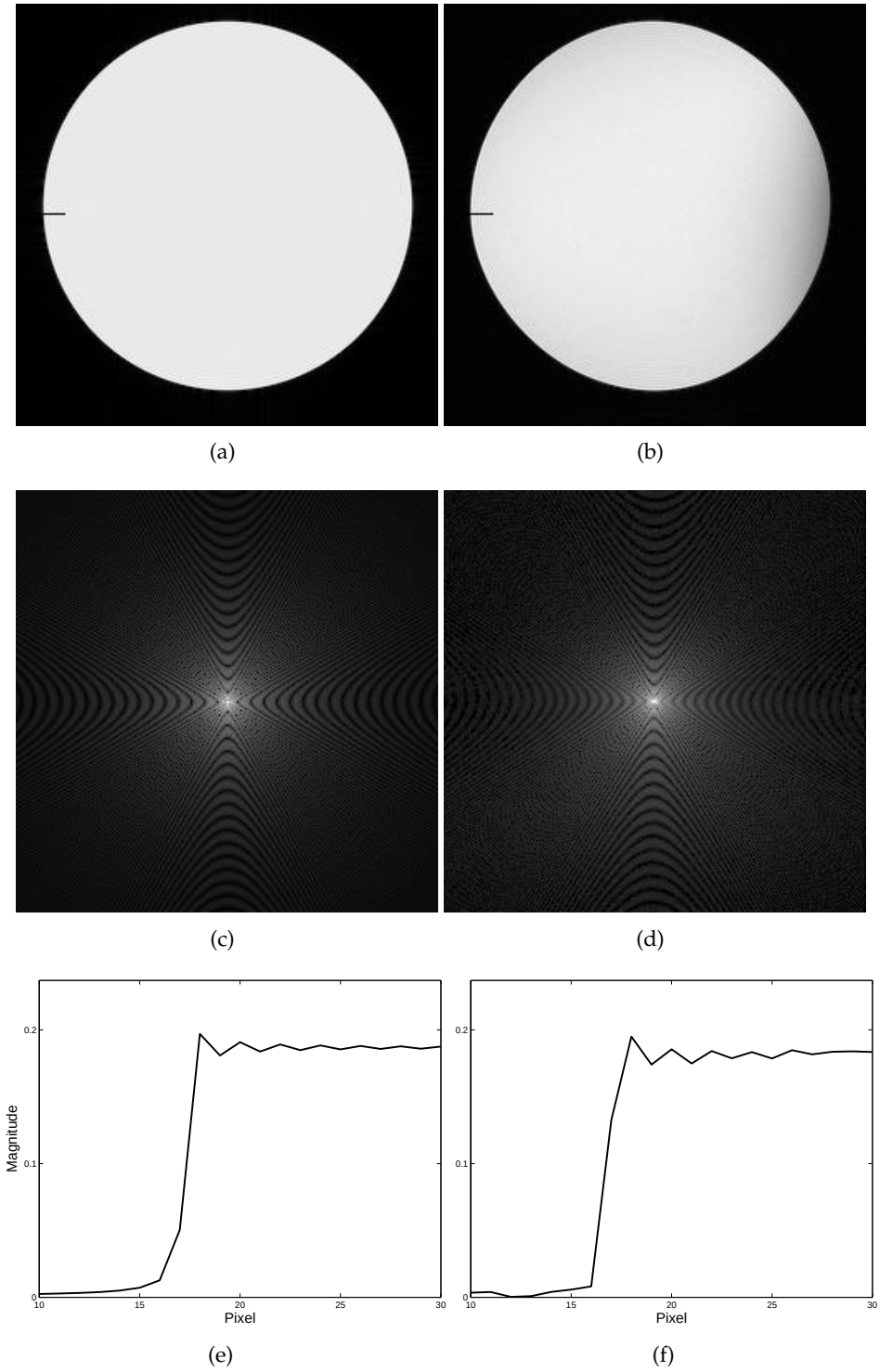

Figure 4.6 A comparison between magnitude images of a computer-generated circular phantom (a) and a slice through the physical phantom (b) consisting of only $CuSO_4$ solution inside the acrylic cylinder. The corresponding *k*-space magnitudes (log scale) are given in (c) and (d). Cross-sections of (a) and (b) (position indicated by the black horizontal lines) are shown in (e) and (f) respectively. Approximately equal Gibbs ringing is present in both cases.

k-space data by a smooth two-dimensional window function has the effect of attenuating high spatial frequencies, thereby reducing Gibbs ringing in the image reconstruction and making the analytical *k*-space data set more closely approach the physical version.

4.2.1 Motion

The author is not aware of any commercially available moving phantoms suitable for MRI. There are, however, a number of custom-made moving phantoms described in the literature. Drangova et al. [101] constructed a computer controlled phantom from deformable silicone gel to mimic physiological motion. The motion achievable with this phantom includes bulk rotation and translation, rotational shear, axial shear, and combinations of some or all of these. Three stepper motors situated a safe distance from the scanner are used to drive three shafts connected to the phantom. Although the construction of such a versatile phantom was complex, the resulting motion is highly reproducible and motion such as the cardiac cycle can be imitated.

Leung and Plewes [102] tested their retrospective motion correction technique using a custom-made phantom, designed to mimic respiration. The phantom itself consists of agar gel in a circular mold doped with a standard MR contrast agent (Gd-DTPA) to reduce T_1 and T_2 times. Again, motion is applied using a stepper motor mounted at the end of the scanner patient table and transferred to the phantom using a single long plastic shaft. Motion is limited to a repeating cycle of rotation and translation together (these are not separable) as only a single motor is used.

A less sophisticated, but more affordable solution has been developed using a commercially available K'NEX construction set (Hyper Space Training Tower, K'NEX Industries, Inc., Hatfield, PA) by Huber et al. [103]. This produces periodic motion with simultaneous translation and rotation designed to simulate cardiac or respiratory motion. The design was deliberately chosen for its low cost. Again, a motor is connected to a rigid rod to transfer motion to the phantom itself. This is not a stepper motor, however, but a low-cost K'NEX 12 V DC motor.

As mentioned in Section 3.4.3, ultrasound has been used to track motion in conjunction with MRI by Günther et al. [86]. The authors developed a moving phantom to test their system. This phantom generated sinusoidal displacement at two different frequencies (about 1 Hz and 1/6 Hz) to simulate cardiac and respiratory motion. The phantom was based on the work discussed above and was also constructed of K'NEX. The object being moved was a water-filled balloon. The source of motion was again an electric motor outside the magnet and again plastic rods and gears were used to move the balloon.

An even simpler system has been used to rotate a pineapple inside the scanner by van der

Kouwe et al. [104]. A pineapple was used due to its good internal structure and contrast. It was connected to a plastic shaft and then to a motor situated outside the scanner bore. In this case the only motion achievable was rotation about a single axis.

Although varying in complexity, all the systems above use a motor connected to a plastic drive shaft to maintain a safe distance from the scanner. This also requires a control system for the motor to be located in the same room as the scanner. While metallic items can be taken into the scanner room, this is generally undesirable for reasons of safety and, in the case of a motor, RF interference. An alternative system was therefore developed and is described in the following.

A pneumatic moving phantom

A moving platform for the phantom described earlier was designed and built by the author with the assistance of workshop staff. It is constructed entirely from non-metallic materials so as not to affect the magnetic field homogeneity in the scanner or pose a safety hazard. The platform and phantom are shown in Fig. 4.7.

Two 60 mL plastic syringes act as pneumatic actuators: one translates the platform while the other rotates it. They can operate simultaneously or independently. Compressed air and vacuum is coupled to the syringes through 10 m of plastic pipe. This is sufficiently long to reach from the magnet room through a built-in waveguide into the control room; thus, there are no metallic components in the scanner room. Also, no wires (potential sources of RF interference) are needed to connect the phantom inside the scanner room with the control system outside.

In the control room, a pneumatic system designed by the author manipulates the pressurised air or vacuum connected to each pipe. The control unit for this system consists of a programmable logic controller (PLC) designed for real-time operation. This generates a repeatable motion sequence. When used in the hospital, the apparatus is connected to the hospital's 400 kPa air supply. For testing purposes away from the hospital, a 50 L portable air tank is used; in either case, regulators in the pneumatic system maintain a constant air pressure. Any compressed air supply can be used to fill the tank.

A video tracking system has also been developed to independently quantify the motion of the phantom. To date, however, this has only been used outside the MR environment. This system is discussed further in Chapter 8, where results using this and those from the author's TRELLIS algorithm are compared.

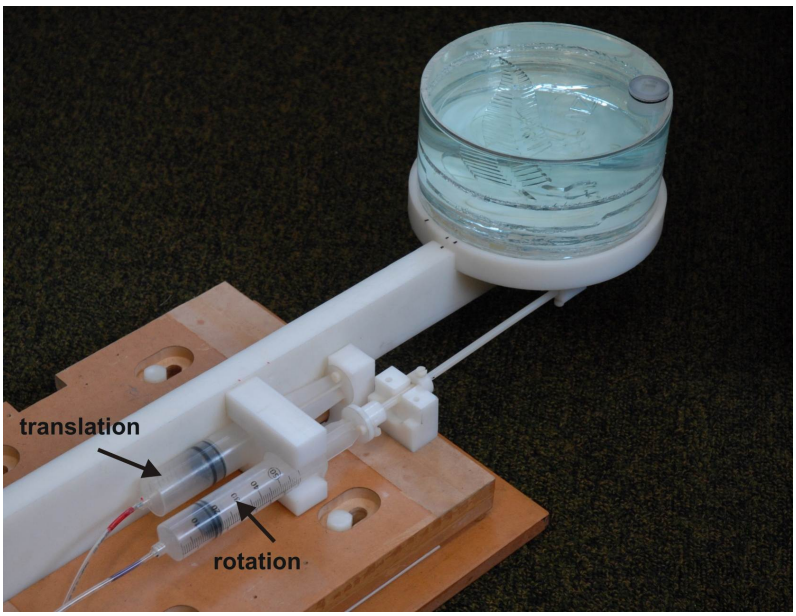

Figure 4.7 The moving phantom. Translation (along a single axis only) and/or rotation are achieved using a pneumatic system. Air is fed to syringes which then act as actuators to move the platform holding the phantom. The entire construction is MR-compatible with no metallic components.

4.3 Summary

The analytical Shepp-Logan phantom has been adapted to test the effects of bulk motion in MRI. A simulator has been developed that allows imaging and motion parameters to be modified easily. A physical phantom has also been constructed. One slice of this phantom has been modeled on the Shepp-Logan phantom, enabling comparisons to be made with simulations. A computer-controlled moving platform has been designed and built. This has no metallic components so is safe for use in an MR environment.

These tools allow testing of motion-correction techniques in MRI to be performed in a controlled and repeatable manner.

Chapter 5

MR Image Artifact Metrics

As well as using phantoms to conduct repeatable testing in MRI, it is important to be able to quantify the effect that different data acquisition and reconstruction methods have on the final image. This chapter compares a number of metrics that can be used for this purpose.

Provided that a reference image is available, and the object is of limited extent, it is shown that a measure relating to the amount of energy outside the object support can be used to objectively compare the severity of motion-induced artifacts. This work has been published in the *Proceedings of SPIE: Image Reconstruction from Incomplete Data IV* [105].

5.1 Introduction

It would be useful to have a metric capable of providing a numerical measure of how badly an image is corrupted by artifacts. Most work reporting the testing of other correction algorithms (such as that presented by Pipe [57] and Forbes et al. [106]) relies instead on the visual appearance of the image. While not denying the importance of assessing images for their clinical utility, an objective metric allows the effect of subtle changes to an algorithm to be quantified.

There are several important considerations in the development of an image-comparison metric for motion-correction experiments. First, it is normally possible to produce some form of reference image to compare reconstructions to. This applies to all tests that might reasonably be carried out: an analytical phantom can be generated without introducing motion artifacts; a physical phantom can be imaged while stationary in the scanner; and a human subject can hold their head still during imaging.

Invariance of the metric to translation and rotation of the imaged object is critical. If an

image is motion corrected, the precise location of the reconstruction within the FOV may be unknown. Likewise, for in vivo experiments, it is difficult to ensure that the subject is in exactly in the same position in the scanner during acquisition of different sequences. The metric should be unaffected by such imprecision. As example, consider the images shown in Fig. 5.1. Apart from noise differences, test image (a) is identical to the reference image. The same applies to test image (b), although it is in a different position in the FOV and has been rotated. An image comparison metric would ideally produce the same result for both: the images show the same information and would be of equal diagnostic value. Images (c) and (d), on the other hand, are corrupted by motion artifacts; they therefore differ significantly from (a) and (b).

Invariance to image amplitude is not a useful feature here. If necessary, images can easily be scaled so that they have the same energy as the reference image. It can also be assumed that the relative size of the imaged object (analytical phantom, physical phantom or human head) and the FOV will not change between images. There is a need to compare reconstructions from the same subject, but no need to compare reconstructions from different subjects. This principle applies to the test images in Fig. 5.1: they are all of the same object and are all the same size.

In summary, a useful metric must produce the following results for the test images in Fig. 5.1: images (a) and (b) should be shown as virtually identical to the reference image; image (c) should be less similar to the reference image than (a) or (b); and image (d) should be the least similar to the reference. In the absence of changes in the imaged object or noise level, the difference between the test and (motion free) reference image can then be taken to quantify the level of motion artifacts in the test image.

In the following, several metrics are discussed:

- Mean squared error (MSE): a measure widely used for determining the difference between two images (or signals of any kind).
- Blur metric: a means of quantifying image blur by determining the 'edge width' of objects in the image.
- Difference in background energy (DBE): a new metric proposed here specifically to assess the severity of motion artifacts.

A number of other metrics exist. Image entropy has previously shown to be useful in MRI as a focus criterion for some of the methods discussed in Section 3.4.4 [107]. Its primary advantage, however, is the lack of a requirement for a reference image, which is not a useful feature here. Another possible technique is structural similarity [108, 109]. It is claimed

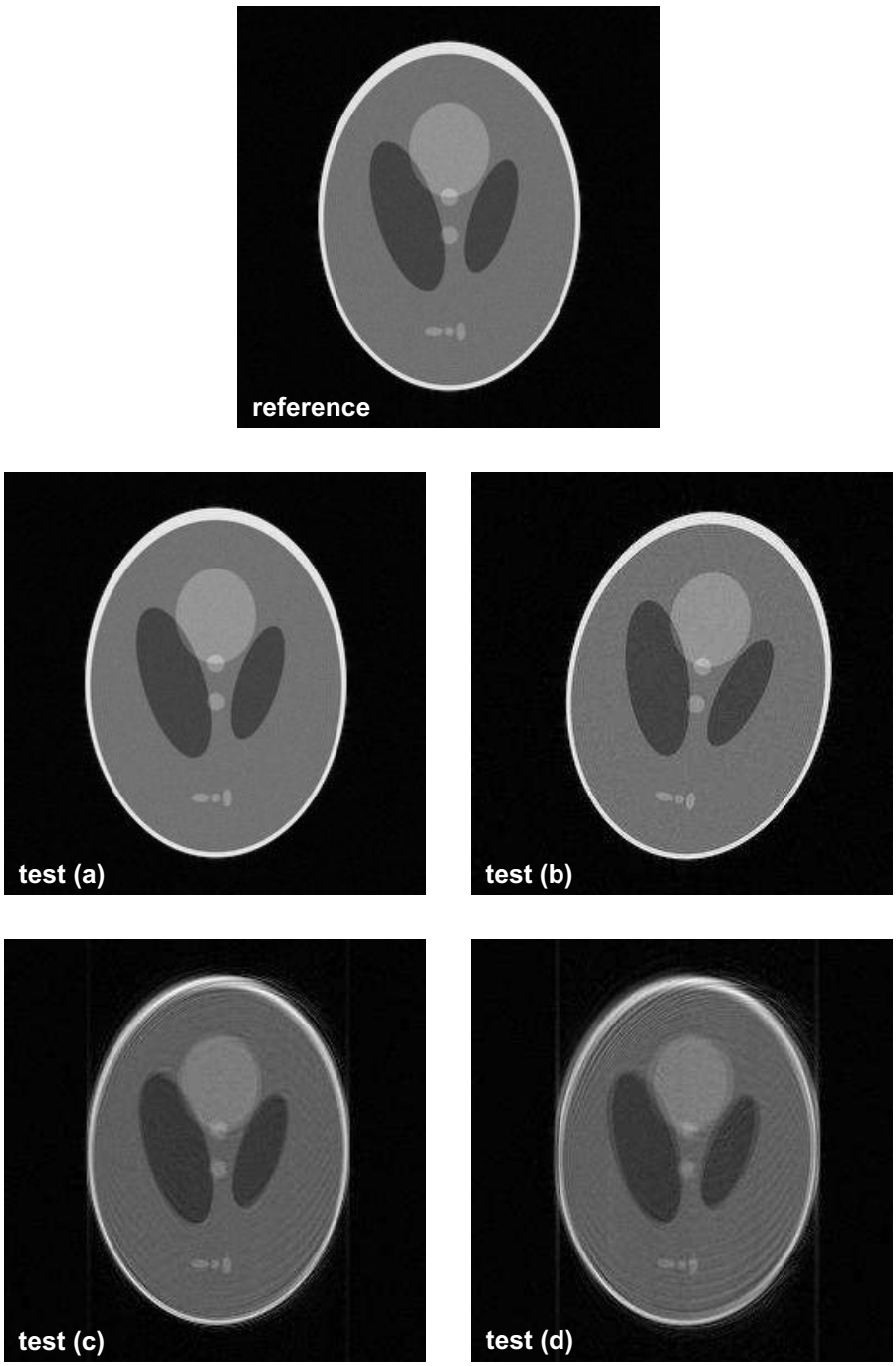

Figure 5.1 A reference image and four test images. The SNR used in all cases is 25 dB. Test image (a) is identical to the reference image except for noise differences. Test image (b) is offset by 10 pixels (to the right) and is rotated by 10degs. Test images (c) and (d) have motion added during the simulated acquisition, with the motion greater for (d) than for (c). A metric is sought that will show that test images (a) and (b) are essentially identical to the reference and will quantify the level of artifact in (c) and (d).

that this metric quantifies the effect of errors in an image on human visual perception more accurately than other techniques. It has, for example, been shown to be useful for evaluating the effect of errors in video encoding [110].

The author has briefly experimented with entropy and structural similarity measures and has had little success obtaining useful results. These two techniques may still be worthy of further investigation, however. This is left for future work.

5.2 Mean squared error (MSE)

A common metric for quantifying the difference between two images is mean squared error (MSE) defined for two images, the reference image, $R(x, y)$, and the test image, $T(x, y)$, as

$$\text{MSE} = \frac{1}{MN} \sum_{x=1}^{M} \sum_{y=1}^{N} (R(x, y) - T(x, y))^2, \tag{5.1}$$

where both $R(x, y)$ and $T(x, y)$ have dimensions $M \times N$.

MSE is not translation/rotation invariant. It could, however, be combined with an image registration algorithm to align the two images prior to computing the MSE. Unfortunately, even small errors in the image registration step significantly contribute to the MSE value (this is shown in Section 5.5). Despite this failing, MSE is so widely used it is included here for comparison with other metrics.

MSE is sometimes normalised by, for example, dividing the result in Eq. (5.1) by a quantity such as $\sum\sum(R(x, y))^2$. This is discussed in more detail when the mean squared error is used for a different purpose in Section 6.3. For the task at hand, however, the expression in Eq. (5.1) is sufficient.

When applied to each of the test images in Fig. 5.1, MSE values are: (a) 2.7×10^{-4}; (b) 4.7×10^{-2}; (c) 7.5×10^{-2}; and (d) 1.5×10^{-2}. The results suggest that test image (c) is the least like the reference image, followed by test image (b). This is not the image ranking required; however, since the images have not been registered, these results are not surprising.

Despite its disadvantages, MSE is still investigated further as a metric. For simulation purposes, translation/rotation invariance is not critical as it is possible to ensure the objects to be compared are properly aligned. This is done in a later experiment in this chapter.

5.3 Blur metric

Measuring the 'blur' of an image is an intuitive approach to quantifying reconstruction accuracy: a blur measure could be expected to increase with increasing motion corruption. It is also likely to be fairly rotation/translation invariant. For these reasons a 'blur metric' was developed, largely based on work reported by Marziliano et al. [111]. This metric does not require a reference image, although the result can be compared to that of the reference image if a relative measure is desired.

The blur metric is defined as the mean edge width of all edges located in the image. The process to find this value is summarised as follows:

1. Find all edges in the image.
2. Classify edges as horizontal, vertical or both.
3. Find the width of each edge.
4. Compute the mean edge width: this is the blur metric.

The edge detection process is shown in Fig. 5.2 for the reference image shown in Fig. 5.1. In Fig. 5.2(a), edges are identified using the method developed by Canny [112]. A Gaussian-smoothed version of the image is generated and local maxima in the gradient of this smoothed image are taken to be edges. A binary mask is formed which indicates the location of these maxima and thus corresponds to edge pixels in the original image. At this stage, detected edges are all one pixel wide.

Edges are then classified as 'vertical' or 'horizontal' and a corresponding 'edge mask' is formed, as shown in Fig. 5.2(b) and (c). Diagonal edges are classified as both vertical and horizontal. In this case it is possible to obtain two measurements from the same edge: one is the edge width in the vertical direction, the other the edge width in the horizontal direction.

The width of each edge is then estimated (see Fig. 5.3). Treating the vertical edges first, each row of the image is scanned. For pixels corresponding to an edge in the edge mask, the edge width is defined as the distance (in pixels) from the nearest local extremum left of the edge in the image to the nearest local extremum right of the edge in the opposite direction. If a local maximum is found left of the edge, a local minimum is sought right of the edge, and vice versa. The procedure is repeated for horizontal edges, using the columns of the image and the horizontal edge mask. This means that a particular pixel may be counted twice if it is classified as being on both a horizontal and vertical edge. The blur metric is then the mean edge width over all edge pixels.

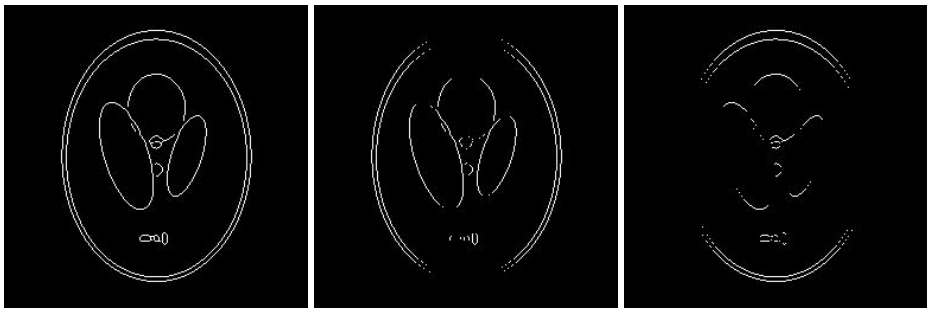

(a) (b) (c)

Figure 5.2 The edge detection process. The original image is the reference image in Fig. 5.1. Edges detected after application of a Canny filter are shown in (a). Two 'edge masks' are then formed: (b) a vertical edge mask and (c) a horizontal edge mask.

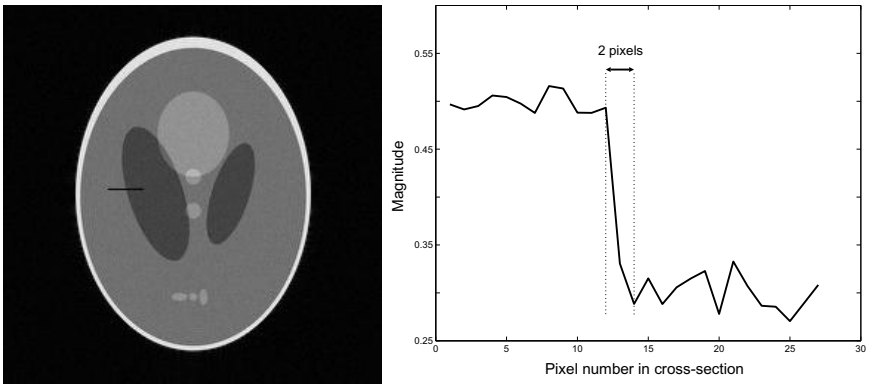

(a) (b)

Figure 5.3 Measuring the edge width: (a) the original image with a small cross-section marked in black; (b) the same cross-section showing an edge width measurement of 2 pixels.

When applied to each test image in Fig. 5.1, blur metric values (edge width in pixels) are (a) 3.3, (b) 3.3, (c) 4.7, and (d) 4.3. Unlike MSE, the blur metric has coped well with test image (c). Image (d), however, is classified as better than (c) according to the blur metric values. This is problematic.

The unexpected result with test image (d) is caused by the incorrect identification of edges. Fig. 5.4 illustrates this situation by showing edges detected for each image. If edges are incorrectly identified, their (meaningless) edge width affects the final result.

In summary, the blur metric may provide good results for very slightly blurred images for which it can still detect all image edges correctly. It is unreliable, however, for badly distorted images.

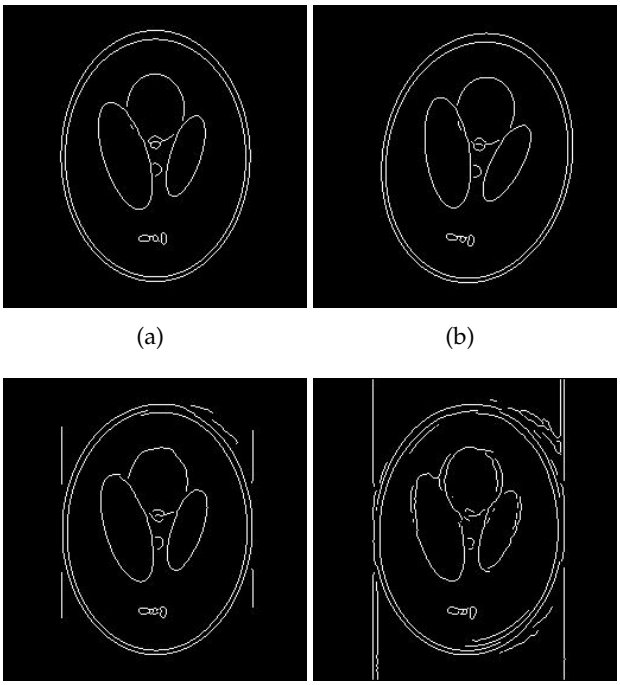

Figure 5.4 Images (a)-(d) show the edge identification results for the respective test images in Fig. 5.1. A large number of edges in (d) are identified incorrectly, leading to a failure of the blur metric in this case.

5.4 Difference in background energy (DBE)

In an MR image, pixels within the field-of-view (FOV) but outside the support region of the object should have a value close to zero in the absence of artifacts. The DBE measure exploits this property: it quantifies the amount of energy that has 'escaped' outside the support region as a result of image artifacts. It is only applicable when the support region is smaller than the FOV; in MRI, this is normally the case in brain imaging.

The principle behind DBE is that any energy outside the support region is the result of either noise or artifacts. This assertion can be demonstrated as follows. Let the field-of-view be Γ, partitioned into the support region, Ω_i, and the region outside the support, Ω_o, so $\Gamma = \Omega_i \bigcup \Omega_o$ and $\Omega_i \bigcap \Omega_o = 0$. In the absence of noise or motion, adequate sampling of the *k*-space data allows the object to be reconstructed entirely within Ω_i. If the object undergoes rigid-body motion that takes any part of it into Ω_o, changes to its Fourier transform reflect this. Therefore, accurate measurements taken in *k*-space of a moving object must necessarily reconstruct to an image with some energy inside Ω_o.

If the measurements are noisy, the reconstruction throughout Γ is affected, with or without the presence of motion artifacts. There is no reason to expect that the mean noise power

per pixel differs significantly between Ω_i and Ω_o. Thus, while the relative energy outside the support is due to both noise and artifacts, only the portion of this due to artifacts will change between a reference image and a motion-corrupted image.

The estimation of DBE proceeds as follows:

1. Locate the background in the reference image using thresholding followed by morphological 'opening'. Form a binary mask that can be used to partition the image into the object and the background (Fig. 5.5).
2. Use this mask to locate an equivalent background region in the test image. This is achieved by shifting and rotating the mask in order to minimise the amount of energy in the located background.
3. Compute the total energy in the reference (T_{ref}) and test (T_{test}) images as well as the background energy for both images (B_{ref} and B_{test}).
4. The metric is then given by:

$$\mathrm{DBE} = \frac{B_{test}}{T_{test}} - \frac{B_{ref}}{T_{ref}} \tag{5.2}$$

Energy is defined as in Section 2.6, that is, the energy of an image (or signal) is equal to the integral of the signal squared over the region (or interval) of interest.

For Step 1, pixels with intensity below a threshold value are considered to be 'background'. The threshold found to be appropriate is 25 % of the mean pixel intensity. A morphological opening is then applied to remove isolated points erroneously classified as part of the object due to noise. Sample results for this are shown in Fig. 5.5. Experience shows that this simple thresholding technique is sufficiently robust for the application. Acceptable results have been achieved using a threshold of anywhere between 15 % and 35 % of the mean pixel intensity, suggesting that the choice of threshold is not critical.

Step 2 allows the reconstructed image under test to be translated or rotated with respect to the reference image. By searching for the mask position and orientation which minimises B_{test}, the value of the resulting metric best represents the degree to which the background is corrupted by artifacts. This is currently achieved using an exhaustive search of position and rotation angle to find the global minimum: not a very computationally efficient approach. A more efficient means of calculating the DBE metric is presented in Section 5.5.1.

Step 4 involves subtracting the proportion of energy in the background of the reference image from the proportion of energy in an equivalent region in the test image. Since measurement errors in MRI affect *k*-space measurements and image space noise level is relatively

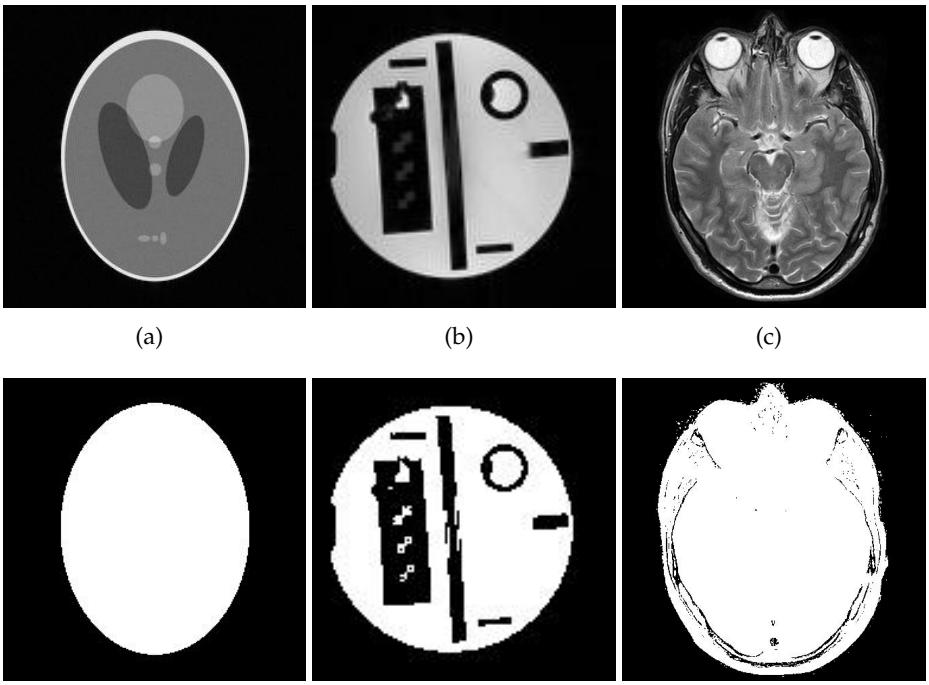

Figure 5.5 Three images and the binary masks representing their backgrounds, as found using the thresholding and opening technique described in the text. The segmentation does not need to be exact: minor changes make little difference to the final DBE metric.

independent of location, the contribution of noise energy to the ratio B_{test}/T_{test} is largely canceled by subtracting B_{ref}/T_{ref}. As a result, the DBE metric is very insensitive to the level of noise in the *k*-space measurements.

When applied to each test image in Fig. 5.1, DBE values are: (a) 3.2×10^{-6}, (b) 6.0×10^{-4}, (c) 1.2×10^{-2}, and (d) 2.6×10^{-2}, respectively. Values for images (a) and (b) are relatively close to zero, indicating that the images are essentially the same as the reference image. The DBE values for images (c) and (d) indicates major differences between them and the reference; this is the case for image (d) more so than image (c). These results are promising as they correspond well to human perception of the test images.

Having performed these basic tests, an experiment to further compare these three metrics was carried out.

5.5 Application to a motion corrupted sequence

A sequence of images corrupted by simulated motion is shown in Fig. 5.6. The uncorrupted reference image is that shown in Fig. 5.6(a). Each image in the sequence (b)–(h) is corrupted by a slightly greater amount of motion than the previous one. In images (a)–

(c) the increasing image corruption is so slight that it is not readily apparent to the eye, while in images (c)–(f) the ghosting becomes progressively more obvious. From (f)–(h) the ghosting continues to increases, but the change is less noticeable.

Motion has been simulated by modifying the phase of every third line of data in *k*-space. This is consistent with an acquisition method such as multiple-shot FSE, using three shots to fill *k*-space. The simulated motion corresponds to a horizontal shift in the object after acquisition of the second shot. The result is a modulation of *k*-space data resulting in ghosting in the phase-encode (vertical) direction.

The simulation of motion is such that the MSE metric can be estimated without image registration in this case. This is because the centre of *k*-space is acquired with the object in the same position in each test case. Also, note that this simulation maintains the same energy for each image because only *k*-space phase, not magnitude, is modified. Thus, *k*-space energy does not change between simulated data sets and Parseval's theorem ensures that this also applies to the image-space reconstructions.

Fig. 5.7 shows the performance of the three metrics presented here for the images in Fig. 5.6. Both MSE and DBE provide a good indication of the level of artifacts in the images shown. Furthermore, the similarity between the two is striking. The blur metric does not behave consistently with increasing artifact levels; this is the result of incorrect edge detection, as identified in Section 5.3.

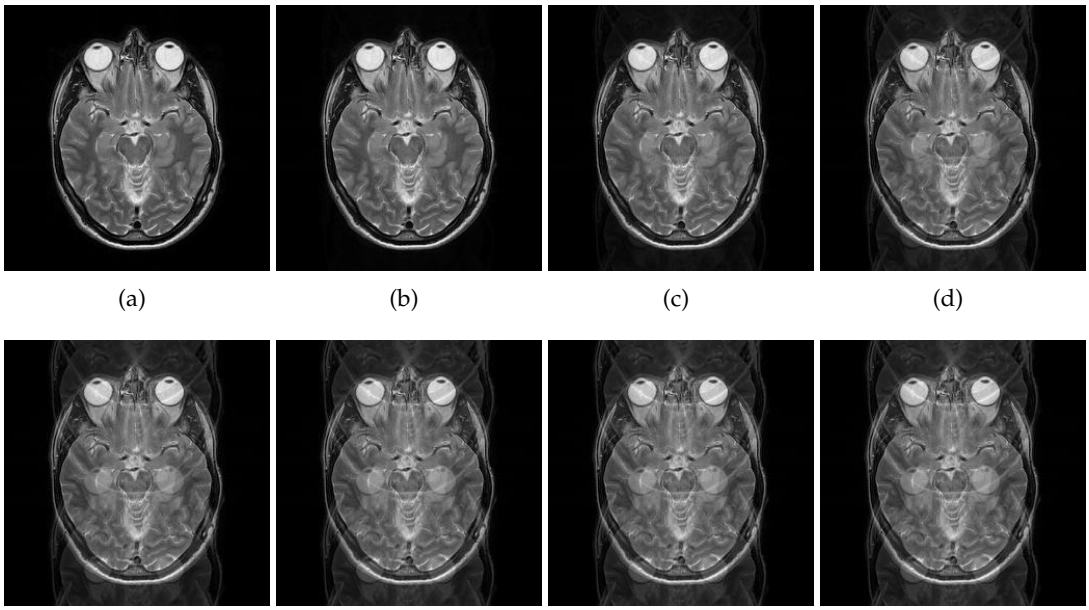

Figure 5.6 A sequence of motion corrupted images. The artifact metrics for these are plotted in Fig. 5.7.

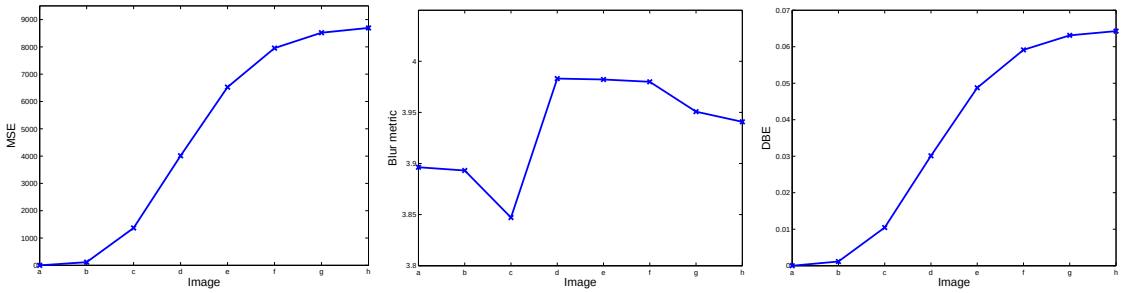

(a) (b) (c)

Figure 5.7 Artifact metrics for the images shown in Fig. 5.1: (a) MSE, (b) the blur metric and (c) DBE. Note the close similarity of the MSE and DBE metrics for this example.

Determining the DBE metric involves registering the mask with the test image. This is significantly easier than registering two images in order to obtain the MSE metric. A minor error in registration with MSE can lead to a grossly different metric value. A minor error in registration with DBE produces only a small change in the final result. This is illustrated in Fig. 5.8 in which a registration error of 1 pixel (horizontally) is deliberately introduced for image (d) in the original sequence. Registration of the background mask was disabled when calculating DBE values in this experiment. The MSE metric (Fig. 5.8(a)) is affected to a much greater degree than the DBE metric (Fig. 5.8(b)).

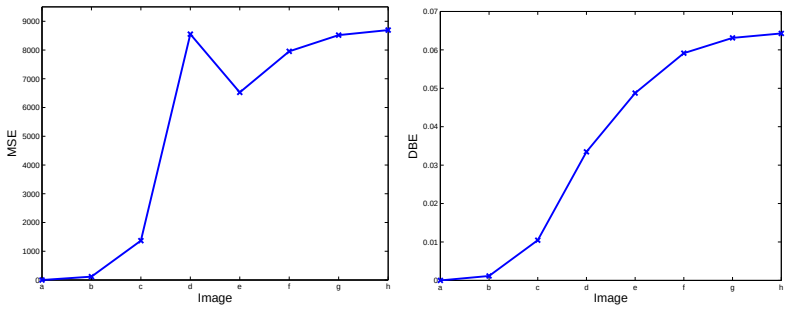

(a) (b)

Figure 5.8 The effect of a relatively minor registration error on (a) the MSE metric and (b) the DBE metric shown previously in Fig. 5.7(a) and (c). A fitting error of one pixel in the horizontal direction has been introduced for image (d) within the set shown in Fig. 5.6.

Another disadvantage of MSE is that it is affected by noise in the images. A metric is required that provides a measure of the severity of artifacts in an image, but is not sensitive to the level of noise inherent in the measurements. Both the MSE and blur metric measures are sensitive to the noise level, while DBE is not (this is apparent in an experiment shown in Section 7.4).

5.5.1 Extension to the DBE metric

The DBE metric requires a background mask to be fitted to the test image (a somewhat computationally expensive process). To alleviate this limitation an approximation is provided here which is useful if the metric is to be used in a situation where computational speed is important. The approximation is described as follows:

1. Locate the background in the reference image in the same way as described in Section 5.4.

2. Count the number of pixels, N_B, in the background of the reference image.

3. Rank the pixels of each image according to intensity.

4. Make the assumption that the smallest ranked N_B pixels in each image correspond to the background, and use those pixels to compute the values B_{ref}, B_{test}.

5. Compute the metric by Eq. (5.2).

The advantage of this approximation is computational speed. The relatively expensive registration of a mask is not required: the algorithm is already unaffected by shifts or rotations of the object within the field-of-view. The assumption that the N_B smallest-valued pixels will all be found in the background holds well for images with reasonably low artifact and noise levels. Fig. 5.9 shows a comparison of the original DBE metric for the sequence of images shown in Fig. 5.6 with this approximation. It is clear that qualitatively similar results are obtained with the simpler background definition algorithm.

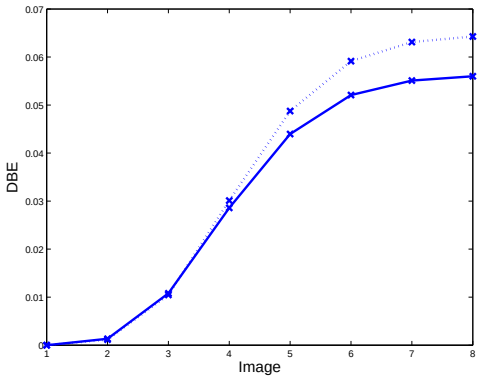

Figure 5.9 A comparison of the DBE metric described originally (dotted line) and its approximation as described in Section 5.5.1 (solid line) for the sequence of images shown in Fig. 5.6.

5.6 Discussion and conclusions

Three metrics for quantifying image artifacts have been compared: MSE, the blur metric, and the DBE metric.

MSE proved to be unsuitable for this purpose. It requires accurate image registration in order to produce a reliable result. This is difficult to achieve for motion-corrupted images. It is also sensitive to differing noise levels in the images.

The blur metric performed badly in the experiments shown. Nevertheless, the author believes that it has some potential for this application. It is interesting to analyse why and where it failed. Results in Fig. 5.4 show that extra edges are detected if significant ghosting is present. This suggests an alternative approach: seeking a metric that quantifies how well edges match between the reference and the test images. This measure could be quite similar to the human perception of image quality (humans identify edges well).

The DBE metric is found to perform the best in simulations. It has ideal properties for MRI applications involving artifacts: translation invariance, rotation invariance and a high level of sensitivity to artifacts with a low noise sensitivity. In Chapter 7, the DBE metric is shown to be useful in conjunction with the author's TRELLIS algorithm (for motion correction). It is used to investigate TRELLIS to automatically determine the noise level at which TRELLIS no longer performs satisfactorily. Without a metric such as DBE, this experiment would be more difficult to carry out.

A number of questions remain unanswered, however. It would be useful to investigate how different metrics correlate with diagnostic utility in an image. It would also be interesting to try using separate metrics to quantify different types of motion artifact. The DBE metric, for example, may be more sensitive to ghosting than to blurring in an image. Thus, a separate measure of blur might complement the DBE metric well.

Chapter 6

TRELLIS: A Motion Correction Algorithm

Although numerous motion-correction techniques have been developed, these all have their disadvantages. Navigator echoes and PROPELLER, for example, collect extra data to obtain motion information, leading to an increased acquisition time. Real-time tracking and gradient adjustment requires external hardware; this added complication perhaps explains why this method is not widely used. Post-processing techniques, although convenient, have had limited success so far.

This chapter presents a motion-correcting pulse sequence and reconstruction algorithm, termed TRELLIS [113]. This technique uses *all* collected data for *both* image reconstruction and motion detection; thus, it differs significantly to existing techniques.

This chapter describes the initial simulated version of TRELLIS; modifications associated with the implementation of TRELLIS on a scanner are discussed in subsequent chapters.

6.1 Introduction

The term 'TRELLIS' is an acronym for **T**ranslation and **R**otation **E**stimation using **L**inear **L**east-squares and **I**nterleaved **S**trips, and is so named because its sampling pattern resembles a trellis. This technique has some similarities to PROPELLER: it does not require extra hardware; it samples k-space more than once to obtain information about patient motion; it is capable of estimating translation (x- and y-directions) and rotation (in-plane only) parameters; and the final reconstruction requires some form of gridding. The data acquisition and image correction methods differ substantially, however, and TRELLIS may offer some

advantage because *k*-space is uniformly sampled instead of concentrating sampling in the centre of *k*-space as in PROPELLER. All acquired data is used for both motion detection and image reconstruction. Thus, extra time spent oversampling results in a useful SNR improvement across all spatial frequencies.

The description of TRELLIS is broken down into four consecutive steps:

1. **Data acquisition:** *k*-space is filled using orthogonal overlapping strips. Data from horizontal and vertical strips are stored in separate arrays denoted **H** and **V**, respectively.

2. **Rotation estimation and correction:** overlap between the horizontal and vertical strips in *k*-space magnitude data is used to estimate the rotation parameters of the object. Strips are then rotated in *k*-space to correct for this.

3. **Translation estimation and correction:** Translation parameters are estimated by using overlap between the horizontal and vertical strips in the *k*-space phase data. Corrupted data is then corrected in *k*-space by adjusting its phase.

4. **Image reconstruction:** all corrected *k*-space data is gridded onto a Cartesian coordinate system to allow application of the inverse Fourier transform. The final result is a motion-corrected image.

Each of the above steps is described in detail in the following sections.

6.2 Data acquisition

TRELLIS uses a unique *k*-space trajectory. Data is acquired using interleaved horizontal and vertical strips as shown in Fig. 6.1(a). In the example shown, the number of strips used to fill *k*-space, N_s, is 16. The acquired data is stored separately in two arrays: **H**, k-space data acquired using horizontal strips; and **V**, k-space data acquired using vertical strips.

The description of the practical implementation of this trajectory is deferred to Chapter 8. In the meantime, it is sufficient to state that each strip consists of a number of lines and the phase- and frequency-encode directions are selected so that the frequency-encode direction is always parallel to these (Fig. 6.1(b)). For now, the assumption is that each individual strip is acquired so rapidly that negligible motion occurs during the strip acquisition.

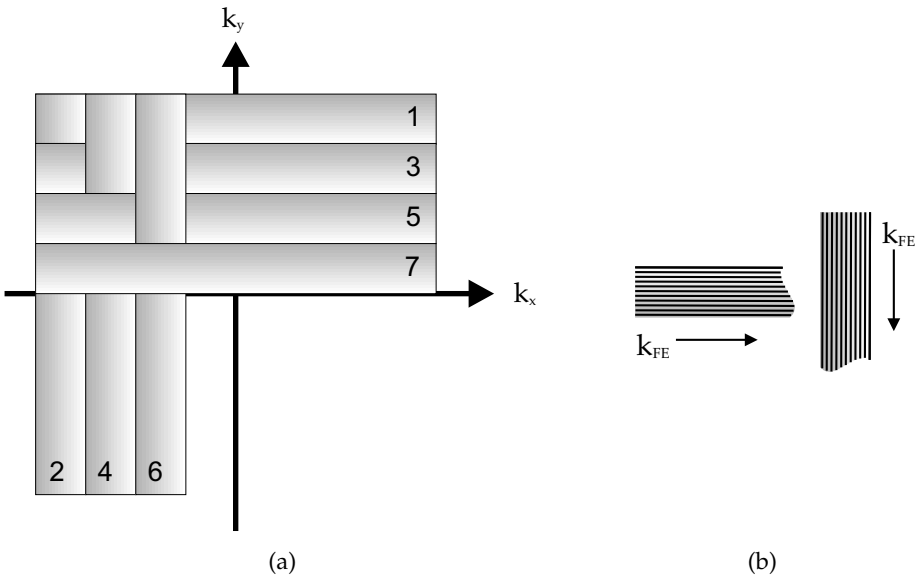

Figure 6.1 (a) The *k*-space trajectory used by TRELLIS. In this example, 16 strips are used to fill *k*-space ($N_s = 16$). The first 7 strips are shown; their numbers indicate the order of acquisition. (b) Each strip comprises a number of lines, with the frequency-encode direction always parallel to these.

6.3 Rotation estimation and correction

The next step after data acquisition is the estimation of rotation parameters. Referring back to Eq. (2.15) in Section 2.6, a rotation of the imaged object is equivalent to an equal rotation in *k*-space. Here, the goal is to determine the rotation of the object from *k*-space samples. This is achieved using *k*-space magnitude data: *k*-space phase information may have been corrupted by translational motion as described by Eq. (2.14). The rotation detection procedure is therefore decoupled from the translation estimation stage (Section 6.4) by using *k*-space magnitude to estimate rotation, whereas *k*-space phase is used to estimate translation. This section describes how rotation estimation is achieved [114].

6.3.1 Initial rotation estimation

Data is acquired as N_s strips of *k*-space, $N_s/2$ horizontal and $N_s/2$ vertical, where N_s is even. Each strip therefore overlaps $N_s/2$ other strips. If there is no motion while the data is acquired, the *k*-space data in each region of overlap between a pair of strips, one horizontal and the other vertical, should be identical except for the inevitable presence of noise. Strips are acquired in the order $1, 2, \ldots, N_s$. Consider two *k*-space strips (Fig. 6.2), a horizontal strip with odd integer index p and a vertical strip with even integer index q. Each strip is measured at a known time when the object is rotated by an unknown angle θ. The relative angle of rotation between the two strips is determined by comparing the magnitude values within the overlapping region, using complex interpolation to generate correspond-

ing points. Let θ_p be the angle that the strip p data is rotated from its nominal horizontal orientation and θ_q be the angle that the strip q data is rotated from its nominal vertical orientation. The relative angle of rotation is then $\theta_{pq} = (\theta_p - \theta_q)$, which has zero value if the strips are perpendicular. The area of overlap between two strips is henceforth referred to as a 'patch'. Note that rotations are made about the origin of *k*-space.

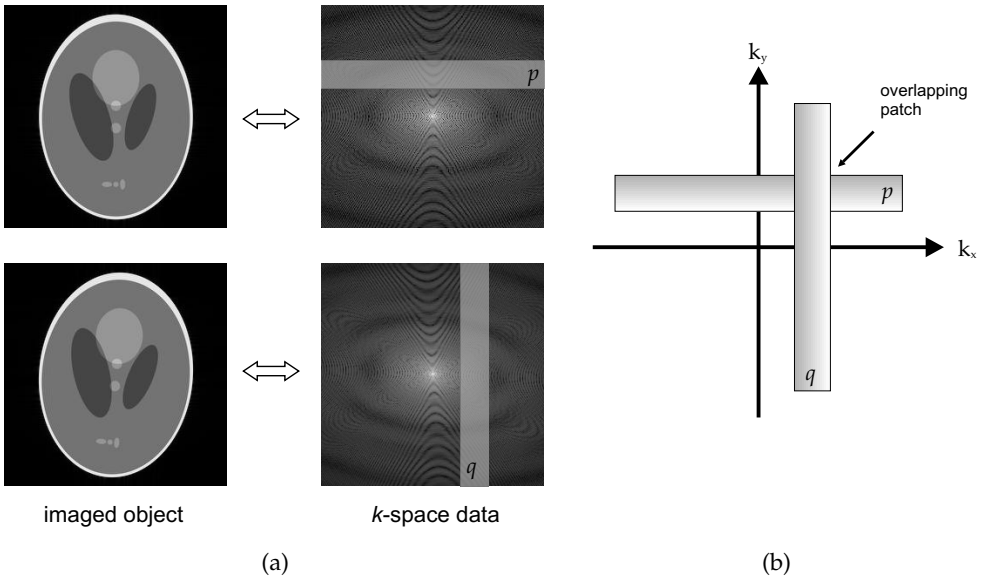

Figure 6.2 Each strip in *k*-space is acquired at a different time; thus, the imaged object may have moved between acquisition of the two strips (a). Any given horizontal strip, p, in *k*-space will overlap any given vertical strip, q. The overlapping patch of data between strips p and q (b) is used to determine the relative angle of rotation, θ_{pq}.

Rotation that has occurred between the measurement of two orthogonal strips is determined by rotating one strip relative to the other to achieve the largest correlation between the *k*-space magnitudes in the overlapping patch. In practice, the *k*-space data from each strip is first transformed into polar coordinates with respect to the origin of *k*-space using spline interpolation of the real and imaginary parts. This is computationally efficient since interpolation only needs to be performed once and testing individual rotation angles is reduced to a simple matrix shift. For each patch, the normalised mean square error (NMSE) between the strip magnitudes is computed for a range of relative angles, $-10^\circ \leq \theta_{pq} \leq +10^\circ$, in 0.1° increments. The NMSE metric is defined as

$$\text{NMSE} = \frac{\sum_{\text{patch}} \left[\, |F_p| - |F_q| \,\right]^2}{\sum_{\text{patch}} |F_p| \;\; \sum_{\text{patch}} |F_q|} \,, \tag{6.1}$$

where F_p and F_q are the *k*-space data values from the strips concerned. The angle for which NMSE is minimum is taken to be an initial estimate of θ_{pq} (Fig. 6.3). The magnitude-dependent normalisation in Eq. (6.1) prevents a bias when changing the angle θ_{pq} and

moving the position of the overlapping patch in relation to the centre of *k*-space (and hence changing the magnitude of the data within the patch).

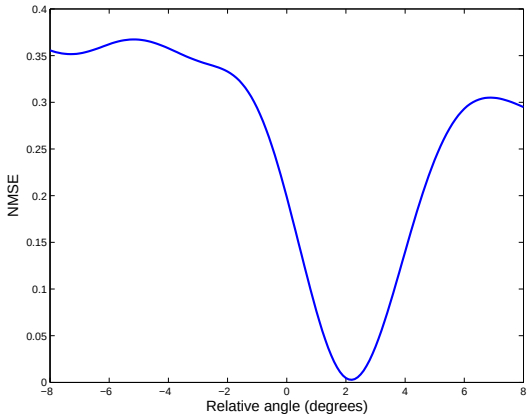

Figure 6.3 Correlation as a function of rotation angle for two overlapping strips, p and q, in *k*-space. The relative angle, θ_{pq}, between the two strips is 2.2° in this example.

The procedure described above is performed for all overlapping strips so that a value for θ_{pq} is obtained for all possible values of p and q. The goal is then to estimate the set of individual strip angles, $\{\theta_p\}$ and $\{\theta_q\}$.

A set of equations can then be written that links measured values for θ_{pq} to the individual strip angles $\{\theta_p\}$ and $\{\theta_q\}$. A weighted least squares estimate of $\{\theta_p\}$ and $\{\theta_q\}$ is made; the weight given to each equation is (minimum NMSE)$^{-1}$. This weighting scheme has been chosen to give more emphasis to those patches where the best match between the strip magnitudes has been found, as measured by a relatively low minimum value for NMSE.

As an example of the system to be solved, for $N_s = 16$ there are 8 horizontal and 8 vertical strips and 64 patches. There are therefore 64 linear equations in 15 unknowns (the orientation of the first strip acquired is arbitrarily set as zero). In general, however, the set of linear equations is

$$\mathbf{S}\,\mathbf{x} = \mathbf{r}\,, \tag{6.2}$$

where the elements of the $(N_s/2)^2 \times 1$ vector $\mathbf{r}$ consist of all relative rotation angles, θ_{pq}, estimated using the NMSE technique described above. The matrix $\mathbf{S}$ has dimensions $(N_s/2)^2 \times (N_s - 1)$. Each row in $\mathbf{S}$ contains two non-zero elements of value 1 and -1, positioned to represent the two strips p and q that correspond to the measured rotation angle in $\mathbf{r}$. The sign of these values reflects the definition of relative rotation mentioned earlier, that is, $\theta_{pq} = \theta_p - \theta_q$.

Eq. (6.2) is solved for the $(N_s-1)\times 1$ vector $\mathbf{x}$ in a least squares sense using the *lscov* function in MATLAB® and the weighting scheme described above. The angle of the reference strip (0°) is then inserted in the first position in $\mathbf{x}$, increasing the dimensions of $\mathbf{x}$ to $N_s \times 1$. Each value in $\mathbf{x}$ then gives the initial estimate of $\{\theta_p\}$ and $\{\theta_q\}$, that is,

$$x_j = \begin{cases} \theta_p & j,p = 1,3,5,\ldots,N_s-1 \\ \theta_q & j,q = 2,4,6,\ldots,N_s\,. \end{cases} \tag{6.3}$$

As a rotation by θ in image-space results in a rotation by θ in *k*-space, the result in Eq. (6.3) is applicable to either domain. In image-space, θ_p and θ_q represent the relative rotation angle of the imaged object at the time of acquisition of strip p or q. In *k*-space, θ_p and θ_q represent the angle by which data in individual strips p or q have been rotated about the centre of *k*-space. Although the first strip acquired has been used as the reference strip, this choice is arbitrary. Choosing a different reference equates to rotating all *k*-space data together around the *k*-space origin: the relative strip angles remain the same.

6.3.2 Pruning

In the absence of noise and other measurement errors, the estimated angles can be expected to be accurate enough for successful rotation correction. Indeed, the author's early work on TRELLIS demonstrated some success with the straightforward estimation described above [105, 115]. In practice, however, some of the strip angle estimates are found to be significantly in error. The inaccuracy of the initial angle estimates is particularly noticeable for strips lying outermost in *k*-space. Having estimated the individual strip angles as described, it is possible to recompute the *expected* angle difference, θ_{pq}, for each patch and compare this with the value derived from the NMSE minimum. The author postulates that small discrepancies from the expected angle differences are more likely to be observed in patches for which the NMSE minima are reliable because of a relatively good SNR, while larger discrepancies are more likely to be observed for NMSE minima which are unreliable because of a relatively poor SNR. The latter patches can therefore be 'pruned' from the estimation process, thereby improving the accuracy of the estimation. This technique is similar to a class of 'robust least-squares' approaches described in the literature [116].

The pruning is implemented as follows:

1. The discrepancies between the re-computed angle difference and the value derived from the NMSE minimum are determined for all patches not yet pruned.

2. The standard deviation σ_d of the distribution of discrepancies is computed.

3. Those patches for which the discrepancy in angle difference exceeds $2\sigma_d$ in magnitude are pruned.

4. The reduced set of equations is re-solved using the weighting (minimum NMSE)$^{-1}$ as described above.

Steps 1 to 4 are performed three times. The number of iterations has been determined empirically over a range of different values of N_s. As is shown in Chapter 7, the pruning process significantly improves the rotation estimation accuracy.

6.3.3 Rotation correction

Once rotation angles for all N_s strips have been estimated, each strip is corrected individually by rotating the coordinates of each data point relative to the coordinate system. For example, if strip p is found to have been rotated by θ_p from its nominal position, then the coordinate system is rotated by θ_p to match. Data is then gridded to the Cartesian coordinate system using 2-D spline interpolation of the real and imaginary parts. This is straightforward because data points within each individual strip are still on a rectangular grid; thus, interpolation is from one rectangular grid to another and the sampling density is constant. Each strip is not yet combined with other strips, but stored separately: individual strips are required for the translation estimation stage that follows.

The rotation correction of *k*-space strips is depicted in Fig. 6.4.

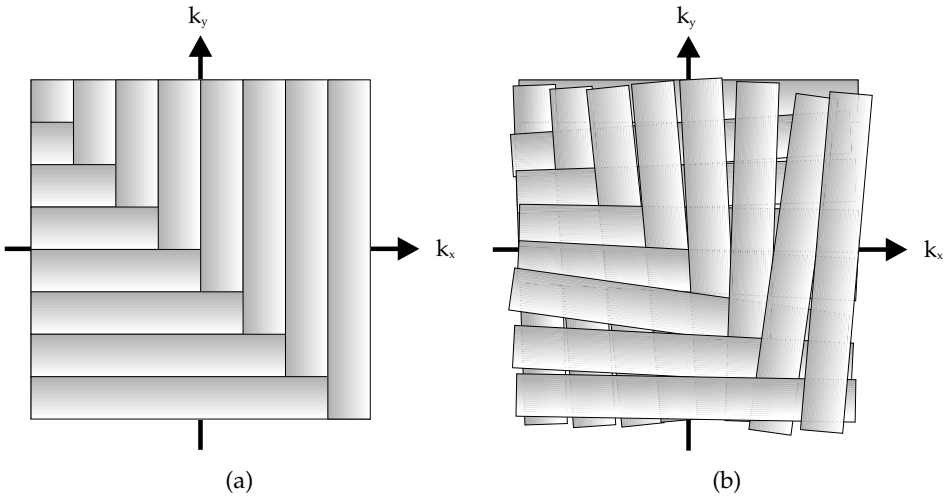

Figure 6.4 Rotation correction in *k*-space. A depiction of all acquired strips (a) before rotation correction and (b) after correction. The position of the object during acquisition of each strip in *k*-space defines the frame of reference for that strip. Thus, *k*-space strips have been rotated individually so that these frames of reference are all aligned.

6.4 Translation estimation and correction

Given rotation-corrected strips of *k*-space data, it is now possible to detect translational motion [117, 118, 119]. The goal is to identify the (x, y) position of the imaged object at the time each of the N_s strips of data in *k*-space were acquired. This position is relative to the position of the object when the first horizontal strip, with index $p = 1$, was acquired.

The procedure is similar to that used for rotation detection. To ultimately obtain the position of the object for each *k*-space strip, the relative shifts that have taken place between the sampling of each pair of strips are first calculated. The relative shift between a horizontal strip, p, overlapping a vertical strip, q, is denoted Δx_{pq} and Δy_{pq} in the x- and y-directions respectively.

6.4.1 Relative displacement

First, sections of data that overlap between strips p and q are identified using a simple binary mask. This is now possible as the rotation angle of each strip in *k*-space has been determined, and each rotation-corrected strip has been gridded to the same coordinate system (Fig. 6.5(a)). Although the overlapping patch between strips p and q is not necessarily square, the overlapping region is taken to be an $N_t \times N_t$ region which incorporates all of the overlap between the strips (Fig. 6.5(b)). The dimension N_t is always chosen to be even for computational convenience in the later stages of the algorithm. The phase difference between each repeated data point is computed giving the $N_t \times N_t$ matrix Φ_{pq} and a mask is formed to indicate which of the values in Φ_{pq} lie inside the patch.

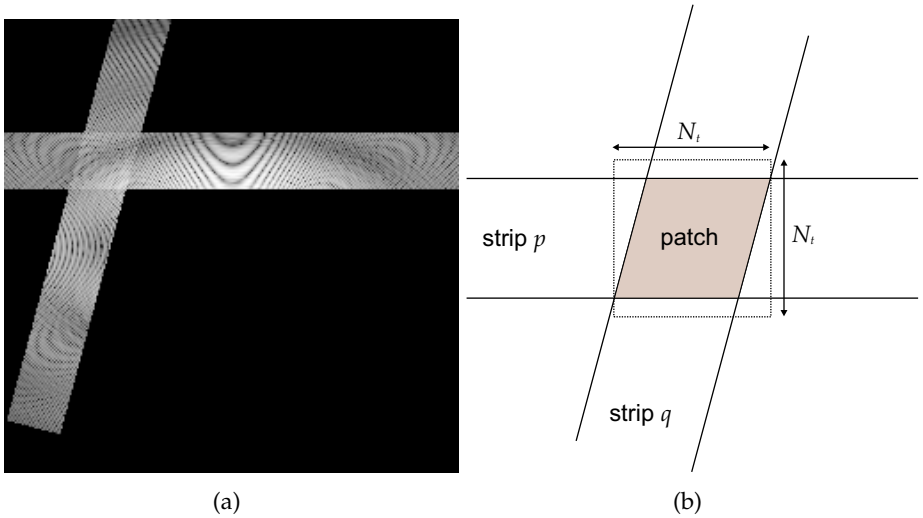

Figure 6.5 Forming Φ_{pq} from the overlap between strips: (a) two rotation-corrected overlapping strips of data in *k*-space; (b) dotted lines show the region used to form the $N_t \times N_t$ matrix Φ_{pq}.

In each patch each sample is acquired twice: once as part of a vertical strip and once as

part of a horizontal strip. As rotational motion has already been corrected for, if the object has not been translated between the acquisitions, both samples will be identical except for noise. If, however, the object has been translated by an amount $(\Delta x, \Delta y)$, the phase of the second sample will differ from the phase of the first sample by an amount proportional to $(\Delta x, \Delta y)$ and dependent on the location in *k*-space, (k_x, k_y). This is a direct result of the Fourier shift theorem (refer to Eq. (2.14)). The measured phase difference, Φ_{pq}, between matching points in strip p (horizontal) and strip q (vertical) within the region of overlap in *k*-space can therefore be expressed as

$$\Phi_{pq}(k_x, k_y) = [2\pi(k_x \Delta x_{pq} + k_y \Delta y_{pq}) + \text{ noise}] \bmod 2\pi\,, \qquad p, q \in 1, 2, \ldots, N_s \text{ for } p \text{ odd}, q \text{ even}\,, \tag{6.4}$$

where N_s is again assumed to be even.

Given the measured phase difference, Φ_{pq}, a means of estimating Δx_{pq} and Δy_{pq} is required. Although Δx_{pq} and Δy_{pq} correspond to the gradient of Φ_{pq} in the k_x and k_y directions respectively, calculating this gradient is problematic. Phase can only be measured modulo-2π as indicated in Eq. (6.4). Therefore the measured phase difference values must be unwrapped if the gradient is to be used to determine Δx_{pq} and Δy_{pq}. Two-dimensional phase unwrapping is not a trivial problem in the presence of noise [120].

6.4.2 The phase correlation method

To avoid the need for phase unwrapping the phase correlation method is applied, and the method is extended to allow sub-pixel accuracy. Phase correlation is a well-known approach when a measure of the translation of an object between images is required [121, 122, 123]. It relates phase differences between the Fourier transforms of the two images to the translation using the Fourier shift theorem (see Section 2.6).

First, the unity-magnitude complex-valued function $F(k_x, k_y) = e^{i\Phi_{pq}(k_x, k_y)}$ is formed for the *k*-space coordinate values, N_t^2 in number, which fall into the region of dimensions $N_t \times N_t$ around the patch. The magnitude of $F(k_x, k_y)$ is set to zero for any sample that corresponds to a location outside the original patch but within the $N_t \times N_t$ region. For ease of explanation of the phase correlation algorithm, $F(k_x, k_y)$ is expressed as $F(u, v)$, where $u, v = 0, 1, \ldots, N_t - 1$, are the indices of samples in the $N_t \times N_t$ *k*-space patch. The inverse DFT of $F(u, v)$ is given by

$$f(m,n) = \text{IDFT}(F(u,v)), \quad m,n = 0,1,...,N_t - 1.$$

Since the majority of values of $F(u,v)$ have unit magnitude and Φ_{pq} approximates to a ramp function, $f(m,n)$ approximates to a delta function, that is, a single peak. The spacing of the Cartesian samples in the *k*-space patch correspond to the same FOV as the whole image, but in $f(m,n)$ that FOV is spanned by only N_t samples in each coordinate direction. Thus, the location of the peak in the function $f(m,n)$, denoted (m_0, n_0), is only a coarse approximation to the precise location representing the shift $(\Delta x_{pq}, \Delta y_{pq})$.

To improve the estimate of $(\Delta x_{pq}, \Delta y_{pq})$, the $N_t \times N_t$ *k*-space patch could be padded by zeros out to a much larger space $\hat{N} \times \hat{N}$, where $\hat{N} = LN_t$, where L is an integer chosen according to the required accuracy sought for $(\Delta x_{pq}, \Delta y_{pq})$. The corresponding image-domain function would be an interpolated version of $f(m,n)$, denoted $f(m',n')$, where $m' = Lm$ and $n' = Ln$. For example, if L was chosen so that $\hat{N} \times \hat{N}$ had the dimensions of the original *k*-space data set, then the peak could be found to nearest-pixel accuracy. If L was larger still, sub-pixel accuracy would be possible. This would require taking the inverse DFT (implemented by the inverse FFT) of the function $F(u,v)$ and would thus become unworkable for very large values of L.

In practice, however, only a very small region of image-space needs to be evaluated to locate the maximum point in the interpolated function $f(m',n')$. Therefore, a more efficient direct calculation of the inverse DFT is performed by matrix multiplication as follows.

The general relationship between the interpolated function, $f(m',n')$, and the padded function, $F(u,v)$, is

$$f(m',n') = \sum_{u=0}^{\hat{N}-1} \sum_{v=0}^{\hat{N}-1} F(u,v) e^{i2\pi(um'+vn')/LN_t}, \quad m',n' = 0,1,\ldots,\hat{N}-1. \tag{6.5}$$

The summations on the right-hand-side of Eq. (6.5), however, are only required to include the N_t indices corresponding to the patch, while $f(m',n')$ is only required for a small subset of locations in the interpolated image space. The ranges required are

$$m' = (m_0 - 1)L, (m_0 - 1)L + 1, \ldots, m_0 L, \ldots (m_0 + 1)L$$
$$\text{and } n' = (n_0 - 1)L, (n_0 - 1)L + 1, \ldots, n_0 L, \ldots (n_0 + 1)L\,.$$

Eq. (6.5) can be expressed as

$$f(m', n') = \sum_{u=0}^{\hat{N}-1} e^{(i2\pi um'/LN_t)} \left(\sum_{v=0}^{\hat{N}-1} F(u, v) e^{(i2\pi vn'/LN_t)} \right) , \tag{6.6}$$

again noting that summations are limited only to indices around the peak previously located. Given Eq. (6.6), a matrix equation can be formed as

$$\mathbf{f} = \mathbf{Q}\,\mathbf{F}\,\mathbf{P}\,,$$

where $\mathbf{f}$ is a $(2L + 1) \times (2L + 1)$ square matrix of the interpolated values $f(m', n')$, $\mathbf{Q}$ is a $(2L + 1) \times N_t$ matrix of Fourier kernel values of form $e^{(i2\pi um'/LN_t)}$, $\mathbf{F}$ is an $N_t \times N_t$ matrix of values $F(u, v)$, and $\mathbf{P}$ is an $N_t \times (2L + 1)$ matrix of Fourier kernel values of the form $e^{(i2\pi vn'/LN_t)}$.

This implementation makes use of MATLAB's ability to perform high-speed matrix multiplications. The process is illustrated in Fig. 6.6. The peak in $f(m, n)$ is located and the interpolated function $f(m', n')$ is computed around that location. The process is repeated once more to obtain an accuracy of within 0.01 pixels; any greater accuracy becomes meaningless due to the effects of noise. The final location of the peak, when specified in terms of the original coordinate system, $f(m, n)$, is straightforwardly converted into the relative translation for the object, (Δx_{pq}, Δy_{pq}).

Other methods have been proposed to obtain sub-pixel accuracy using phase correlation. It is possible to fit a curve, such as *sinc* function [124], to the initial peaked function to enable interpolation between samples. The author also experimented with spline interpolation. However, the proposed method has proved to be more effective and less computationally demanding than other methods.

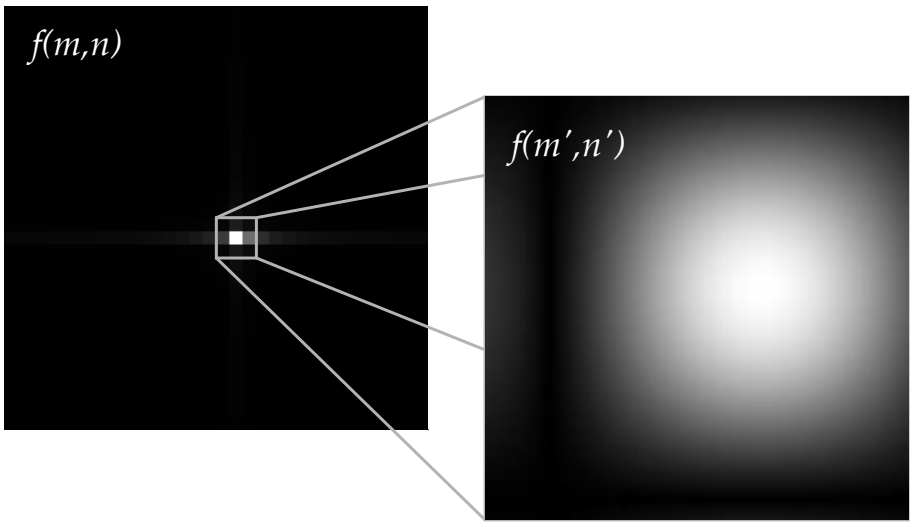

Figure 6.6 Plot of initial peak in $f(m, n)$ (left). For computational feasibility, the interpolated function $f(m', n')$ is then computed directly only in the area shown in the grey box. The result of this is shown on the right. The peak can be located to much greater precision in $f(m', n')$ than in $f(m, n)$.

6.4.3 Absolute displacement

Using the phase difference, Φ_{pq}, between overlapping data points in strips p and q, relative displacement values, Δx_{pq} and Δy_{pq}, between each pair of overlapping strips have now been estimated. The procedure which follows is almost identical to that used for rotation estimation as described in Section 6.3.1. Again, there are $N_s/2$ horizontal strips and $N_s/2$ vertical strips, so there are $(N_s/2)^2$ equations linking the positions of each pair of strips. If the position of the object at the time the first strip, $p = 1$, is measured is taken to be the reference position, there are $N_s - 1$ pairs of unknowns: the $N_s - 1$ shifts of the object in image-space as the sequence of strips is acquired. A system of linear equations linking relative displacements to absolute displacements is then formed and solved (as was done for rotation).

The displacement in the x- and y-directions is treated separately. Only the set of equations used to identify the set of absolute displacement values in the x-direction, $\{\Delta x_p\}$ and $\{\Delta x_q\}$, from Δx_{pq} are presented here: an identical system is used to find $\{\Delta y_p\}$ and $\{\Delta y_q\}$.

The form of the system of equations is the same as that used for rotation estimation, namely

$$\mathbf{S}\,\mathbf{x} = \mathbf{r}\,, \tag{6.7}$$

where the elements of the $(N_s/2)^2 \times 1$ vector $\mathbf{r}$ now consist of all relative displacement measurements, Δx_{pq}, estimated using the technique described above. The matrix $\mathbf{S}$ is identical

to before. Again, it has dimensions $(N_s/2)^2 \times (N_s - 1)$, and again each row in **S** contains two non-zero elements of value 1 and -1, positioned to represent the two strips p and q that now correspond to the measured displacement in **r**. The sign of these values now reflects the definition of relative translation, that is, $\Delta x_{pq} = \Delta x_p - \Delta x_q$.

As was the case for Eq. (6.2), Eq. (6.7) is solved for the $(N_s - 1) \times 1$ vector **x** in a least squares sense using MATLAB's *lscov* function. After inserting the x-position of the reference strip (0 pixels) in the first position in **x** (increasing the dimensions of **x** to $N_s \times 1$), this produces an estimate of the x-position of the imaged object at the point in time when each strip was acquired, that is,

$$x_j = \begin{cases} \Delta x_p & j, p = 1, 3, 5, \ldots, N_s - 1 \\ \Delta x_q & j, q = 2, 4, 6, \ldots, N_s \end{cases} \tag{6.8}$$

Weighting and pruning schemes – as described for rotation estimation – have not been implemented for translation estimation in TRELLIS. The weighting function would have to differ, as the NMSE metric is used for rotation estimation but is not used here. There is no obvious replacement for the weighting function in translation estimation, although perhaps a measure relating to the relative magnitude of the peak generated in the phase correlation stage could be used.

A pruning scheme similar to that used for rotation estimation would presumably improve results if applied to translation estimation. Such a scheme was not implemented, however, as the translation estimation algorithm proved to be robust. A simpler system for identifying translation estimates that are in error is described later in Section 7.4 where results obtained from data with poor SNR are evaluated.

6.4.4 Translation correction

The translation detection algorithm gives the displacement of the imaged object at the sampling time of each strip in *k*-space. Given this, the phase of each data point in each *k*-space strip is adjusted. This is equivalent to shifting the object back to the reference position for each strip. It can also be thought of as making all *k*-space phase data consistent. The exact phase added to each point (k_x, k_y) in a strip p or q in *k*-space is

$$\Phi_a(k_x, k_y) = 2\pi(k_x \Delta x + k_y \Delta y)$$

where $\Delta x, \Delta y$ gives the estimated translation of the imaged object at the time the data in the strip in question was acquired.

6.5 Image reconstruction

Once all data has been corrected for the effects of rotational and translational motion, a complete *k*-space data set is formed so that a final image can be reconstructed.

Data values obtained from different strips gridded to the same *k*-space coordinate are averaged. During the rotation correction stage, however, 'holes' may have appeared in *k*-space data where no sampling occurred. To some extent these can be corrected using the Hermitian symmetry property of *k*-space. Fig. 6.7 demonstrates this process. In some cases a hole may exist in both sides of *k*-space meaning this 'Hermitian filling' is not possible. In this case, zeros are substituted in the place of missing data.

Knowledge of the location of the centre of *k*-space is required to correct for missing data in this way. For simulated data, this does not pose a problem: analytical *k*-space values have been calculated with a known centre. In the case of data obtained from a scanner, however, *k*-space must be centred after data is acquired. This process is described in Section 8.2.1.

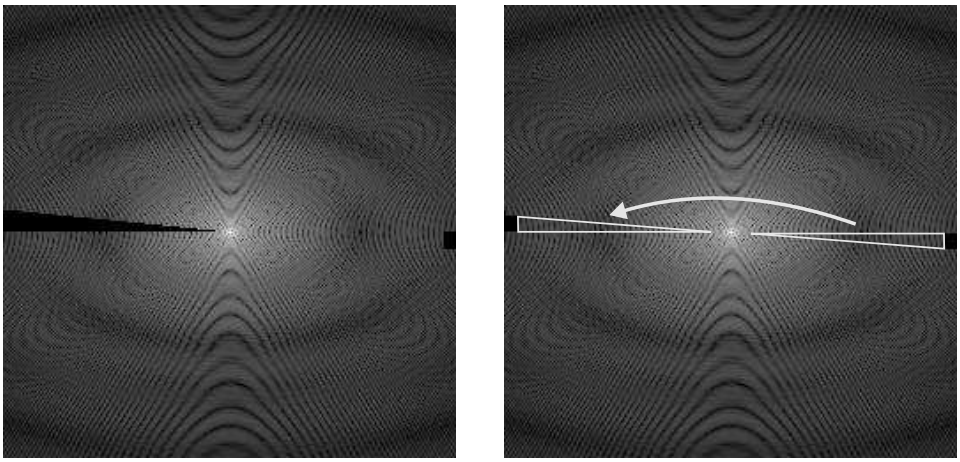

Figure 6.7 Filling 'holes' in *k*-space using the Hermitian symmetry property of *k*-space. The original version of *k*-space is shown on the left. On the right, holes have been filled using conjugate transpose data: if this is also missing, then zeros are used in place of measured data.

The author acknowledges that this means of replacing missing *k*-space data is not a particularly sophisticated approach. The implementation of other methods, such as reported by Pipe [125, 126] or Gabr et al. [127], may improve results.

Once a complete *k*-space data set has been formed, the inverse discrete Fourier transform is applied to produce the final motion-corrected image.

Chapter 7

TRELLIS: Simulations

This chapter presents the results of simulations performed to test the TRELLIS algorithm. One benefit of simulations is that motion is known exactly, enabling the performance of TRELLIS to be accurately quantified. It is also possible to test the robustness of the algorithm under a range of noise levels. Such simulations, while obviously overshadowed by clinical results, are therefore an important indicator of performance. These simulation results led to several proposed changes to aspects of the TRELLIS algorithm.

The results shown here were obtained using motion simulations generated using the analytical Shepp-Logan phantom described in Chapter 4. The motion simulated is exactly in plane and exactly rigid-body in nature. Simulations ignore effects such as T_2 signal decay and hardware imperfections such as field inhomogeneities. Furthermore, motion is assumed to occur only between the acquisition of each TRELLIS strip and not within strips.

7.1 Rotation estimation and correction

Simulations testing the rotation estimation and correction stage of TRELLIS were carried out. Translation estimation and correction was disabled for this experiment. Simulated motion involving rotation only is possible given knowledge of the exact centre of the object and the FOV. The simulated motion was an arbitrary sequence of small rotations resulting the variation in angular position over time shown in Fig. 7.1(a).

The rotation sequence was generated using a 'random walk', where the change in angle of the phantom between each strip acquisition was determined by a pseudo-random number generator with angle changes uniformly distributed over an interval of $[-5°, +5°]$. This limits the rotation that can take place between consecutive strips.

The rotation angles generated were specified to double precision to minimise the probability of them coinciding exactly with the rotation angles tested by TRELLIS, which uses an angular search increment of 0.1°. The maximum range of rotation is 9.88°. The same simulation was repeated using a motion sequence with 25 % of the rotation magnitude used initially, giving a maximum rotation range of 1.77° (Fig. 7.1(b)).

The number of strips used for both simulations, N_s, was 16 and the image resolution was 256×256 pixels. These parameters result in 8 strips in both **H** and **V** with $N_{etl} = 32$. Image reconstructions were performed for the simulations, with and without motion correction.

The mean difference between simulated and detected angles was 0.02° (standard deviation, $\sigma = 0.03°$) for both Fig. 7.1(a) and Fig. 7.1(b). These errors are smaller than the 0.1° angular search increment used for rotation detection. This is expected: the 8 strips in **H** overlap the 8 strips in **V** and result in 64 overlapping patches and 64 estimates of relative strip angles. Thus, the system of equations solved for the 16 strip angles is overdetermined and the least squares solution produces a more accurate estimate that obtained by each individual angle estimate alone.

Motion-corrupted images are shown in Fig. 7.1(c) and (d) and motion corrected versions of these are shown in Fig. 7.1(e) and (f), respectively. The image shown in (c) is visually more blurred than the image shown in (d) as expected due to the four-fold difference in the magnitude of simulated rotation. This visual assessment is supported by DBE values: 3.3×10^{-3} for the image in (c) and 5.2×10^{-4} for the image in (d). After correction (Fig. 7.1 (e) and (f)), artifacts are not visible to the eye, and the DBE values are reduced to 4.1×10^{-4} and 1.5×10^{-5}, respectively. DBE values were calculated using the simplified version of the metric described in Section 5.5.1 and using a reference image free of artifacts.

The results for a second set of simulations are shown in Fig. 7.2. This simulation set was identical to that described above, except for the addition of complex white Gaussian noise, giving a SNR of 25 dB. Noise was added in *k*-space as described in Section 4.1.1. Again, good agreement between simulated and estimated rotation angles is obtained with a mean difference of 0.064° ($\sigma = 0.05°$) in Fig. 7.2(a) and 0.048° ($\sigma = 0.05°$) in Fig. 7.2(b).

Images in Fig. 7.2(c)–(f) demonstrate the same effects as those in Fig. 7.1 discussed above, namely a reduction in image artifacts and the DBE values after motion correction. Values are 3.3×10^{-3} for the image in Fig. 7.2(c) reducing to 1.7×10^{-4} in (e) and 5.1×10^{-4} for the image in Fig. 7.2(d) reducing to -2.2×10^{-4}. The negative DBE value is caused by near-perfect rotation correction and a slight noise reduction in the image (compared to the reference) due to the simulated rotation resulting in some outer parts of *k*-space (with poor SNR) being left unsampled. This discrepancy could be corrected using a reference image with the same *k*-space sampling pattern as the test image.

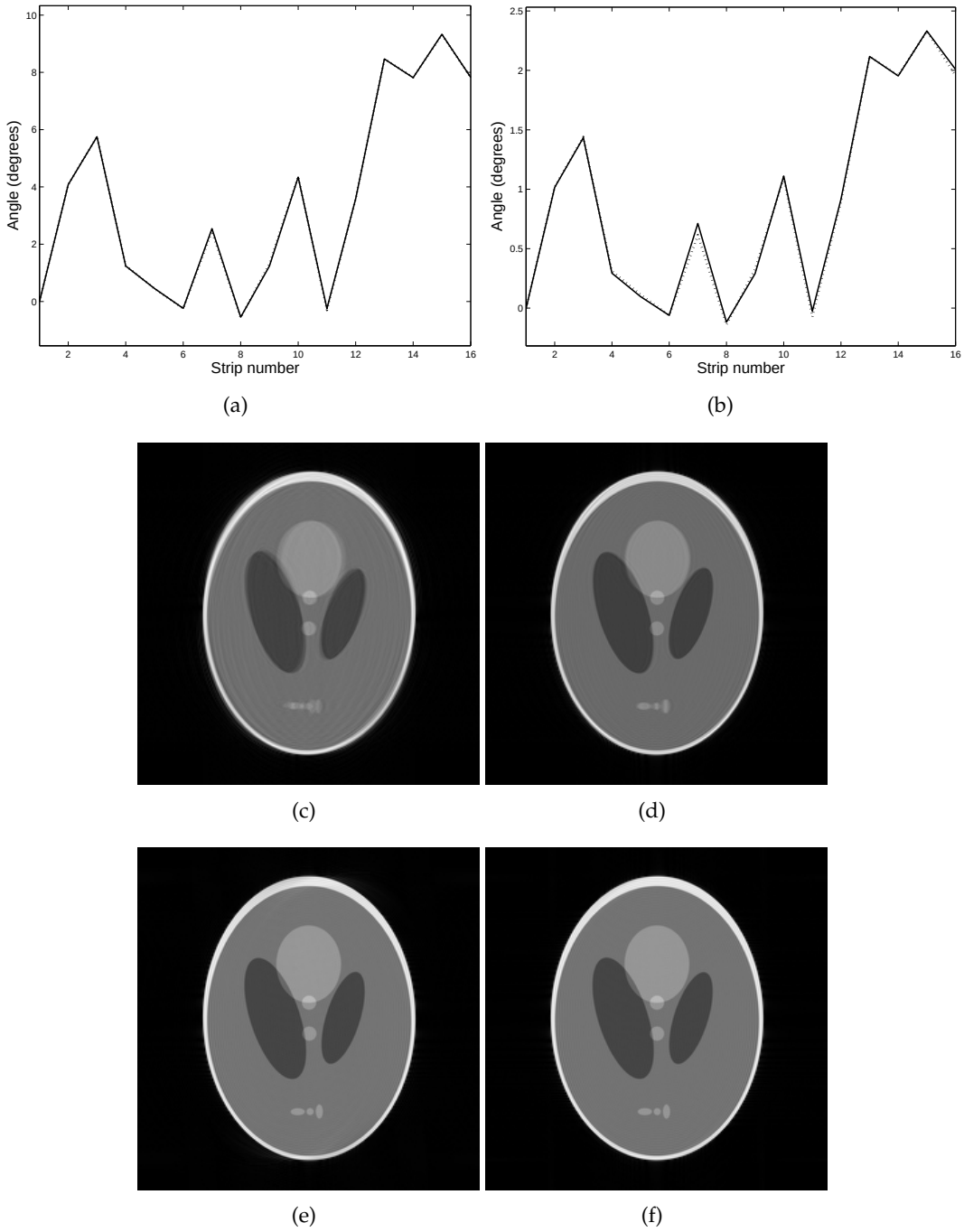

Figure 7.1 Simulation results for TRELLIS data acquired with no added noise during rigid-body rotation. The dotted line in (a) and (b) shows the simulated rotation of the phantom, while the solid line shows rotation estimated by TRELLIS. Reconstructed images are shown without motion correction, (c) and (d), and with motion correction, (e) and (f). Reconstructions in (c) and (e) correspond to the motion shown in (a), while (d) and (f) correspond to the lesser magnitude motion in (b).

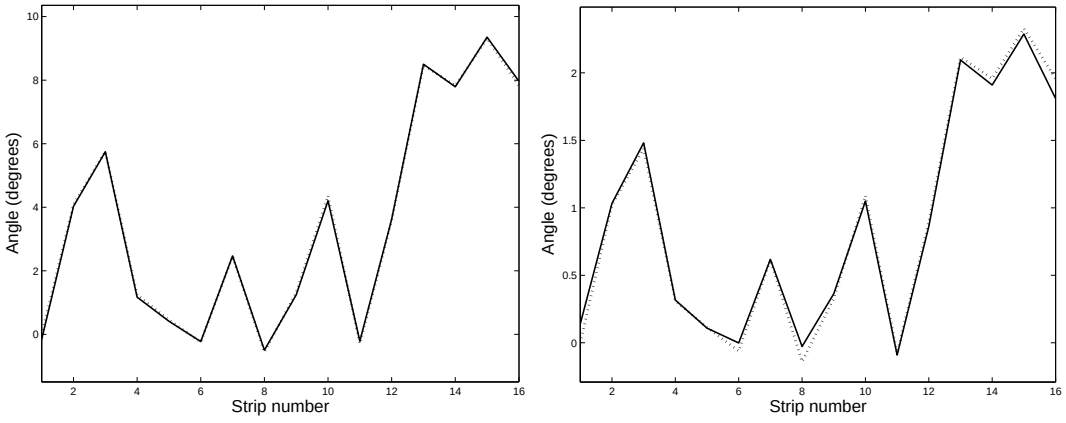

(a) (b)

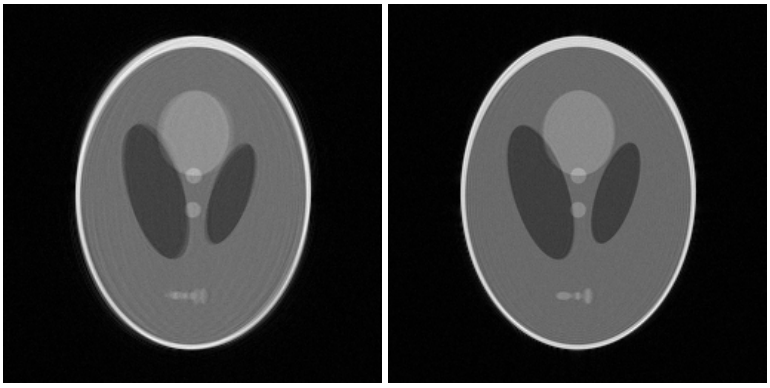

(c) (d)

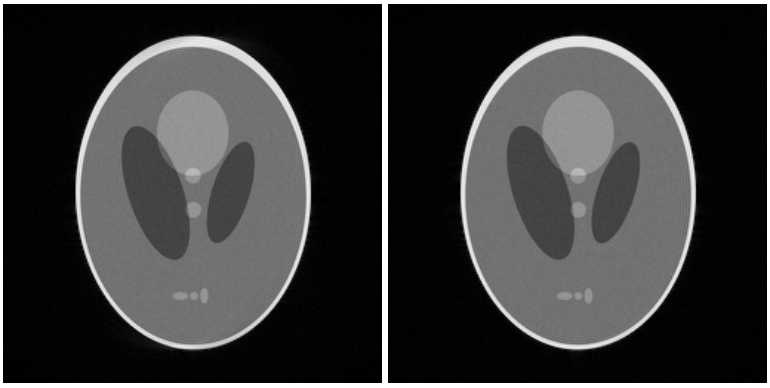

(e) (f)

Figure 7.2 The effect of noise (SNR = 25 dB for both **H** and **V**) on the simulations shown in Fig. 7.1. The simulated rotation of the phantom is shown by the dotted line in (a) and (b), with rotation estimated by TRELLIS shown by the solid line. The resulting images are shown without motion correction in (c) and (d), and with motion correction in (e) and (f). Although the error in detection of strip angles has doubled due to the addition of noise, the mean rotation estimation accuracy remains better than 0.1°.

7.2 Translation estimation and correction

In the previous section, the rotation estimation stage of TRELLIS was tested independently of translational motion. Here, simulation results testing the translation estimation and correction aspect of TRELLIS are presented. Rotation estimation and correction was disabled for this experiment. The simulated motion was again an arbitrary sequence, as shown in Fig. 7.3(a), generated using a 'random walk' approach. The maximum allowed change in position of the object between consecutive strips was 5 pixels in the x-direction and 3 pixels in the y-direction. The full range of translation in the simulation was 11.75 pixels in the x-direction and 6.96 pixels in the y-direction. The same motion sequence was repeated in a second simulation using motion with 25 % of the magnitude (shown in Fig. 7.3(b)), as was done for the rotation estimation simulation.

The same parameters as in the previous section were used, namely, $N_s = 16$, resolution = 256×256 pixels and $N_{etl} = 32$. Good agreement between simulated and detected translational motion was obtained. The mean difference between simulated and detected angles was less than $1{\times}10^{-3}$ pixels for both simulations and in both directions.

Reconstructed images are shown in Fig. 7.3(c)–(f). The uncorrected images corrupted by translational motion exhibit more artifacts than those corrupted by rotation. This visual comparison is in agreement with DBE values: $9.3{\times}10^{-3}$ and $1.4{\times}10^{-3}$ for images corrupted by translational motion compared to $3.3{\times}10^{-3}$ and $5.2{\times}10^{-4}$ for the equivalent rotation corrupted images shown earlier. This difference should be expected: the Shepp-Logan phantom has some degree of circular symmetry; thus, a rotation causes smaller discontinuities in the *k*-space data than a translation. DBE values for the corrected images, (e) and (f), are close to zero, indicating near-perfect motion correction in this case.

The results for a second set of simulations is given in Fig. 7.4. Simulation parameters used were identical to the first translation simulation, except for the addition of complex white Gaussian noise to the *k*-space data, giving a SNR of 25 dB. Again, good agreement between simulated and estimated motion is obtained. The mean difference between the two curves in Fig. 7.4(a) is 0.029 pixels in the x-direction ($\sigma = 0.03$ pixels) and 0.019 pixels in the y-direction ($\sigma = 0.01$ pixels). For Fig. 7.4(b), these figures are 0.023 pixels ($\sigma = 0.02$ pixels) and 0.027 pixels ($\sigma = 0.03$ pixels) in the x- and y-directions respectively.

DBE values reduced from $9.3{\times}10^{-3}$ to $1.8{\times}10^{-5}$ for the images in Fig. 7.4(c) and (e) respectively, and from $1.4{\times}10^{-3}$ to $4.1{\times}10^{-6}$ for the images in Fig. 7.4(d) and (f). As seen in these results and those shown earlier, any DBE value below about $1{\times}10^{-4}$ corresponds to an image with no visually-apparent motion artifacts.

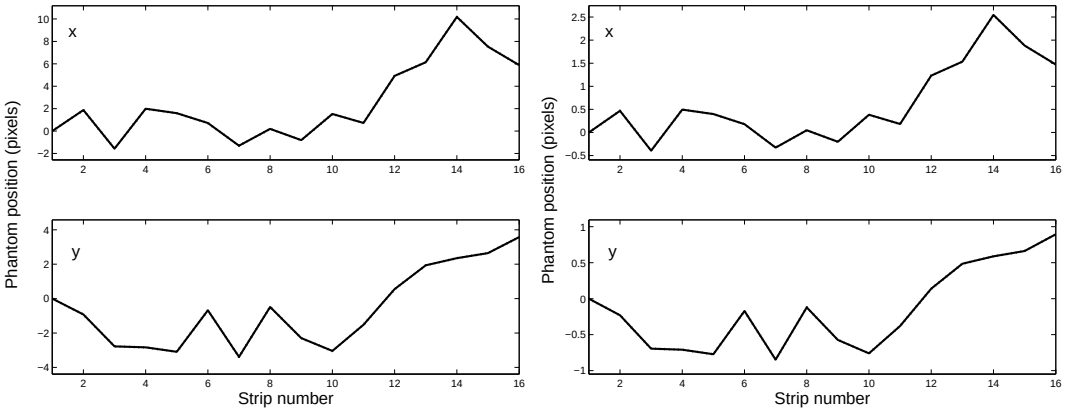

(a) (b)

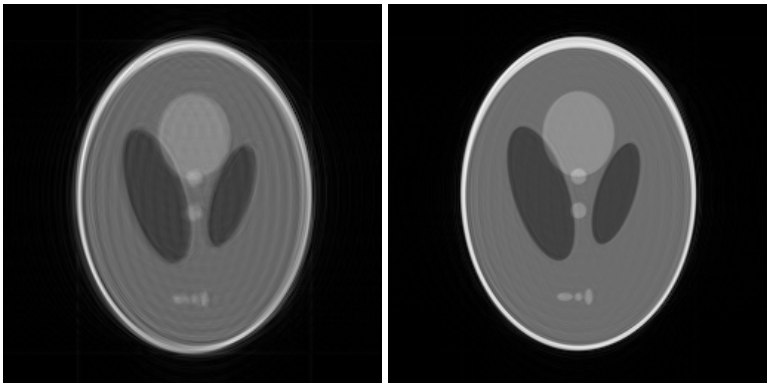

(c) (d)

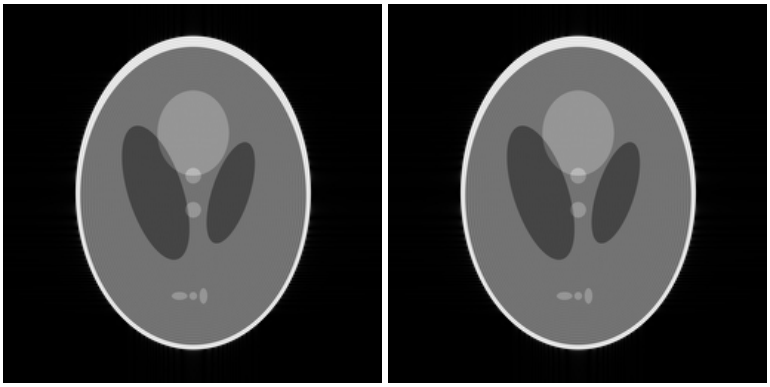

(e) (f)

Figure 7.3 Simulation results for TRELLIS acquired during rigid-body translation. The simulated motion of the phantom is shown by the dotted line in (a) and (b), with motion estimated by TRELLIS shown by the solid line. Reconstructions are shown without motion correction in (c) and (d), and with motion correction (e) and (f). This simulation does not include the effects of noise: estimated motion is almost identical to simulated motion. Reconstructions in (c) and (e) correspond to the translation shown in (a), while (d) and (f) correspond to the lesser translation in (b).

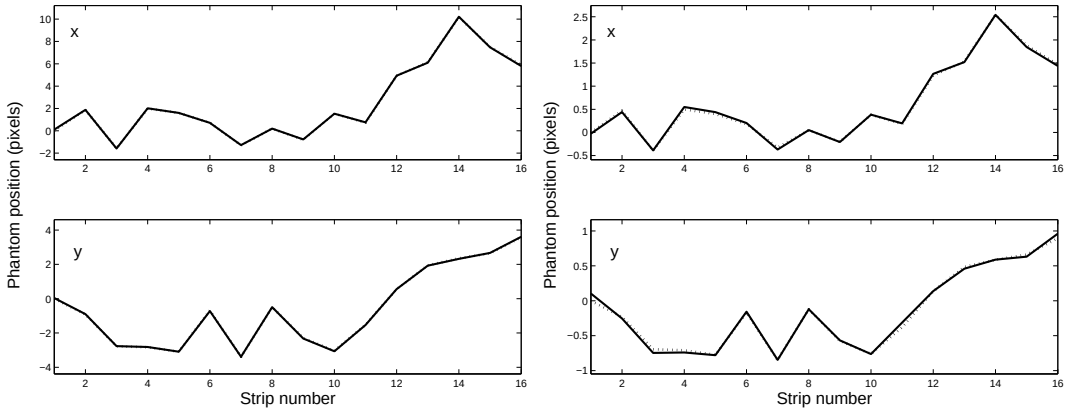

Figure 7.4 The effect of noise (SNR = 25 dB) on the simulation shown in Fig. 7.3. The simulated motion of the phantom is shown by the dotted line in (a) and (b), with motion estimated by TRELLIS shown by the solid line. The resulting images are shown without motion correction in (c) and (d), and with motion correction (e) and (f), respectively.

7.3 Combined rotation and translation

The effectiveness of both the rotational and the translation motion estimation stages of the TRELLIS algorithm have been demonstrated independently; now they are tested together.

It is reasonable to expect that TRELLIS rotation estimation should function as well in this experiment as it did in the experiments reported in Section 7.1. The addition of simulated translational motion affects only *k*-space phase; *k*-space magnitude is used for rotation estimation while phase is ignored.

Translation estimation is likely, however, to be adversely affected by rotational motion. It is hypothesised that small errors in the rotation estimation will propagate through to the translation estimation stage. For example, if two strips, p and q, are misaligned (relative to each other) by some angle, θ_e, after rotation correction, this will result in an offset, $(\Delta x_e, \Delta y_e)$, between points from p and q that are supposedly exactly aligned. This offset will result in errors in the phase patch Φ_{pq} which, in turn, may lead to errors in the location of the delta function found using the phase correlation method described in Section 6.4.2.

Simulation results are shown in Fig. 7.5. The motion simulated was combined rigid-body rotation and rigid-body translation using the same parameters as used previously to facilitate easy comparison between the experiments. The only difference is noise: the SNR remains at 25 dB, but noise values have been regenerated.

Error values are 0.034° ($\sigma = 0.03^\circ$) for estimated rotation, 0.047 pixels ($\sigma = 0.05$ pixels) for estimated translation in the x-direction, and 0.045 pixels in the y-direction ($\sigma = 0.04$ pixels). These results are as expected: rotation error is similar to that obtained for the test involving purely rotational motion; translation estimation error is slightly higher than that found when translation alone was simulated.

Overlapping patches between strips are visible in the uncorrected *k*-space magnitude data shown in Fig. 7.5(c). This is caused by discontinuities due to rotation errors and signal cancellation caused by phase errors due to translational motion. After TRELLIS motion correction, the resulting *k*-space magnitude data, shown in Fig. 7.5(d), no longer exhibits these errors. Note, however, that 'holes' appear in the *k*-space data at the top-right and bottom-left of (d). These are areas where *k*-space data values were not acquired due to inconsistent *k*-space sampling caused by rigid-body motion. Filling has not been possible in these instances using the Hermitian properties of *k*-space, as matching data is also missing.

Uncorrected and corrected images are shown in Fig. 7.5(e) and (f), respectively. The visual improvement in image quality is consistent with DBE values of 9.5×10^{-3} for the image in (e) and 2.1×10^{-4} for the image in (f).

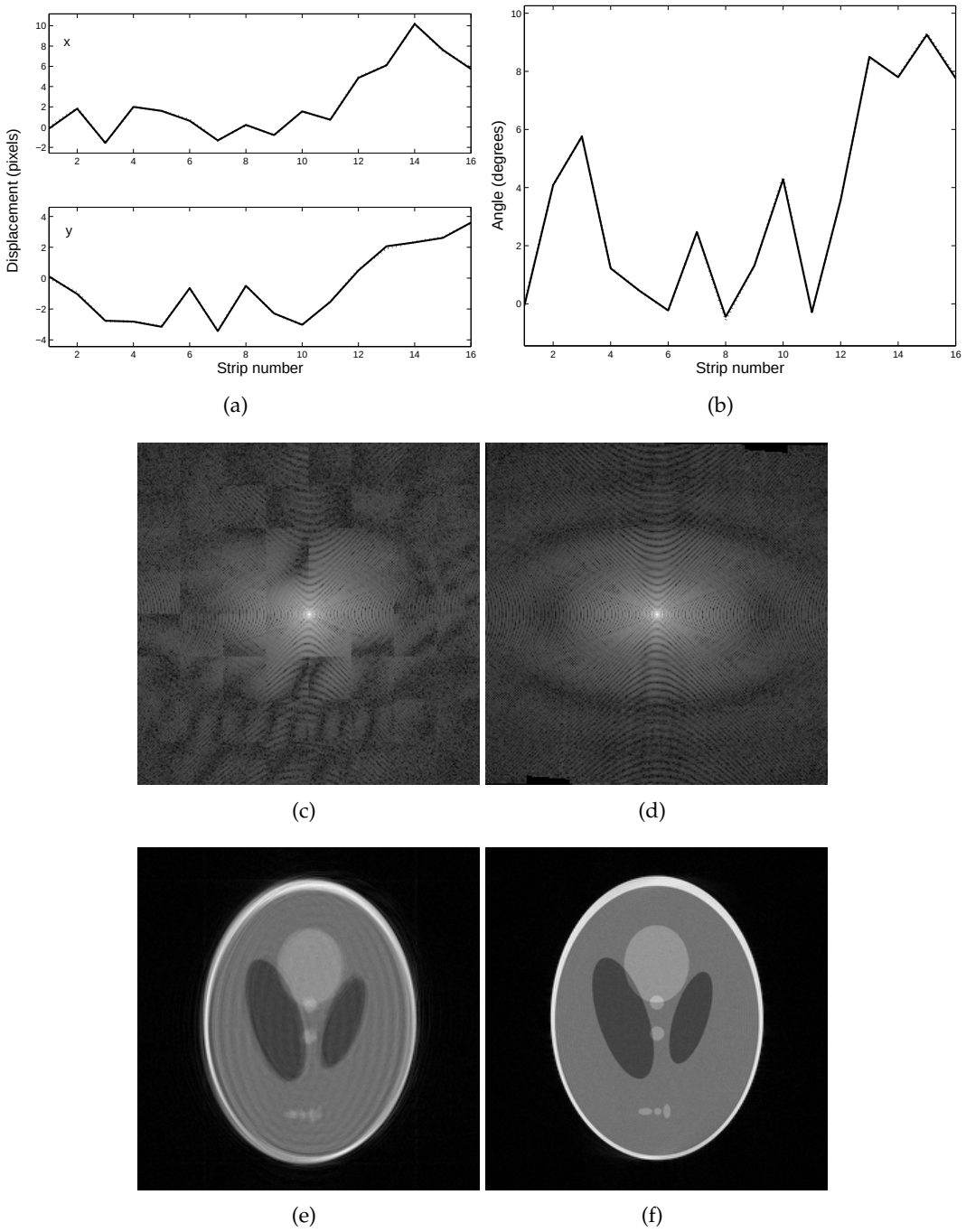

Figure 7.5 A simulation involving both translation and rotation with parameters shown by the dotted lines in (a) and (b). The **H** and **V** SNR was 25 dB. Estimated motion is shown by the solid line and follows simulated motion closely. Uncorrected k-space magnitude and image-space data is shown in (c) and (e), respectively. Corrected versions of k-space magnitude and image-space are shown in (d) and (f).

7.4 Noise performance

Simulations presented so far have used an SNR of either ∞ (no noise) or 25 dB. Results have indicated that the algorithm performs well at these noise levels. Nevertheless, at some point TRELLIS will cease to function correctly as the SNR decreases.

It is obviously important that the estimated motion values are accurate; otherwise, attempted motion correction will not improve the overall image quality and may instead make it worse. This can be seen in Fig. 7.6. In this case motion corruption has been simulated using the motion parameters described earlier, but with an SNR of 14 dB. Rather than correcting the image, TRELLIS has introduced further artifacts.

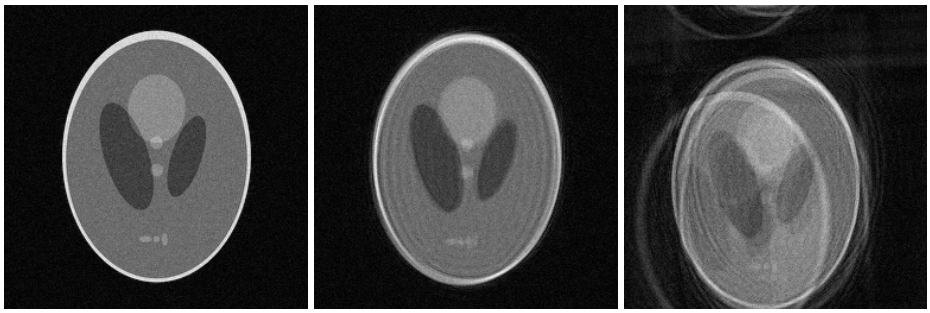

(a) (b) (c)

Figure 7.6 The Shepp-Logan phantom reconstructed from TRELLIS data with an SNR of 14 dB in **H** and **V**: (a) no motion, (b) uncorrected motion, and (c) corrected motion. Failure of the correction algorithm under noisy conditions has led to a reconstructed image with increased artifacts.

It is surmised that there is a 'noise threshold', above which TRELLIS motion correction no longer produces an improvement in image quality. The basis for this assumption is that as noise increases, errors in rotation and translation estimation will also increase. This will lead to a reconstructed image that contains motion artifacts. At some point, these artifacts will become worse than those in the original image.

An experiment was performed to identify the noise threshold and to determine the limiting factor in the TRELLIS algorithm that leads to a failure to correct for motion. The same motion parameters as used previously, and shown in Fig. 7.5(a) and (b), were used. SNR was varied from 40 dB to 14 dB. The simplified version of the DBE metric was used to quantify image artifacts.

Results are graphed in Fig. 7.7. The dashed line shows the DBE values for uncorrected images. The DBE metric is not significantly affected by noise levels, so this line is nearly horizontal. The solid line shows the DBE values for the motion-corrected images. Initially the DBE value is significantly lower than for uncorrected images, indicating that image quality is higher. As noise increases, however, the DBE values increase and eventually

exceed those calculated for uncorrected images.

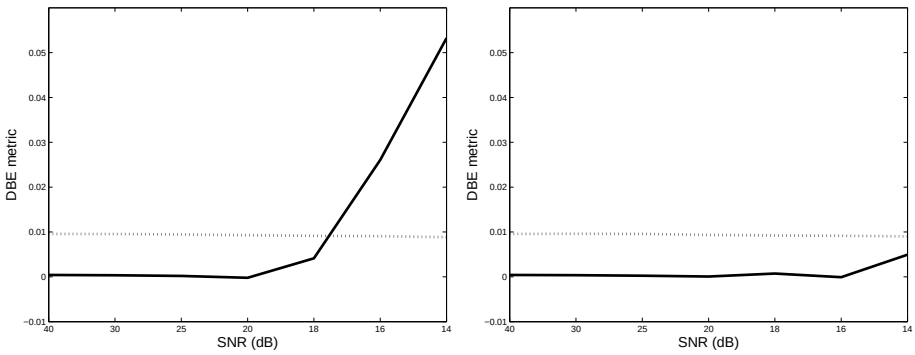

(a) (b)

Figure 7.7 The effect of *k*-space SNR on TRELLIS motion correction: (a) DBE values for uncorrected images (dotted line) and corrected images (solid line) plotted against decreasing SNR. The intersection point near 18 dB indicates the SNR at which TRELLIS motion correction no longer results in an improvement in image quality. Results after introduction of a maximum displacement threshold are shown in (b).

Taking the simulation at 16 dB as an example, TRELLIS results were analysed to identify the main cause of the errors in motion correction. Although estimated values were mostly reasonable, a number of relative displacement values were in error by more than 100 pixels. Referring back to Eq. (6.7), this corresponds to significant errors in **r**. These errors lead to errors in **x**, the vector of displacement values when Eq. (6.7) is solved in a least-squares sense.

A simple solution to this problem is to limit the allowed range of translation. Any relative displacement values, Δx_{pq} and Δy_{pq}, that exceed a certain threshold Δx_{max} or Δy_{max} are ignored and removed from the set of equations to be solved.

The experiment described above with results shown in Fig. 7.7(a) was repeated, this time with maximum translation thresholds in place. The threshold values chosen were 40 pixels for both Δx_{max} and Δy_{max}. These represent the assumed maximum possible translational motion between strips p and q for all allowed values of p and q. In a scanner with a 24 cm field-of-view and image resolution 256×256, this equates to a maximum range of motion of 3.75 cm in the x- and y-directions. Given the restriction imposed by the head coil and head support, this value is reasonable. This value is also well above the motion observed in normal subjects in the experiment described in Appendix B.

Results are given in Fig. 7.7(b). A significant improvement in motion correction for high noise levels is observed. This takes the noise performance of TRELLIS to levels well above that needed for clinical usefulness.

7.5 Effect of pruning

The pruning algorithm for rotation estimation was introduced in Section 6.3.2. Its performance is evaluated here. The simulated motion sequence from Section 7.1 was used again (a range of 9.88° for rotation and no translation). This time the SNR used was 18 dB. This value is relatively low compared to that expected clinically, but was chosen so that errors in rotation estimation become more significant. TRELLIS was used to reconstruct motion corrected data, with and without the pruning algorithm. Results are shown in Fig. 7.8 and show a reduction of nearly 40 % in the error of estimated rotation angles. In each case the estimated rotation angle plots have been shifted vertically to minimise the mean difference between them and the simulated angles. This ensures that the comparison in Fig. 7.8 is fair and is a legitimate adjustment, since strip angles are unchanged relative to the first strip.

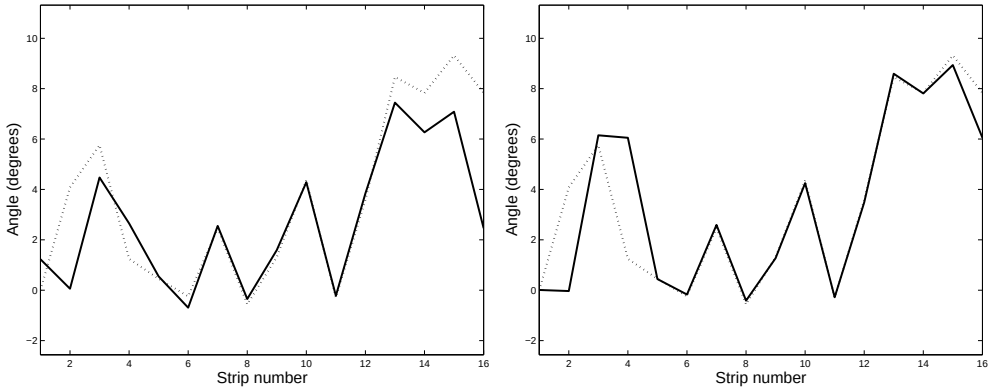

(a) (b)

Figure 7.8 The effect of the pruning algorithm on rotation estimation: (a) without pruning, and (b) with pruning. The mean error in angle estimation is 1.23° in (a) and 0.77° in (b). The SNR used was 18 dB. Simulated motion (dotted line) and estimated motion (solid line) are shown for each case.

It is interesting to note the relative distribution of errors in the estimated values shown in Fig. 7.8. Strips near the centre of *k*-space (numbered 7–10, for example) tend to be more accurately located than those near the edges. This should be expected: data near the centre of *k*-space has greater energy, and therefore greater SNR, than data at the *k*-space periphery. Thus, for acquisitions with a poor SNR, strips at the edges of *k*-space may not be accurately motion corrected.

This observation leads to the next section, where a version of TRELLIS is proposed that omits some of these outer strips.

7.6 Fast TRELLIS

A version of TRELLIS requiring reduced acquisition time is now proposed. Acquisition time is reduced by omitting some of the outer strips of *k*-space data, as depicted in Fig. 7.9. The sequence shown in Fig. 7.9(a) has an acquisition time of 50 % of the original; this sequence is henceforth known as 'fast TRELLIS' and is analysed here. As shown in Fig. 7.9(b), however, other possibilities for reduced acquisition time exist.

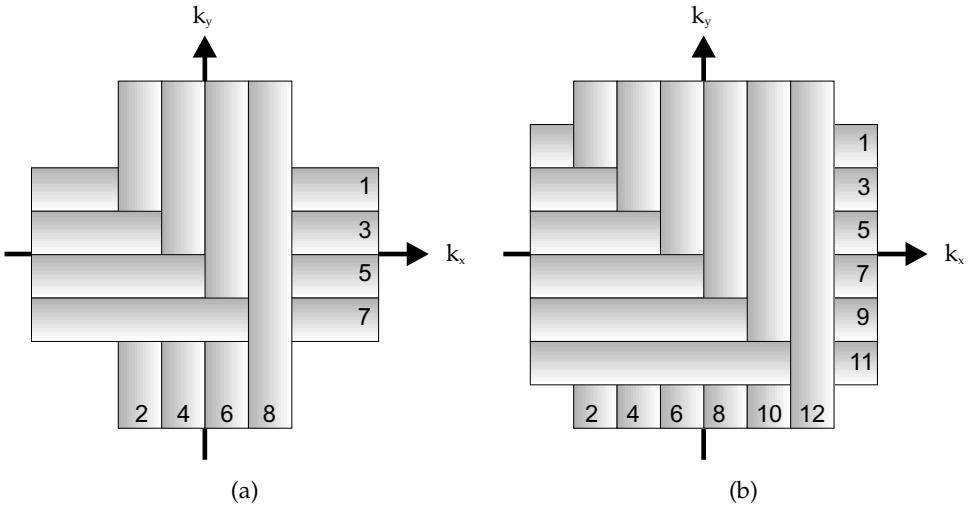

Figure 7.9 A version of TRELLIS requiring only (a) 50 % and (b) 75 % of the acquisition time of the original algorithm by reducing N_s to 8 and 12, respectively, from its original value of 16.

As discussed in the previous section, in cases of poor SNR, outer *k*-space strips may be incorrectly motion-adjusted, rendering them useless. Little is lost, therefore, if these strips are not acquired. The effect on the final image is less obvious, however, in cases of good SNR when every strip is correctly motion-adjusted. To understand this better, it is helpful to examine the contribution of data from different regions of *k*-space to the reconstructed image.

As shown in Chapter 2 (Fig. 2.15), most of the signal energy is found at the centre of *k*-space. The noise energy in MRI, on the other hand, is distributed evenly across all spatial frequencies measured [128, 129]. The SNR therefore drops significantly towards the periphery of *k*-space. Nothing can be gained, therefore, by sampling *k*-space infinitely in each direction as any received signal would be below the noise floor. Furthermore, it has been shown by Watts and Wang [130] that noise does limit spatial resolution in many practical imaging situations and that a 'cutoff *k*-space sampling radius' exists in these cases. Sampling data from outside this region may even degrade the image, due to increased noise.

The exact cutoff depends on the spatial frequency content on the imaged object, as well as the overall SNR, and is thus difficult to determine. Its existence, however, indicates that

the corners of a rectangular acquisition of *k*-space contain little useful information about the image if the resolution in the x- and y-directions is noise limited. Fig. 7.10 illustrates this concept and its applicability to the fast TRELLIS algorithm.

The cutoff radius in Fig. 7.10 is denoted by k_r. Any point in *k*-space further from the centre than k_r does not contribute useful information to the image; rather, the extra noise acquired may reduce image quality. The assumption that the dimensions of *k*-space in the x- and y-directions correspond to k_r will not always be true. This, however, is the case if image resolution is to be maximised.

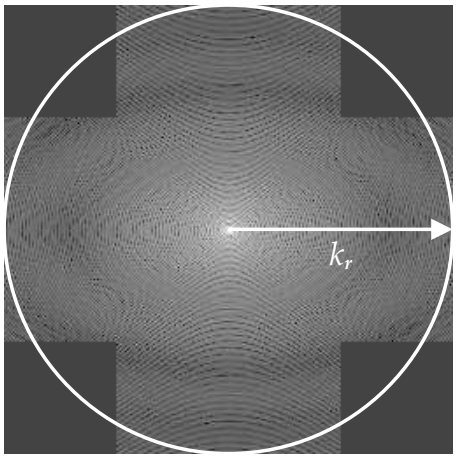

Figure 7.10 The useful sampling radius, k_r, superimposed over *k*-space.

In the example shown in Fig. 7.10, nothing is gained by acquiring data outside the circle; therefore, the fast TRELLIS technique (shown here for a 50 % reduction in acquisition time) results in an information loss of only the unsampled area within the circle. The proportion of the sampled area over the maximum area usefully sampled is

$$S_P = \frac{A_{circ} - 4 \times A_{corners}}{A_{circ}} \approx 0.90 \tag{7.1}$$

where A_{circ} denotes the area of the circle and $A_{corners}$ denotes the area of each unsampled corner within the circle and can be calculated using basic trigonometry.

Eq. (7.1) holds when both the frequency and phase-encode resolutions are set to their noise-limited maximum, as defined by k_r. If the specified resolution is lower than this threshold, then S_P is smaller, and has a minimum value of 0.75; if the specified resolution is higher, then it will be greater, potentially as high as 1.

In terms of information loss when fast TRELLIS rather than the standard version is used, the worst case, therefore, is when the SNR is infinite. In this case $k_r = \infty$, that is, for practical purposes there is no cutoff *k*-space sampling radius and every point sampled contributes information to the reconstructed image.

Fig. 7.11 shows simulation results of this situation. Three different sampling patterns in *k*-space are compared: Fig. 7.11(a) and (b) use the full TRELLIS algorithm; Fig. 7.11(c) and (d) represent fast TRELLIS; and Fig. 7.11(e) and (f) show a reduced resolution image for comparison. There is little visual difference between the images in (b) and (d). The 50 % decrease in acquisition time by using fast TRELLIS over the full version seems, therefore, to be worthwhile. The image in Fig. 7.11(f), however, is of very poor quality due to lower resolution and Gibbs artifacts.

It is possible to describe the effect above in terms of the point spread function (PSF) for each sampling pattern used. Sampling in *k*-space corresponds to multiplying *k*-space data by a binary mask; therefore, the Fourier transform of this binary mask gives the PSF in image-space. Fig. 7.12 shows the corresponding PSFs for the three sampling patterns in Fig. 7.11. The real part of each PSF is shown, and is cropped around the central region for clarity in the diagram. Not surprisingly, the PSF corresponding to Fig. 7.11(a), shown in Fig. 7.12(a), is simply an approximation to a delta function. The sampling pattern in Fig. 7.11(c), produces a PSF consisting of a main peak with some small side lobes (Fig. 7.12(b)). The sampling pattern in Fig. 7.11(e), however, produces a PSF consisting of side lobes that are a significant proportion of the magnitude of the main peak (Fig. 7.12(c)).

7.7 Summary

In the simulations described in this chapter, TRELLIS has performed well at estimating and corrected rigid-body rotation and translation. Results indicate that TRELLIS performs at noise levels above that expected in a clinical setting. It is important to note, however, that simulations have not included a number of imperfections that are present in practice. Rather than attempting to account for the effects of these (with no guarantee of successfully replicating these effects), further testing requires the use of moving physical phantoms and human subjects. This is the subject of the following chapter.

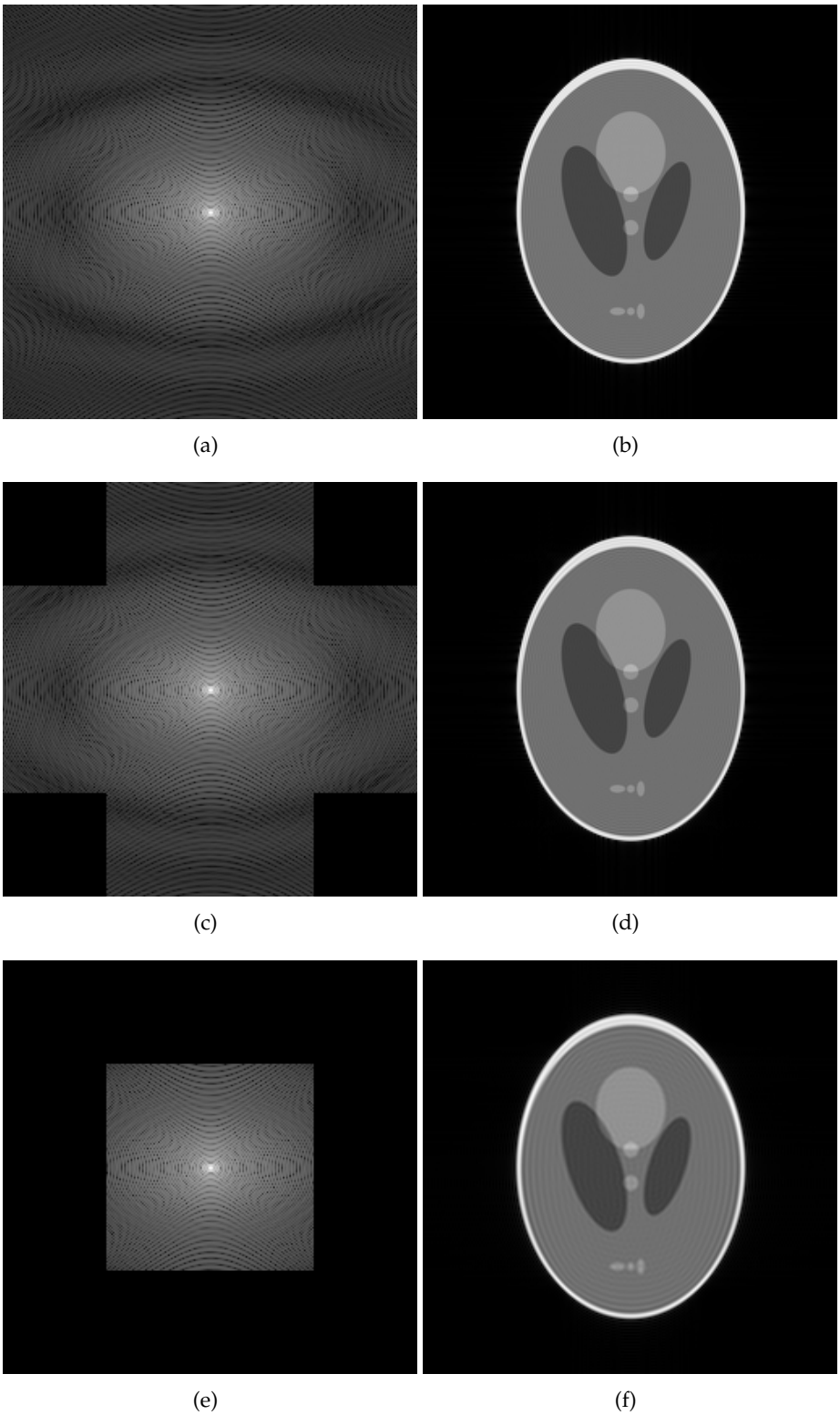

(a) (b)

(c) (d)

(e) (f)

Figure 7.11 Three different sampling patterns in k-space, (a), (c) and (e), and the reconstructed images that result from these, (b), (d) and (f), respectively. Unsampled data points in (c) and (e) are replaced with zeros.

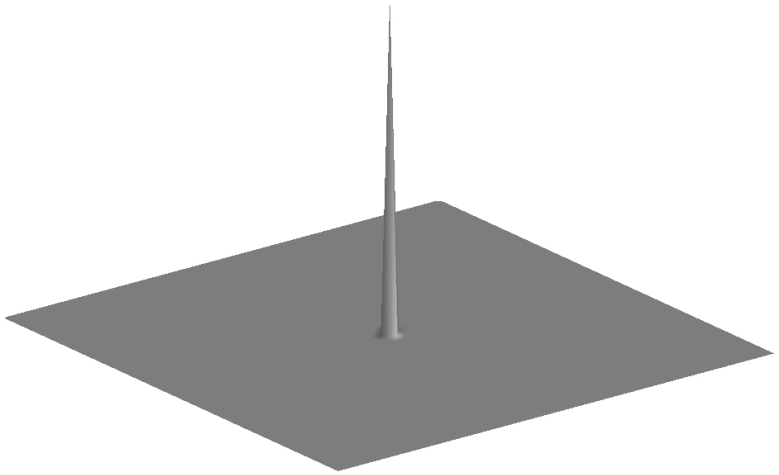

(a)

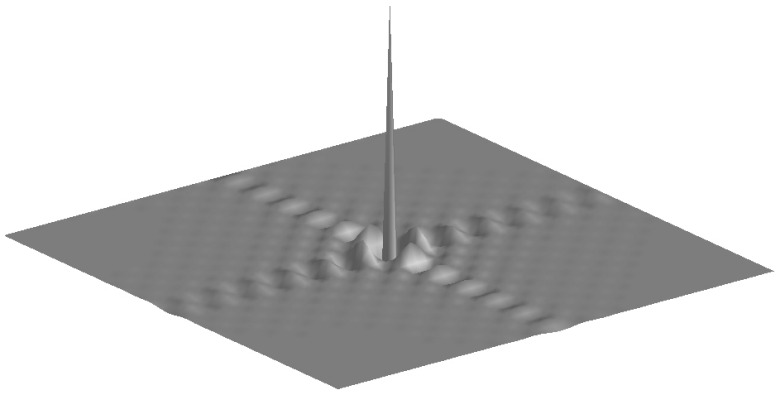

(b)

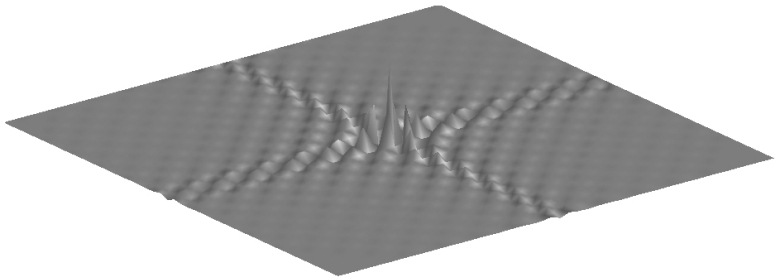

(c)

Figure 7.12 Point spread functions: (a), (b) and (c) correspond to the sampling patterns shown in Fig. 7.11(a), (c) and (e), respectively. The real part of the PSF, cropped around the central peak, is shown here in each case. Each figure is scaled identically.

Chapter 8

TRELLIS: Scanner Implementation

Given the promising simulation results presented in the previous chapter, TRELLIS was implemented on an MRI scanner and ethical approval to scan human subjects was obtained. This chapter briefly describes initial attempts made to implement TRELLIS in practice and then discusses the final implementation in detail. Numerous practical problems were encountered and solutions to these are presented here. Results show that, in agreement with simulations, TRELLIS can be an effective motion-correcting tool [131].

8.1 Pulse sequence development

The data acquisition stage of the TRELLIS algorithm was implemented in the EPIC[1] programming environment (GE Medical Systems, Milwaukee, USA). Software versions used were 11m4 and 14m3; the change corresponds to a GE upgrade on the scanner used. Simulations were run using WTools, the built-in development tool, to ensure code was functioning correctly. This prevented wasting limited scanner time.

8.1.1 Gradient echo experiments

Initial experiments provided a 'bridge' between simulation studies and more realistic experiments. Data were collected from a phantom using a 1.5 T Signa Excite HDx scanner (GE Medical Systems), but rotational motion was simulated by adjusting the scanner gradients.

A standard gradient echo sequence (GE's *2Dfast*) was modified to allow the collection of k-space data at an arbitrary angle. Control variables (variables adjustable by the user at the time of scanning) were established to control the required rotation angle of the acquisition.

[1] Environment for Pulse Programming in C.

The scanner gradients were then manipulated using a rotation matrix applied to the k-space coordinate system that maps logical gradients to physical gradients.

Data were collected from a phantom using the modified 2Dfast sequence for a range of different angles. Two 'composite' k-space data sets, **H** and **V**, were then created by taking strips of data from each scan. **H** comprised k-space data acquired at 0°, 5°, 10° and 15°, while **V** comprised k-space data acquired at 90°, 95°, 100° and 105°. All data within each individual TRELLIS strip were collected at the same rotation angle.

TRELLIS motion correction and estimation was then applied. Reconstructed images before and after motion correction are shown in Fig. 8.1(a) and (b), respectively. The mean error in estimation of rotation angles was 0.05°. Ideally, estimated translation values would equal zero in this case. There were, however, small errors: the mean estimated (absolute) translation value for each strip was 0.08 pixels in the x-direction and 0.12 pixels in the y-direction. The motion corrected image is of good quality, however.

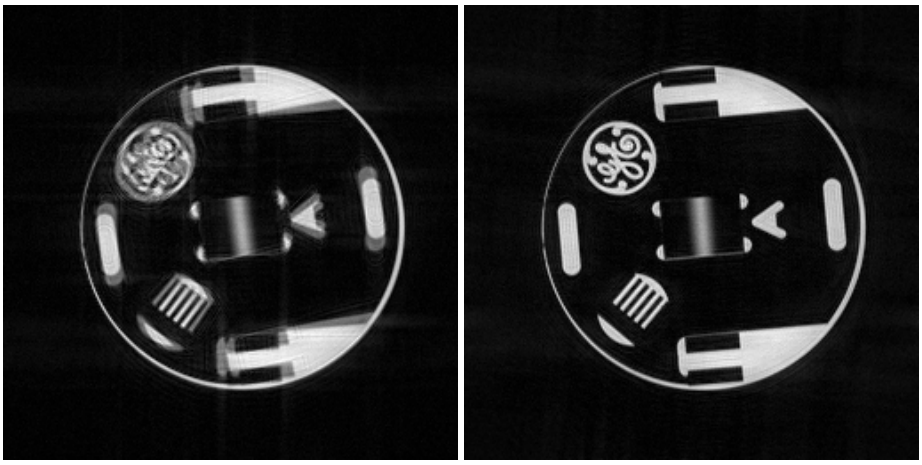

(a) (b)

Figure 8.1 Phantom data collected during motion simulated by rotation of the scanner gradients: (a) the reconstructed image, and (b) after correction by TRELLIS.

A second experiment was performed where the k-space coordinate system was continuously rotated during data acquisition. To test motion correction in TRELLIS, k-space strips were arbitrarily assigned in **H** and **V**, despite the fact that data were collected in individual lines, not strips composed of a number of lines. Not surprisingly, motion estimation and correction failed in this case: the assumption that no motion occurred during the acquisition of each individual strip was violated, making the correlation of overlapping strips difficult.

Clearly, it is important that each TRELLIS strip is acquired rapidly so that minimal motion occurs. The time delay between strips is not important: motion between strips is corrected

by TRELLIS. The initial gradient echo sequence used is not suited to these requirements so alternatives were investigated.

8.1.2 EPI implementation

Echo planar imaging, or EPI, was briefly mentioned in Section 3.3.1 where fast imaging methods were discussed. It is possible to acquire an entire image, albeit at low resolution, in less than 100 ms. This is achieved by using a single RF pulse followed by a series of gradient-echo trains.

It is also possible to use multiple-shot EPI, where multiple RF pulses are interleaved to acquire *k*-space piece-by-piece as shown in Fig. 8.2(a). A higher resolution image can thereby be formed than when using single-shot EPI, although imaging time is much longer. As multiple lines can be acquired in a single RF pulse, EPI is a logical means of implementing TRELLIS. Each strip in **H** and **V** is acquired in a single-shot in around 10 ms, meaning that motion within the acquisition time for a strip is likely to be small. The acquisition scheme used is depicted in Fig. 8.2(b) for **H** data with 4 strips ($N_s = 8$). In practice, values used for N_s were 16 and 32.

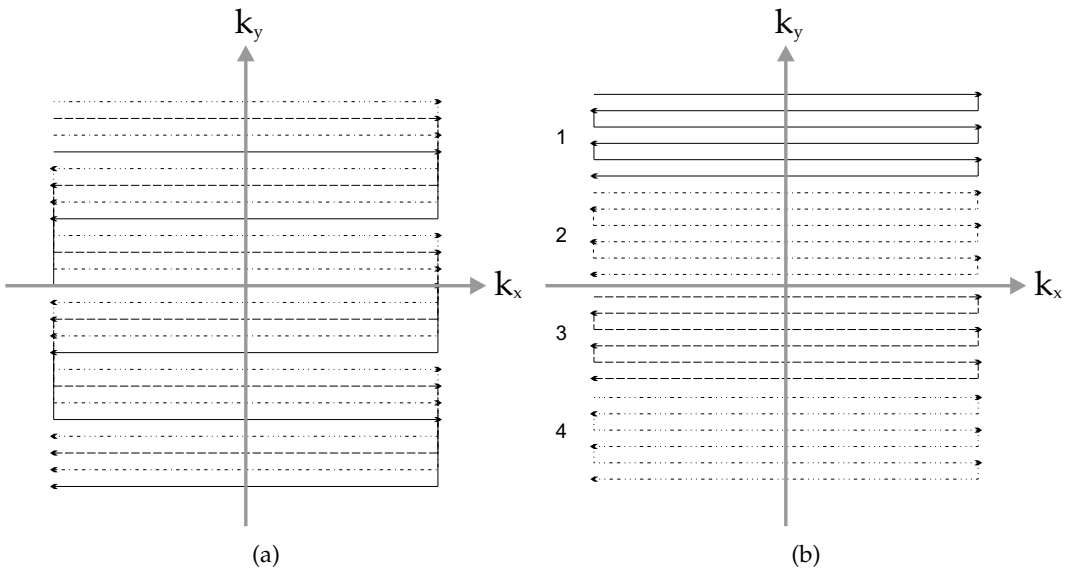

Figure 8.2 (a) A typical multiple-shot interleaved EPI sequence. (b) The version modified for TRELLIS. The number of shots shown here to acquire **H** (4) is less than that actually used in practice for TRELLIS (8 or 16).

EPI was used to implement TRELLIS by modifying the standard GE EPI sequence. The odd lines in *k*-space are acquired in the opposite direction to the even lines. Every second line of *k*-space was therefore flipped in the FE direction to compensate for this. This operation, normally referred to as *row flipping*, is standard practice in EPI image reconstruction [4]. Collected data and a reconstructed image (after row flipping) is given in Fig. 8.3.

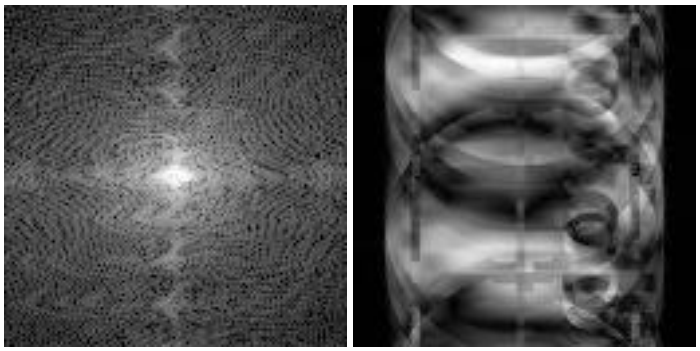

(a) (b)

Figure 8.3 (a) TRELLIS *k*-space magnitude data (**H** data only) acquired using the EPI implementation. (b) The image reconstructed from **H** exhibits very destructive artifacts. The image is a slice through a standard GE phantom and should be circular.

EPI is very prone to artifacts and is particularly sensitive to imperfections in the system such as inhomogeneities in the main magnetic field and phase errors caused by eddy currents. These are corrected to some extent in the GE implementation of the EPI sequence by acquiring reference lines through *k*-space to quantify phase inconsistencies (refer to [4] for more information about this process). The same technique was applied to TRELLIS but with little success. The author suggests that the errors mentioned above apply to the TRELLIS implementation in Fig. 8.2(b) more so than the standard interleaved EPI sequence in Fig. 8.2(a) as they cause a modulation of *k*-space, leading to severe ghosting (see Fig. 8.3(b)).

Work by Skare et al. [69] applying EPI to PROPELLER with reduced artifacts could possibly be also applied to TRELLIS. Instead of acquiring PROPELLER blades line-by-line *along* each blade, data is collected line-by-line *across* each blade (called 'short axis PROPELLER' in [69]). This might mitigate some of the artifact problems encountered but was not attempted here. Instead, fast spin echo (FSE) was investigated as an alternative means of implementing TRELLIS.

8.1.3 FSE implementation

For TRELLIS to work successfully, acquisition time for each strip must be small, so that motion occurring while a strip is acquired is negligible. EPI is a obvious choice to satisfy this requirement. As seen in Fig. 8.3, however, severe artifacts in the reconstructed image result in the author's EPI implementation of TRELLIS.

An alternative to EPI is fast spin echo (FSE), mentioned in Section 3.3.1. As is the case for EPI, FSE can be used to rapidly acquire an entire image to avoid motion artifacts. Again, the amount of data that can be acquired in a single shot is limited; thus, image resolution is restricted somewhat. An advantage of FSE over EPI, however, is the relative robustness

of FSE to imperfections in the imaging system.

FSE uses a train of refocusing pulses to produce multiple spin echoes and it is thus possible to acquire multiple *k*-space lines in a single excitation pulse (a single shot). TRELLIS was implemented using this approach by modifying the GE FSE sequence. The echo train length (N_{etl}) gives the number of spin echoes and the number of lines acquired in a single shot. The FSE implementation of TRELLIS uses a single shot to acquire all lines in each strip within **H** and **V**. Thus, the strip width in lines is equal to the echo train length, and is also denoted by N_{etl}.

The order of acquisition used was all horizontal strips (left to right) followed by another scan containing all vertical strips (top to bottom). This is shown in Fig. 8.4. The reason for acquiring all strips in **H** followed by all strips in **V**, rather than using the interleaved scheme shown in Fig. 6.1, is simplicity of implementation. This order is not important for image reconstruction – the only requirement is that individual strips are acquired rapidly. The relative timing between strips is currently not used by TRELLIS.

The time interval between the acquisition of each consecutive strip is equal to the T_R of the FSE sequence (around 2000 ms). This is longer than the time required to acquire each strip (around 100 ms) by a factor of approximately 20 (depending on scan parameters). Therefore, the assumption that most motion occurs between the acquisition of each strip and not during the acquisition of each strip is reasonable.

Arrows in Fig. 8.4(a) and (b) indicate the phase-encode direction for each strip in **H** and **V** respectively. The phase-encode direction is alternated between neighbouring strips to reduce discontinuities in *k*-space caused by T_2 decay. This is discussed further in Section 8.2.2 and in Chapter 9.

8.2 Post-processing

Using the FSE implementation of TRELLIS, collected data must be post-processed before TRELLIS motion correction can take place. Unlike EPI, all lines are acquired in the same direction so there is no need for row-flipping. There are, however, two other steps that must be carried out: *k*-space alignment and T_2 blurring correction. These are discussed in this section.

8.2.1 K-space alignment

The *k*-space data sets **H** and **V**, taken in their entirety, may be incorrectly centred (relative to the *k*-space origin) or misaligned (with respect to each other) due to eddy currents and

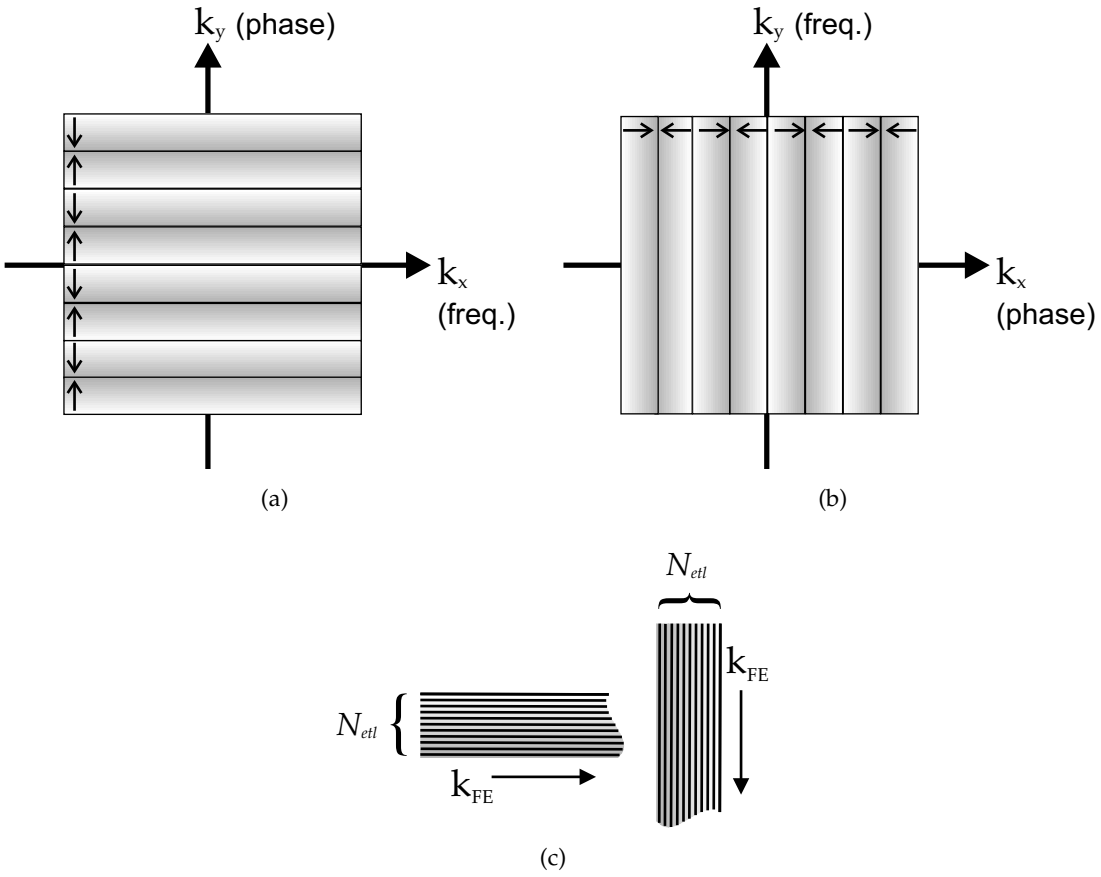

Figure 8.4 TRELLIS data collection for $N_s = 16$ using FSE: (a) shows acquisition of 8 horizontal strips forming the set **H**, (b) shows acquisition of 8 vertical strips, forming the set **V**. The phase-encode direction is indicated by arrows for each strip. Each strip comprises N_{etl} lines as shown in (c), with the frequency-encode (FE) direction indicated.

other imperfections in the system, such as slight differences between the gradients. They must therefore be aligned and centred for subsequent processing.

Misalignment between **H** and **V** manifests itself as a spatially varying phase difference between the two data sets after inverse transformation to image-space, which leads to cancellation if the two complex data sets are combined, as illustrated in Fig. 8.5(a). To align **H** and **V** in *k*-space the phase correlation method presented in Section 6.4.2 is used again.

The process is summarised here using **H** and **V**, rather than the overlapping patches in *k*-space mentioned in Section 6.4.2 (the main difference between the two cases is that the displacement to be determined is in a different domain). First, denote the inverse discrete Fourier transforms of **H** and **V** as $\tilde{\mathbf{H}}$ and $\tilde{\mathbf{V}}$, respectively, defined in image-space. The procedure is as follows:

1. Form a two-dimensional phase ramp function, $\Delta\Phi$, from the phase difference be-

tween $\tilde{\mathbf{H}}$ and $\tilde{\mathbf{V}}$ in image-space.

2. Discrete Fourier transform the function $e^{i\Delta\Phi}$ and find the coordinates of the resulting maximum value in *k*-space. These provide an estimate of the slope of $\Delta\Phi$ and hence an estimate of the displacement between **H** and **V** in *k*-space.

3. To obtain sub-pixel accuracy, repeat step 2. This time compute the DFT for values at and around the peak previously found in step 2 in order to achieve a 100-fold increase in resolution of the peak location in *k*-space. The method for computing the DFT in this way was described earlier in Section 6.4.2.

4. Add a phase ramp (with the slope found in step 3) to $\tilde{\mathbf{V}}$ in image-space and Fourier transform. This produces a new version of **V**, now aligned with **H** in *k*-space.

Once *k*-space alignment is complete, a constant phase offset between **H** and **V** may still exist. This is undesirable, as it is necessary to combine the two data sets later and any phase offset may result in signal cancellation. To remove this offset, the phase distribution of the central 20×20 points in each data set **H** and **V** is computed. The difference between the peaks of the distributions corresponds to the phase offset between **H** and **V**. A constant phase is added to **V** to correct for this.

When **H** and **V** are aligned, and have a similar phase, the addition of **H** and **V** no longer results in signal cancellation (Fig. 8.5(b)).

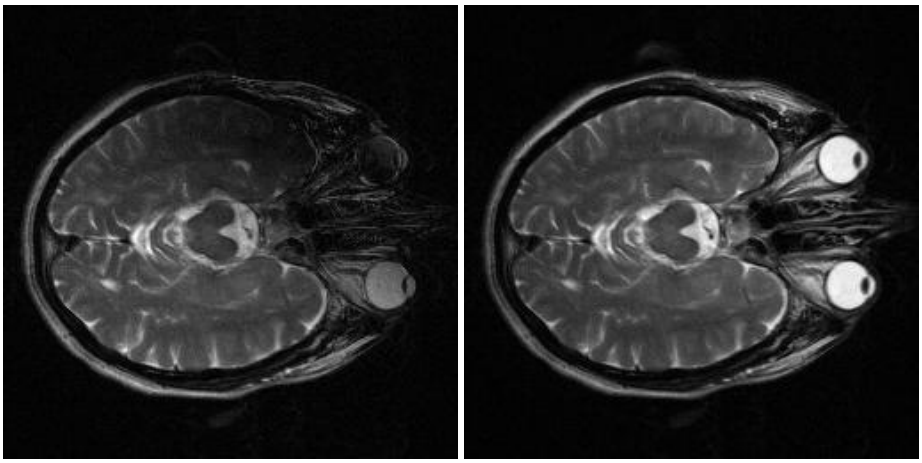

(a) (b)

Figure 8.5 (a) Poor *k*-space alignment of **H** and **V** leads to cancellation in image-space if the two data sets are combined. (b) Correction by phase correlation prior to combination of **H** and **V** solves this problem.

It is normally the case that **H** and **V**, although now aligned with respect to each other, are not exactly centred in *k*-space. The TRELLIS algorithm uses knowledge of the centre of *k*-space to determine the centre of rotation; thus, it is important that this is accurate.

The sum $\mathbf{S} = \mathbf{H} + \mathbf{V}$ is formed, and used to determine the displacement of both **H** and **V** away from the *k*-space centre. Experience has shown that prior alignment of **H** and **V** before finding the *k*-space centre is more accurate than finding the centres of **H** and **V** individually. If **S** is not correctly centred in *k*-space, a phase ramp will be present in $\tilde{\mathbf{S}}$, the inverse Fourier transform of **S**. This phase ramp is shown in Fig. 8.6(a). This is used to identify, and correct for, the displacement from the *k*-space origin in the same way as the displacement between **H** and **V** was found. It is also possible to locate the *k*-space centre using a 'centre of mass' approach based on *k*-space magnitude; this alternative method appears to be equally effective.

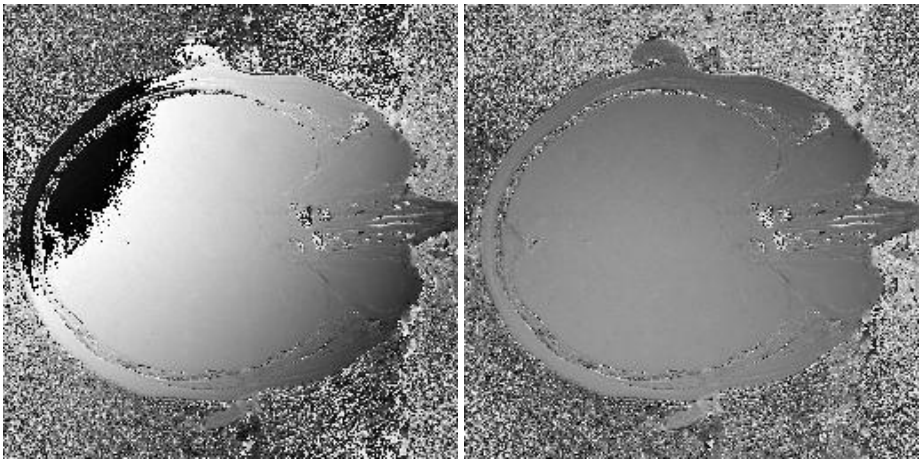

(a) (b)

Figure 8.6 (a) If **S** is incorrectly centred in *k*-space, a phase ramp is present in its Fourier transform in the image domain, $\tilde{\mathbf{S}}$. The slope of this phase ramp indicates the displacement of **S** from the centre of *k*-space. (b) After correction, the linear phase variation across $\tilde{\mathbf{S}}$ is no longer present.

8.2.2 T2 blurring correction

The decay of transverse magnetisation due to T_2 effects was discussed in detail in Section 2.3. This has important implications for the implementation of TRELLIS using FSE.

Signal amplitude decay due to T_2 effects causes a modulation of the *k*-space data. In turn, this produces blurring in the image in the direction corresponding to phase-encoding. The reasons for this are discussed in detail in Chapter 9. This problem is partly mitigated by reversing the order of acquisition of lines within neighbouring strips (see Fig. 8.4(a) and (b)). Despite this reversal of direction, some blurring remains. The effect of the modulation on *k*-space and image-space (**H** and $\tilde{\mathbf{H}}$ data only) is shown in Fig. 8.7(a) and (b) for one slice of the phantom constructed by the author. Note the blurring in the phase-encode direction in Fig. 8.7(b). The effect is especially obvious here, due to the relatively short T_2 of the fluid in the phantom (approximately 250 ms, compared to about 2200 ms for CSF in the brain).

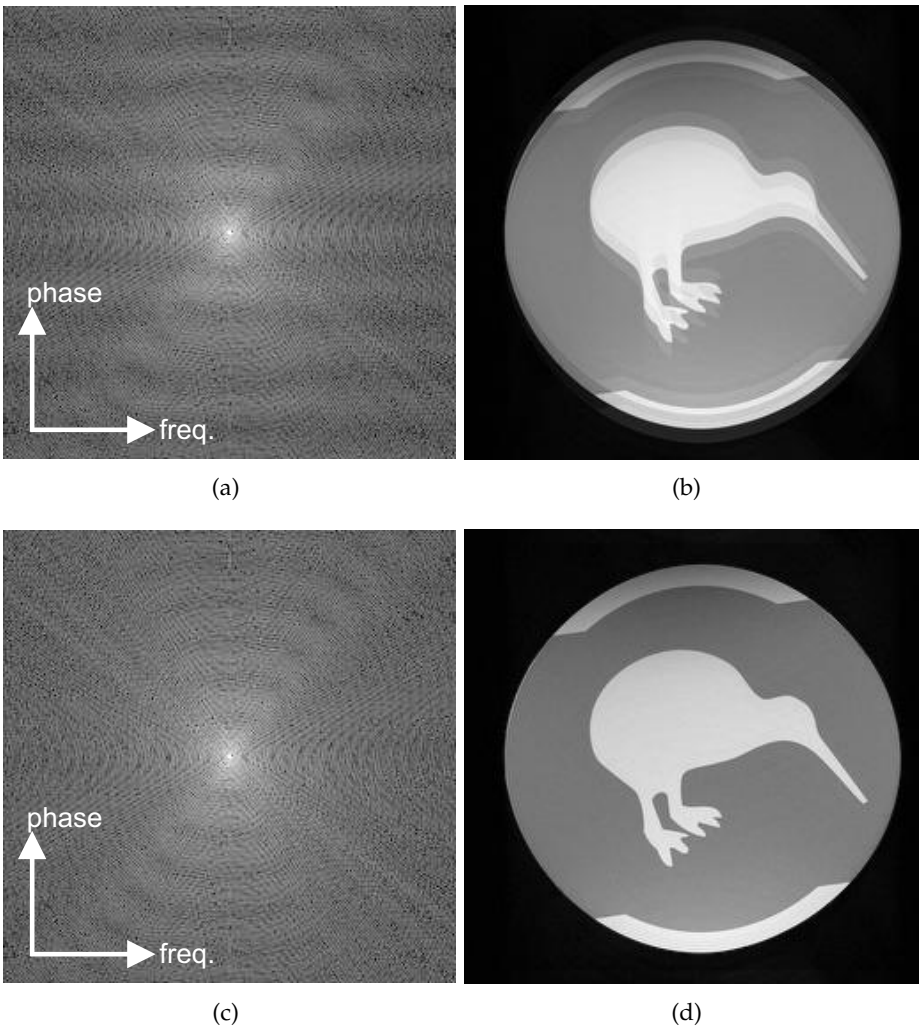

Figure 8.7 Correction of **H** data using T_2 demodulation. Before correction: (a) log *k*-space magnitude and (b) reconstructed image. After modulation correction: (c) log *k*-space magnitude and (d) reconstructed image. Note the reduced blurring in the phase-encode direction in (d) compared to that in (b).

Not only are the artifacts resulting from T_2 decay undesirable, but the magnitude decay in *k*-space causes errors in the rotation estimation stage of TRELLIS. Thus, T_2 correction is required. If the modulation function can be estimated, then its effect can be undone to some extent.

This is not the first time an attempt has been made to reduce T_2 effects in MRI images acquired using FSE. Chen et al. [132], for example, have attempted to enhance MR images degraded by T_2 effects. Their algorithm estimates a single T_2 value from the acquired data, based around the Hermitian symmetry property of *k*-space. They note, however, that T_2 correction based on this single estimated value of T_2 may result in a under- or over-compensation for certain objects in the image. Similar techniques have also been applied

by others [133, 134].

A similar approach to that discussed above was initially used by the author and results were reasonable in some cases. An obvious weakness, however, is that such a technique does not take advantage of the unique situation provided by TRELLIS, namely, that k-space is acquired twice, and that the two acquisitions are perpendicular to each other. A new technique was therefore developed here.

The modulation function is estimated directly from the complete **H** and **V** data sets. To obtain m_H, the modulation function in the phase-encode direction in the **H** data set, the magnitudes of both **H** and **V** k-space data sets are summed along their rows to form two vectors. Dividing the **H** vector by the **V** vector element-by-element yields the noisy estimate of m_H shown in Fig. 8.8(a). Denoting the number of frequency-encode samples as N_{kx} and the number of lines acquired in the phase-encode direction as N_{ky}, this procedure can be expressed as

$$m_H(k_y) = \frac{\sum_{k_x=1}^{N_{kx}} |H(k_x, k_y)|}{\sum_{k_x=1}^{N_{kx}} |V(k_x, k_y)|}, \quad k_y = 1, 2, \ldots, N_{ky}\,. \tag{8.1}$$

As seen in Fig. 8.8(a), the modulation function, m_H, is approximately periodic with a period corresponding to the eight pairs of opposing strips used in this example. A smoother modulation function, shown in Fig. 8.8(b), is formed by combining the eight repeating sections in Fig. 8.8(a) to form an average and replicating this unit eight times to form an exactly periodic function. The **H** data is then corrected by normalising each row of **H** using the modulation function (Fig. 8.7(c) and (d)). The same process is used to correct **V**, but the initial summation is performed down each column rather than along each row.

Imperfections in the final image caused by T_2 signal decay still exist, particularly in the case of human subjects where T_2 values vary widely between different tissue types. Nevertheless, the two steps described here greatly mitigate the effect.

An alternative approach to estimating the modulation function is also proposed here. This produces a similar final result to the technique already mentioned, but has a more solid theoretical justification. First, the assumption is made that T_2 effects are negligible within each single k-space row (for H) or column (for V). This is reasonable: in a standard interleaved sequence, T_2 blurring is almost unnoticeable in the FE direction and TRELLIS

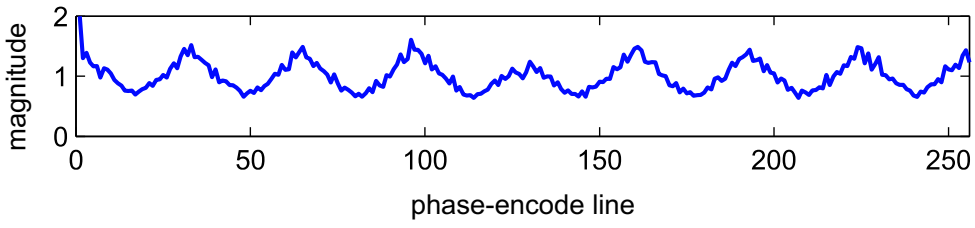

(a)

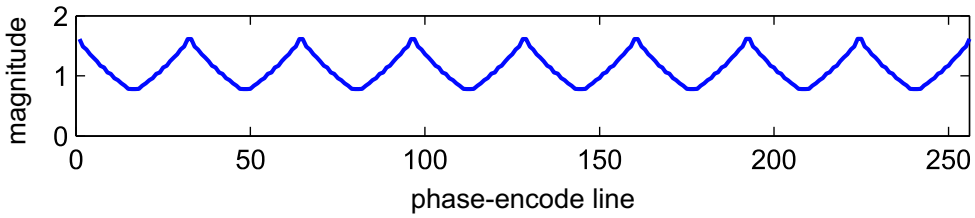

(b)

Figure 8.8 (a) The initial modulation function, m_H, as a function of k_y computed for the data shown in Fig. 8.7. (b) The eight repeating sections in (a) are averaged to form a single T_2 decay curve which is then replicated eight times along the length of k_y to form the final smoothed periodic function. The vertical axis on each plot shows the relative magnitude of the *k*-space data plotted as a function of position in *k*-space in the phase-encode direction.

H and **V** acquisitions do not differ from a standard sequence in the FE direction (the only change is to the PE ordering). Again denoting the T_2 modulation for H as m_H and that for V as m_V, we have therefore

$$|H(k_x, k_y)| = |F(k_x, k_y)|\, m_H(k_y) \tag{8.2}$$

$$|V(k_x, k_y)| = |F(k_x, k_y)|\, m_V(k_x), \tag{8.3}$$

where $F(k_x, k_y)$ is the *k*-space data that would be measured in the absence of T_2 modulation. Clearly, the aim in estimating the T_2 modulation is to estimate $F(k_x, k_y)$ from H and V. Given Eqs (8.2) and (8.3), dividing one *k*-space magnitude measurement by the other at each point in the space gives a set of equations of the form

$$\frac{|H(k_x, k_y)|}{|V(k_x, k_y)|} = \frac{m_H(k_y)}{m_V(k_x)}. \tag{8.4}$$

To linearise these, the logarithm of each side is taken to form

$$\ln\left(\frac{|H(k_x,k_y)|}{|V(k_x,k_y)|}\right) = \ln\left(m_H(k_y)\right) - \ln\left(m_V(k_x)\right). \tag{8.5}$$

Without loss of generality, let the dimensions of the *k*-space measurements be $N \times N$. For simplicity, row and column coordinates for the *k*-space data sets are adopted, so that (m,n) corresponds to the point in *k*-space for the pixel occupying the mth row and nth column, where m and n both number from 1 to N. A lexicographic ordering of the pixels is adopted to form a one-dimensional vector of all pixels. A sparse set of linear equations can then be formed from Eq. (8.5) as

$$\mathbf{A}\,\mathbf{x} = \mathbf{b}. \tag{8.6}$$

In Eq. (8.6), the elements of the $2N$ vector $\mathbf{x}$ are

$$x_j = \begin{cases} \ln(m_H(j)) & j = 1,\ldots,N \\ \ln(m_V(j-N)) & j = (N+1),\ldots,2N\,, \end{cases} \tag{8.7}$$

and the elements of the N^2 vector $\mathbf{b}$ are

$$b_i = \ln\left(\frac{|H(m,n)|}{|V(m,n)|}\right) \quad , i = (N-1)m + n. \tag{8.8}$$

The matrix $\mathbf{A}$ is $N^2 \times 2N$. Each row in $\mathbf{A}$ contains two non-zero elements, of value 1 and -1, positioned so that Eq. (8.5) is satisfied. A least squares solution for $\mathbf{x}$ can straightforwardly be obtained. To avoid the inherent rank deficiency in $\mathbf{A}$, $m_H(1)$ is set to 1, thus reducing the number of unknowns to $(2N-1)$.

The results are very similar to those shown in Fig. 8.8(a). The difficulty with this approach is that it appears to require a computationally expensive inversion due to the size of the system being solved. Fortunately, it is possible to compute the least-squares solution directly. This derivation is given in Appendix C. This technique is the one used for the remaining TRELLIS results presented.

8.3 Results

The implementation of TRELLIS described in Section 8.1.3 was tested using a 1.5 T Signa Excite HDx scanner (GE Medical Systems) at St George's Hospital in Christchurch, New Zealand. This section is divided into two parts: results collected using the moving phantom described in Section 4.2.1, and results obtained from imaging human subjects.

8.3.1 Experiments using a moving phantom

The moving phantom described in Section 4.2.1 was imaged using both a standard FSE sequence and using TRELLIS. In each case, the *k*-space matrix size used was 256×256, $N_{SA} = 1$, and the slice thickness was 10 mm. The phantom motion was a pre-programmed rotation sequence, which was started simultaneously with the scanner data acquisition. The current implementation of the TRELLIS sequence is effectively split into two scans, where **H** and **V** are obtained separately. Phantom motion was started in the same place for each of these. This synchonisation was performed manually; ideally an automated method would be used but this has not yet been developed.

Echo train lengths of both 16 and 32 were used successfully. For results shown here, parameters were $N_{etl} = 16$, giving N_s = 32. Therefore, **H** and **V** comprise 16 strips each. The value of the repetition time used, T_R, was 2000 ms. This is the time between the acquisition of each strip.

Reconstructed images obtained from this experiment are shown in Fig. 8.9. These correspond to interleaved FSE (a), TRELLIS without motion correction enabled (b), and TRELLIS with motion correction (c). The image in (b) is reconstructed from combined **H** and **V** data after *k*-space alignment and T_2 correction, but without motion estimation or correction.

Fig. 8.9(a) shows a considerable amount of ghosting in the phase-encode direction (horizontal, in this case). This is often seen in motion-corrupted images obtained using an interleaved FSE sequence. The images in Fig. 8.9(b) (TRELLIS with no motion correction) and Fig. 8.9(c) (TRELLIS with motion correction) are significantly less motion-corrupted although the motion of the object was the same in all cases. Not surprisingly, the relatively large motion (a maximum range of 14°) produces a marked blurring in Fig. 8.9(b) when no rotation correction is employed. The rotation-corrected reconstruction shown in Fig. 8.9(c) shows a greatly improved result.

To compare the fast TRELLIS algorithm (Section 7.6) to the regular version of TRELLIS, the outer strips in **H** and **V** are omitted resulting in a reduced number of strips. In the following, the number of strips used is henceforth denoted N_s', where $N_s' \leq N_s$. This is

(a) (b) (c)

Figure 8.9 Moving phantom results: (a) an image obtained using standard interleaved FSE with an echo train length of 16; (b) an image reconstructed using TRELLIS with motion correction disabled; and (c) an image reconstructed using TRELLIS with motion correction. Phantom motion used was a repeating rotation sequence (up to 14° in magnitude).

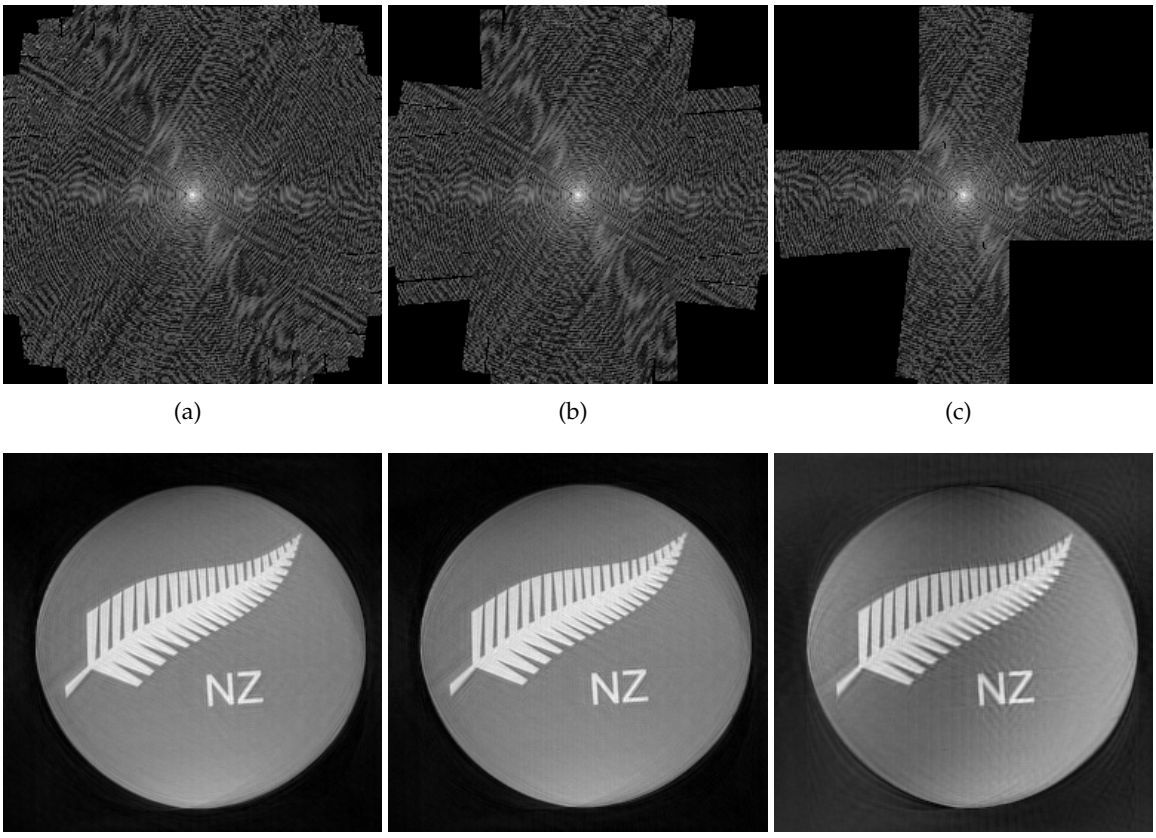

(a) (b) (c)

(d) (e) (f)

Figure 8.10 Corrected *k*-space data after applying the fast TRELLIS algorithm for three different values of N_s': 24 (a), 16 (b), and 8 (c). The respective reconstructed images are shown below in (d)–(f).

distinct from N_s, which denotes the number of strips that are required to *completely* fill **H** and **V** for a given *k*-space matrix size and echo train length. In the results shown in Fig. 8.9, the N_s' value used was 32. In Fig. 8.10, results are presented using N_s' values of 24, 16 and 8. When N_s' of 24 and 16 is used, the resulting image appears better that that in Fig. 8.9(c). This is due to errors in the translation estimation stage of the algorithm for patches in the outer region of *k*-space. In fast TRELLIS, these strips are omitted removing these errors from the estimation process. Using $N_s' = 8$ results in a reconstructed image showing artifacts presumably caused by the sub-sampling of *k*-space. Thus, the choice for N_s' here is 16, resulting in a good quality image in half the acquisition time of the normal TRELLIS sequence.

DBE values for the images in Fig. 8.10 have not been computed. The images have different spectral weightings due to the different portions of *k*-space that they sample and this would presumably affect the DBE metric. Without having quantified this effect, it is best to leave the judgment of image quality to the observer.

Fig. 8.11 compares the rotation parameters of the phantom estimated by TRELLIS with those measured using an independent optical tracking system. The tracking system consists of a video camera recording images of a marker attached to the top of the phantom at a rate of 15 frames per second. The measurements were not simultaneous with the MR data collection as the optical system has not yet been used in an MR environment. Fig. 8.11(a) is a plot of angle versus time for one cycle of the phantom rotation, as determined by the optical tracking system. Figures Fig. 8.11(b) and Fig. 8.11(c) show the angles for the phantom rotation estimated by TRELLIS for the set of horizontal *k*-space strips and for the set of vertical *k*-space strips, respectively, with angle plotted against strip number in each case. There is an acceptable level of qualitative agreement between the three plots.

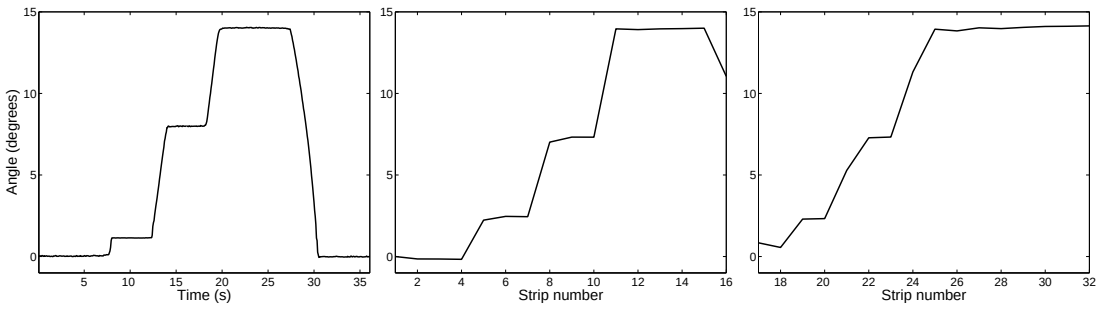

Figure 8.11 Plots of rotation for the moving physical phantom: (a) estimated by an independent optical system (angle vs time); (b) estimated by the algorithm from the set of 16 *k*-space strips in **H** (angle vs strip number); and (c) estimated by the algorithm from the set of 16 *k*-space strips in **V** (angle vs strip number).

The slope of the curve in Fig. 8.11(b) looks somewhat different to that in Fig. 8.11(c). The

author conjectures that this is due to a slight timing difference between the acquisition of the two data sets **H** and **V**. In each graph, there are only 16 data points; these correspond to each of the 16 strips in **H** and **V**. Sampling the curve in Fig. 8.11(a) with only 16 points could lead to either of the plots in Fig. 8.11(b) and Fig. 8.11(c) depending on the time delay of the samples. If the phantom motion started at a slightly different time compared to imaging, then this would explain the result. Estimated angles for strips 30–32, however, are probably in error. The author recommends that future work should involve simultaneous tracking of the phantom motion during the TRELLIS acquisition.

8.3.2 Results using human subjects

Ethics approval was obtained for this study from the Upper South B Regional Ethics Committee (Christchurch, New Zealand) under the project title: *Correction of Motion Artifacts in Magnetic Resonance Imaging*. Informed consent was obtained from several normal, healthy volunteers. The information sheet and consent form given to each subject (as required for ethics approval) are included in Appendix D.

Subjects were imaged using both interleaved FSE and the TRELLIS sequence and were told to move their head in all directions throughout the scan and to try and to make this motion as consistent as possible between scans. Thus, through-plane motion existed but was not corrected for. This would also be the case in a clinical situation.

The TRELLIS sequence with matrix size 256×256 and $N_{SA} = 1$ was used for imaging. Parameters were $N_{etl} = 32$, $N'_s = N_s = 16$, TR = 4520 ms, and slice thickness 10 mm.

Typical results are shown in Fig. 8.12 for imaging using a standard FSE sequence (a), using TRELLIS without motion correction (b), and using TRELLIS with motion correction (c). The maximum motion detected was rotation of 3.8° and translation of 1.6 pixels (x-direction) and 3.6 pixels (y-direction). The reduction in ghosting from (a) to (b) is obvious, indicating the high sensitivity of interleaved acquisitions to motion. Due to the relative insensitivity to motion of the TRELLIS sequence, the differences between (b) and (c) are small. Note, however, the improved appearance of the middle cerebral artery and the eye in (c), as indicated by arrows.

In Fig. 8.12, image contrast differs between (a) and (b)–(c). This is due to different effective echo times (the time point at which the *k*-space centre is sampled) between the FSE and the TRELLIS sequences.

Again, the fast TRELLIS sequence was compared to the regular version of TRELLIS. In the results shown in Fig. 8.12, the N'_s value used was 16. In Fig. 8.10, results are presented using N'_s values of 12, 8 and 4. As for the moving phantom, fast TRELLIS performs well

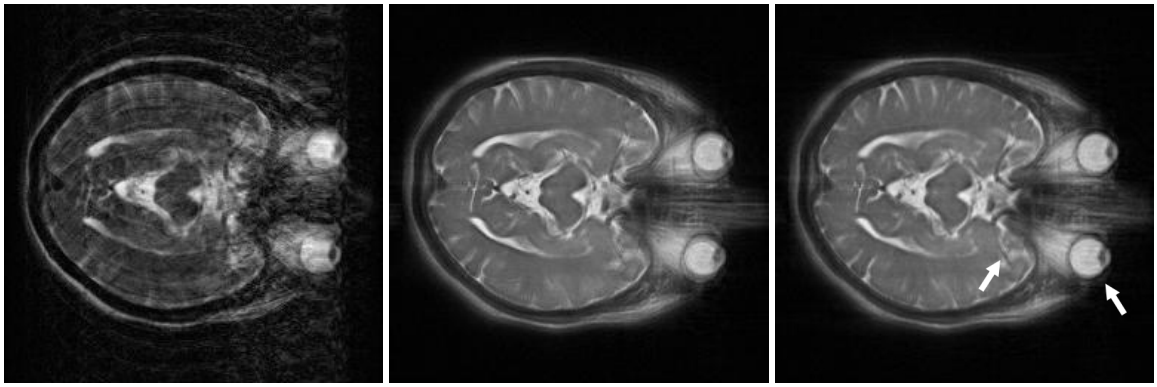

(a) (b) (c)

Figure 8.12 In vivo results. In (a) the subject was imaged with a standard interleaved FSE sequence; in (b) the same subject was imaged using TRELLIS (motion correction off); (c) shows the same as (b) except motion correction is on. Arrows show improved appearance of the middle cerebral artery and the eye.

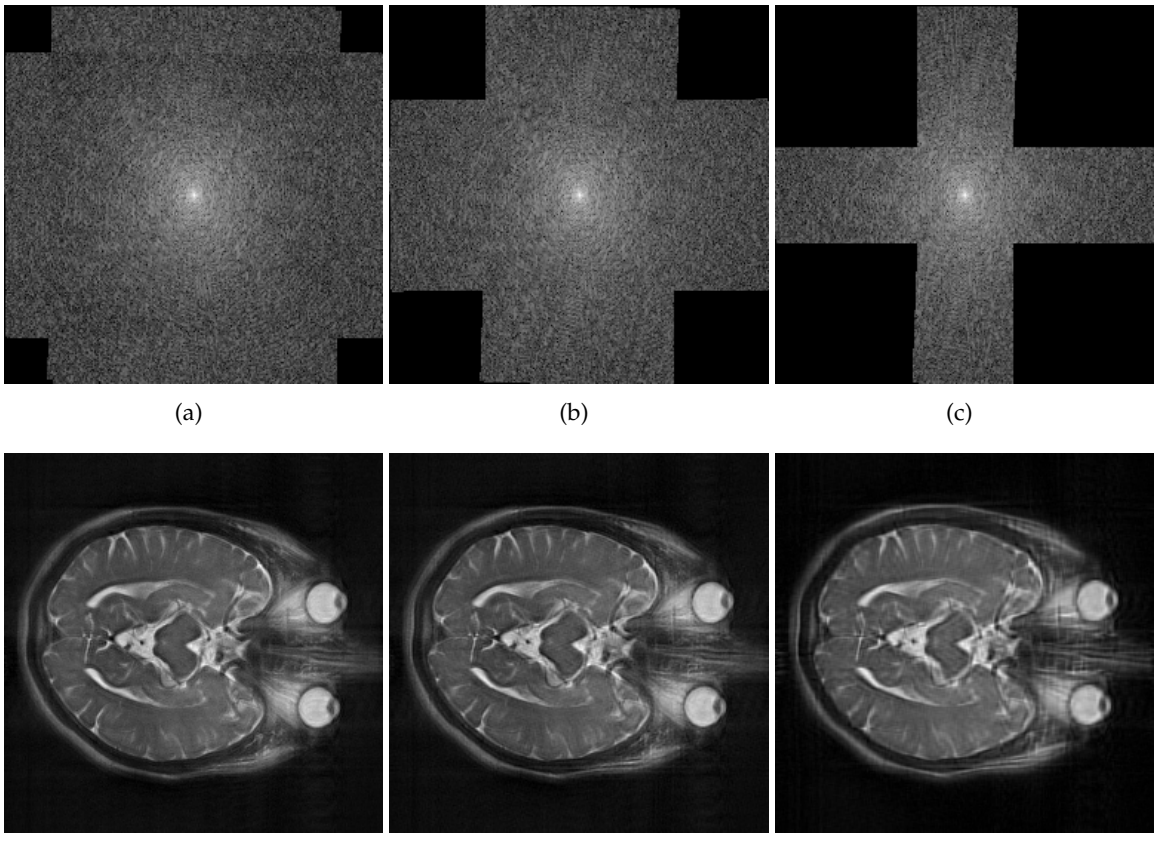

(a) (b) (c)

(d) (e) (f)

Figure 8.13 Corrected *k*-space data after applying the fast TRELLIS algorithm for three different values of N_s': 12 (a), 8 (b), and 4 (c). Reconstructed images are shown below in (d)–(f).

with a 25 % or 50 % reduction in the number of sampled strips. With a 75 % reduction in the number of strips ($N_s' = 4$, in this case), however, blurring is evident in the image. The optimal choice for N_s' is probably 8, again requiring half the acquisition time of the standard TRELLIS sequence.

8.3.3 Computational requirements

The motion estimation and image reconstruction stage of the TRELLIS algorithm was implemented using MATLAB® on a desktop PC with a 2.8 GHz Pentium 4 processor and 2 GB of RAM. When applied to TRELLIS data with **H** and **V** of size 256×256 pixels and $N_s = 16$, the time taken for each stage of the algorithm is as follows.

Task	Time (s)
Alignment of **H** and **V**	2.46
T_2 correction	1.31
Rotation estimation	41.89
Rotation correction	11.61
Translation estimation	6.74
Translation correction	2.13
Image reconstruction	0.96
TOTAL	67.10

Table 8.1 The execution time of various stages of the TRELLIS algorithm.

Although only useful as a rough guide, the data in Table 8.1 indicates that the estimation of rotation parameters is by far the most computationally expensive stage of the TRELLIS algorithm. Nevertheless, the overall time required (67 s) is reasonable. Some steps have been taken to optimise the algorithm for speed, namely, the use of polar coordinates for rotation estimation and the direct implementation of the T_2 correction algorithm. Most code, however, has not been written with computational efficiency as the highest priority. If converted to optimised C code, the author expects the TRELLIS reconstruction algorithm would execute in only a few seconds for the example data tested here. Computational requirements are therefore not a limiting factor in the performance of TRELLIS.

8.4 Discussion

TRELLIS has been successfully implemented using FSE. Alternatives exist, however, including EPI (although the author's attempts using this were unsuccessful) and GRASE (gradient- and spin-echo), first proposed by Oshio and Feinberg [135]. GRASE has been

successfully applied to PROPELLER [68] with reduced scan time over the conventional FSE-based implementation.

The TRELLIS algorithm is effective at reducing motion artifacts for both a moving phantom and a human subject, in agreement with simulations. It could be assumed that data in the outer part of *k*-space are not useful for motion detection due to poor SNR. Examination of TRELLIS results, however, has shown this not to be the case. Although motion estimates from these areas are noticeably less reliable than those obtained by using data from the centre of *k*-space, these estimates are still useful, particularly for rotation detection. This can probably be explained by the fact that a small rotation produces a significant displacement of data in the outer regions, while the change may be too small to detect near the *k*-space origin.

Results from the moving phantom experiment show reasonable detection of rotation parameters. A system of synchronising the phantom motion with data acquisition has not yet been developed, so this comparison is qualitative only. Also, one important distinction between the physical phantom and a patient is the different T_1 and T_2 characteristics. In the human body the T_1 and T_2 characteristics vary continuously from region-to-region, although they are relatively homogeneous in some tissues [6]. In the phantom constructed, T_1 and T_2 each take a single value only. Care must be taken therefore in interpreting the phantom results.

It would have been interesting to image the moving phantom using PROPELLER. Unfortunately, the commercial version of PROPELLER (GE Medical Systems) can only image axial slices, whereas the moving phantom must be imaged coronally. Access to the PROPELLER source code was not available. Having seen PROPELLER images of moving patients, however, the author believes PROPELLER motion correction for the moving phantom would be at least as good as that achieved by TRELLIS.

Results shown here use an even number of strips in **H** and **V**. Using an odd number of TRELLIS strips may be advantageous to maintain the integrity of the *k*-space origin as the middle strip in **H** and **V** would then lie directly over the centre of *k*-space. The centre of *k*-space will then always be kept intact, no matter what motion occurred during imaging. Currently, 'holes' in *k*-space near the origin caused by a gap between strips after rotation correction can occasionally cause artifacts. The optimum width of each strip has yet to be found. This is a trade-off: wider strips result in more accurate motion detection, but suffer greater T_2 artifact problems, than narrower strips. Also note that TRELLIS has been demonstrated here using a square FOV but is equally applicable to a rectangular FOV: **H** and **V** do not need to contain the same number of strips.

It is interesting to note that the TRELLIS sequence is relatively robust to motion even with-

out the application of motion correction performed in post-processing. This appears to be due to the damaging modulation of *k*-space that results from motion in standard interleaved sequences. Such modulation does not apply to TRELLIS; disruptions to *k*-space are inherently more gradual. In interleaved sequences, motion artifacts manifest themselves as 'ghosts' spread across the entire image. Using a sampling scheme like TRELLIS, motion tends to result in blurring that is arguably less problematic in terms of image interpretation. The same effect has been observed with PROPELLER [60, 73]. This leads to the possibility of acquiring only the **H** data, for example, and reconstructing an image from that. Although no TRELLIS motion correction is possible, some degree of motion artifact suppression occurs. This is the subject of the next chapter.

Chapter 9

Reduced Motion Sensitivity

Results in Chapters 7 and 8 indicated that the TRELLIS acquisition *without* motion correction is relatively insensitive to motion artifacts compared to a standard acquisition. Based on this observation, a new sequence, termed an *asymmetric sequential acquisition*, is proposed [136]. This does not correct for motion, but is relatively robust to motion effects.

9.1 Introduction

Two common sources of image artifacts when acquiring data using multiple-shot FSE are motion and T_2 signal decay. Motion causes discontinuities in *k*-space leading to blurring or ghosting in the image as seen in Chapter 8. Transverse magnetization decay, characterized by the relaxation time T_2, can have a similar effect. The order of acquisition of *k*-space data affects the sensitivity of the acquisition to these effects. This chapter proposes an acquisition order that minimises these artifacts.

As mentioned earlier, a number of lines in *k*-space can be acquired by FSE in a single excitation sequence using a train of echoes. The number of echoes is known as the *echo train length* (N_{etl}). Each 90° pulse followed by N_{etl} 180° pulses is known as a *shot*. The number of shots, N_{shots}, is equal to the image size in the k_y direction, N_{ky}, divided by the echo train length, that is,

$$N_{shots} = N_{ky}/N_{etl} \ . \tag{9.1}$$

As is the case for the TRELLIS algorithm it is assumed here that the acquisition time of data within a single shot is sufficiently small that motion can be regarded as 'frozen'. Thus,

inconsistencies in *k*-space only occur between shots in the k_y (phase-encode) direction.

A lookup table (the *view table*) links echoes to lines in *k*-space. The order of acquisition of these lines is the *view order*. A common view order is an interleaved acquisition where each shot runs from the top to the bottom of *k*-space (Fig. 9.1). In the example shown, $N_{etl} = 4$, $N_{shots} = 4$ and $N_{ky} = 16$. These values are used purely for clarity in the figure; more usual values for N_{ky} are 128 or 256.

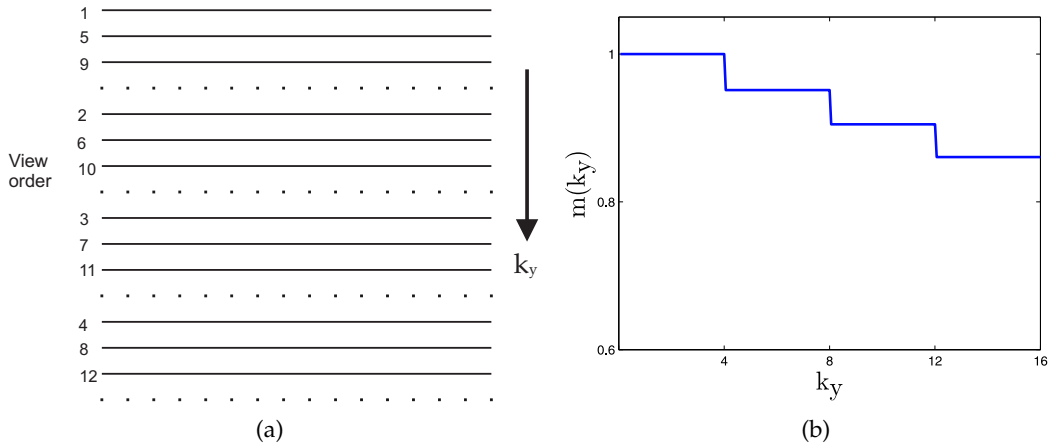

Figure 9.1 (a) An example of an interleaved acquisition in *k*-space. Data from the first three shots has been collected (solid lines) while data from the fourth shot has yet to be acquired (dotted lines). Numbering indicates the order of acquisition. The first shot comprises lines 1–4, the second shot lines 5–8, etc. (b) The resulting modulation function in the k_y direction.

Transverse magnetisation decay continues throughout the entire FSE echo train so that the signal measured for the later acquired lines is attenuated relative to the earlier lines. The measurement sensitivity in the nth acquired line can be approximated by

$$S(n) \;=\; S(0)e^{-nt_{esp}/T_2}\;, \tag{9.2}$$

where $n = 0, 1, 2, \ldots, N_{etl} - 1$, t_{esp} is the echo spacing (the time between line acquisitions) and T_2 is the transversal relaxation time of the tissue. There is thus a modulation imposed on the *k*-space data in the phase-encode direction; this is denoted as $m(k_y)$. As $N_{shots} > 1$ for all acquisitions considered here, $m(k_y)$ consists of repeated versions of $S(n)$. Its exact form, however, depends on the order in which lines are acquired.

For the view ordering given in Fig. 9.1, $m(k_y)$ is a step-like decay function as the top four lines are all acquired at the same point in the echo train, as are the next four and so on. This is shown in Fig. 9.1(b) for $t_{esp} = 5$ ms and $T_2 = 100$ ms.

9.2 Modified view orders

The view order shown in Fig. 9.1 is commonly used. Several alternatives are presented here; the first has been considered before [4], but is not normally employed for reasons explained shortly. Fig. 9.2(b)–(d) shows the three alternative view orders to be compared to that shown in Fig. 9.1. Each ordering scheme has been implemented in practice by generating a view table that is then used by the scanner to determine the view order.

The first view order, shown in Fig. 9.2(b), acquires data from the top to bottom of *k*-space in sequential strips. Each strip corresponds to a single shot comprising N_{etl} lines, acquired as illustrated in Fig. 9.2(a). The view order in Fig. 9.2(c) is the same as that in Fig. 9.2(b) except that the direction of acquisition of each strip alternates as shown. Strips are still acquired sequentially, from the top to the bottom of *k*-space. This is the order of acquisition used by TRELLIS in the results presented in Chapters 7 and 8. The final ordering system, Fig. 9.2(d), is a shifted version of Fig. 9.2(c) so that the centre of *k*-space is acquired during the middle of an echo train. The author calls this an *asymmetric sequential acquisition*. As N_{shots} is still an even number, the top-most strip must be split as shown. This means that the very top and bottom of *k*-space is filled in the first shot, but then acquisition is from top to bottom as previously described.

In Fig. 9.3(a)–(h) the imposed *k*-space modulations and the corresponding point spread functions (PSFs) that result from the different view ordering schemes are compared. Again, the parameters used were t_{esp} = 5 ms and T_2 = 100 ms, but this time with $N_{ky} = 256$, $N_{etl} = 32$ and, as required by Eq. (9.1), $N_{shots} = 8$. The PSF, denoted $h(y)$, directly affects the final image quality, as the measured *k*-space data is equal to the ideal data multiplied by $m(k_y)$. In image-space this is equivalent to a convolution of the ideal image with $h(y)$, as shown in Eq. (3.1).

Note that blurring and ghosting in the image is best indicated by the real part of the point spread function. This has been observed before [137].

9.3 Results and discussion

For simulation purposes, the Shepp-Logan head phantom has been used once more. Data is modulated in *k*-space and an image reconstructed. These reconstructions are compared in Fig. 9.3(i)–(l), and each corresponds to the view order and PSF directly above the figure.

The use of an interleaved view order for multiple-shot FSE is prevalent as, in the absence of motion, image quality is good (Fig. 9.3(i)). The first sequential acquisition method presented produces images of unacceptable quality due to T_2 artifacts (Fig. 9.3(j)). The reason

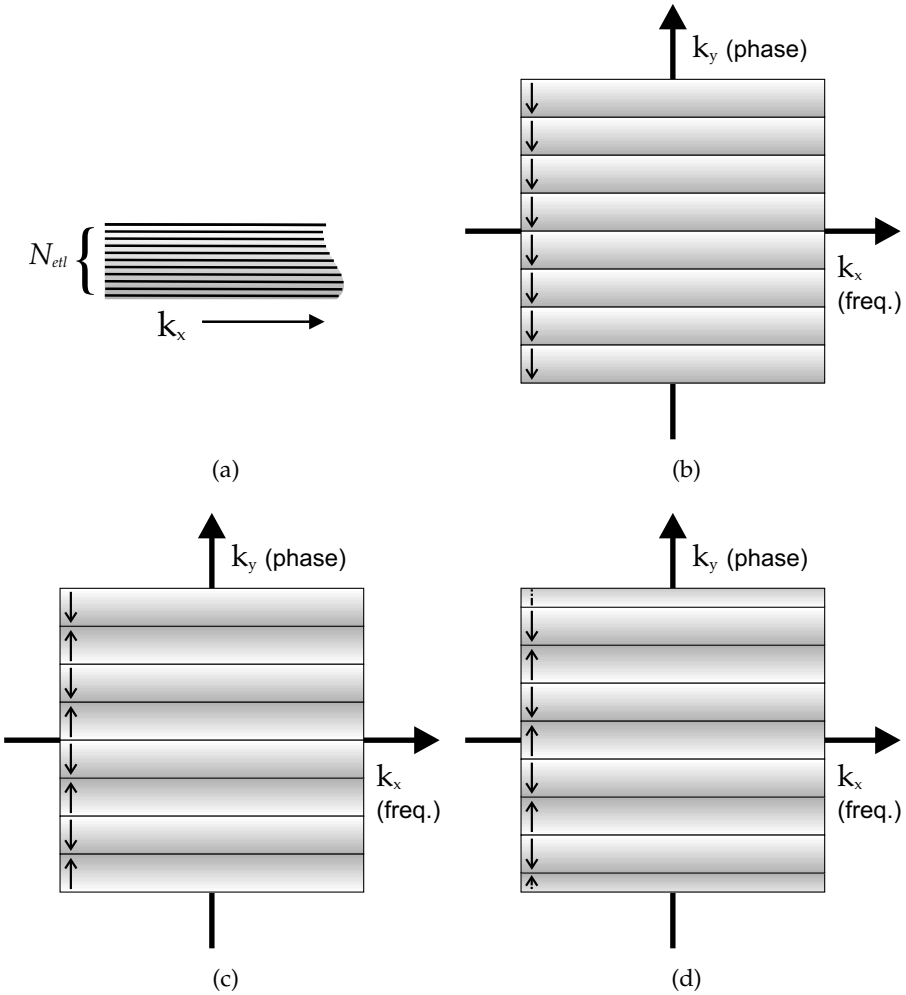

Figure 9.2 A strip of data can be acquired rapidly in *k*-space using FSE. Each strip is composed of N_{etl} lines as shown in (a), corresponding to the echo train length used. The three proposed view orders (b)–(d) use such strips.

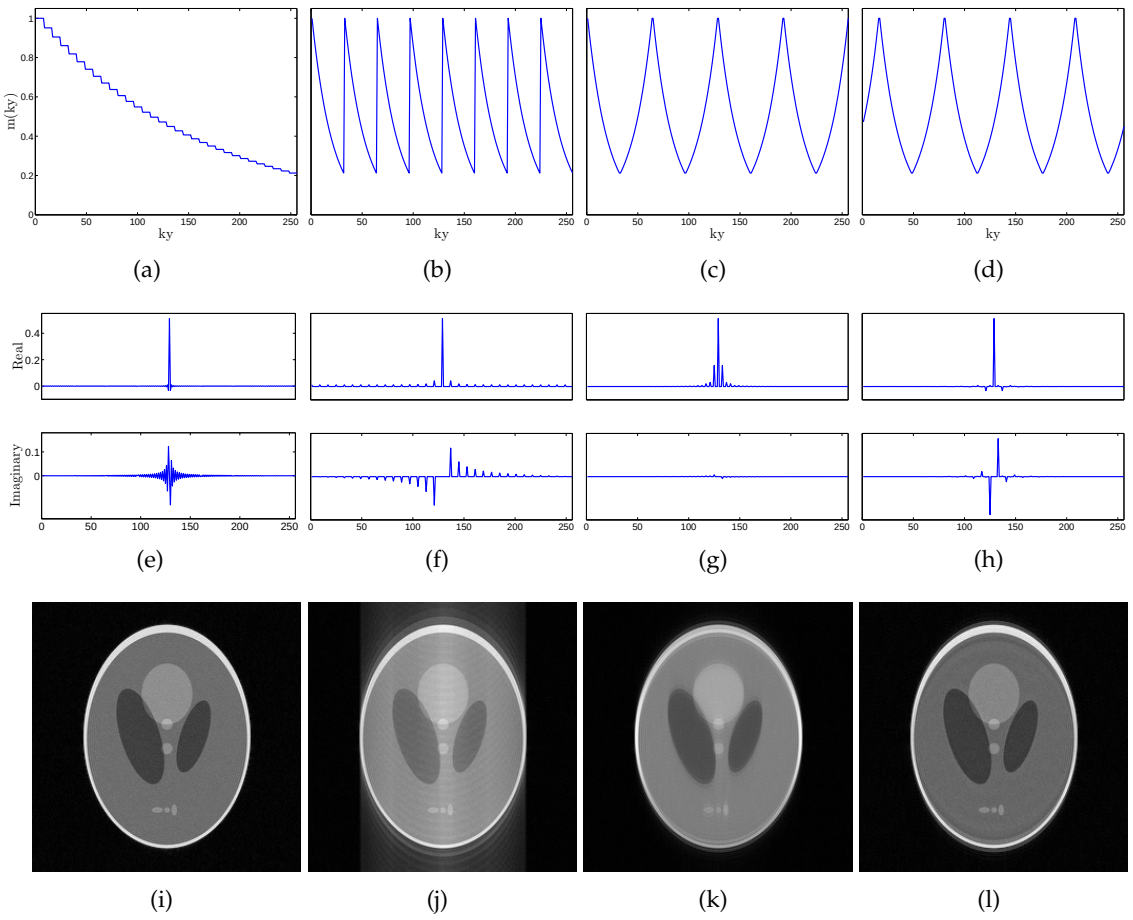

Figure 9.3 Four different view orders: (a) is commonly used; (b) is not often used due to T_2 artifact problems; (c) and (d) are proposed here. Note that (b), (c) and (d) correspond to the respective view orders shown in Fig. 9.2. The four resulting point spread functions are shown in (e)–(h), and the effect on reconstructions of the Shepp-Logan head phantom is shown in (i)–(l).

is the sharp discontinuities in $m(k_y)$, apparent in Fig. 9.3(b), which manifest themselves as widely spread oscillations in the PSF and thus generate ghosts in the image.

The next alternative ordering scheme proposed here, that is, sequential strips with alternating phase-encode direction, Fig. 9.2(c), significantly improves the situation through reduction of discontinuities in $m(k_y)$. The real part of the new point spread function does, however, have significant energy close to the origin; this leads to the blurring of the image seen in Fig. 9.3(k).

The asymmetric sequential view order shown in Fig. 9.2(d) improves the situation further as is apparent from Fig. 9.3(h) and (l). The author proposes that this is due to the inherent 'averaging effect' the Fourier transform has on Hermitian points in *k*-space. This provides a first order correction for $m(k_y)$.

The view order shown in Fig. 9.2(d) exhibits T_2 artifacts that are only slightly worse than those in the interleaved order. It is markedly superior, however, in terms of robustness to motion. This is illustrated in Fig. 9.4. The simulated motion is a clockwise rotation (from 0 to 7° in 1° increments) and a translation (from 0 to 7 pixels in the positive x-direction in 1 pixel increments and from 0 to 3.5 pixels in the positive y-direction in 0.5 pixel increments). As seen in Fig. 9.4(a), image quality is poor if an interleaved view order is used. Using the asymmetric sequential ordering, however, motion manifests itself as a more tolerable blurring.

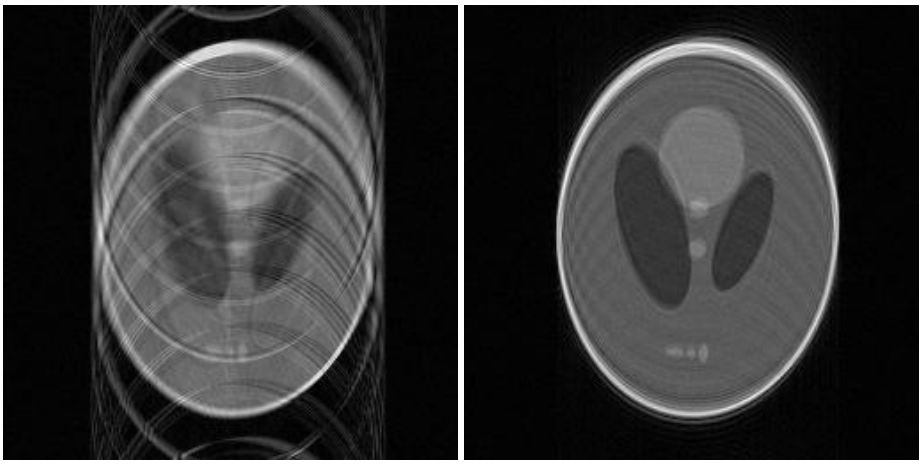

(a) (b)

Figure 9.4 Comparison of interleaved FSE and the proposed asymmetric sequential method shown in Fig. 9.2(d) under motion, including both rotation and translation.

Not all motion in MRI is rigid-body motion. The Shepp-Logan phantom motion simulation was modified as shown in Fig. 9.5(a)–(b) so that one of the Shepp-Logan ellipses moved during the scan (14 pixels total, in increments of 2 pixels per shot) rather than the entire

phantom. The results are shown in Fig. 9.5(c)–(d). They indicate that the proposed view ordering technique is superior to the standard interleaved acquisition for deformable motion as well as for rigid-body motion. In Fig. 9.5(d) the position of the moving ellipse in the reconstructed phantom is its position at the time the central strip in *k*-space was acquired.

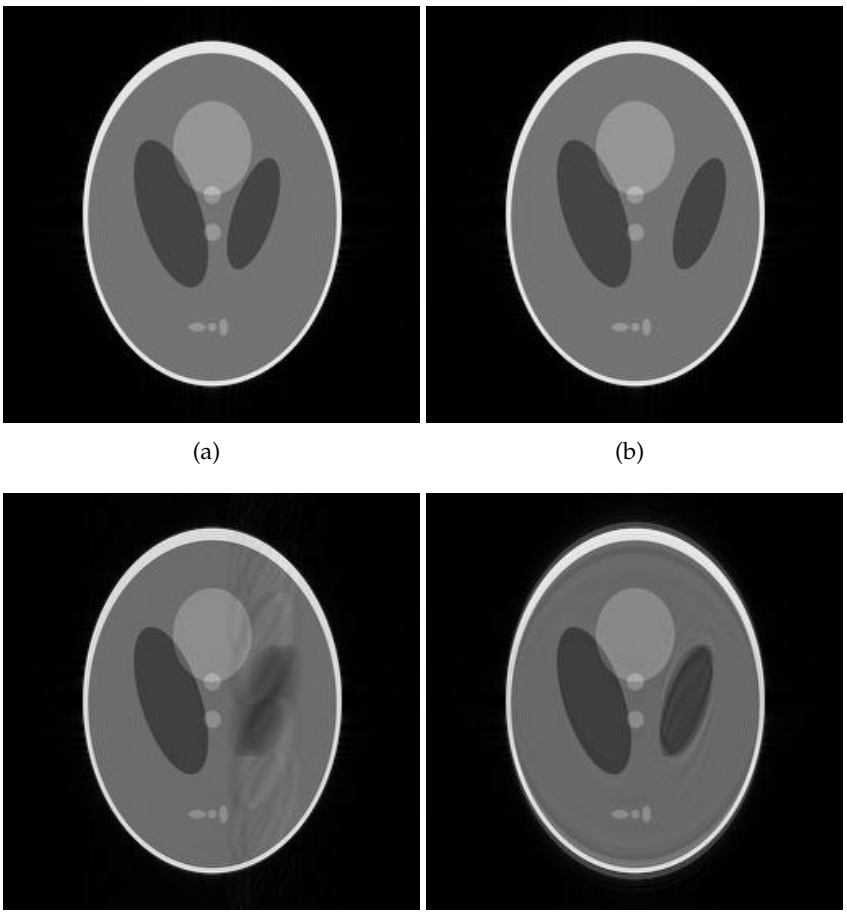

(a) (b)

(c) (d)

Figure 9.5 (a) The Shepp-Logan head phantom with an SNR of 25 dB. (b) To simulate motion other than rigid-body motion, a single ellipse is moved inside the phantom as shown. This is done in increments of 2 pixels between every shot acquired in *k*-space. (c) An image reconstructed using interleaved FSE under this motion. (d) An image reconstructed using the proposed asymmetric sequential method under the same motion.

It may also be possible to demodulate *k*-space to remove the effects of $m(k_y)$. This is not entirely straightforward, however, as T_2 values are not normally known in advance. Also, the expression in Eq. (9.2) only approximates the real situation. In practice, T_2 varies between different tissue types. This approximation does little to change the results shown here; however, it adds complexity to the process of estimating $m(k_y)$ in order to attempt any demodulation.

As well as the simulations presented above, sequences have been implemented on a 1.5 T

Signa Excite HDx scanner (GE Medical Systems) using a modified FSE sequence with matrix size 256×256. Echo train lengths of both 16 and 32 were used successfully. An example using $N_{etl} = 32$ is shown in Fig. 9.6. Results are consistent with simulations and show a significant reduction in ghosting when using the proposed asymmetric sequential sequence to image a moving object. Some T_2 blurring, however, is present both with and without motion. DBE values for images in Fig. 9.6(b), (c) and (d) are 1.5×10^{-3}, 2.0×10^{-2} and 5.0×10^{-3}, respectively, when using the image in Fig. 9.6(a) as a reference. These values confirm the order of image quality that is already apparent to the eye and quantify the level of artifacts.

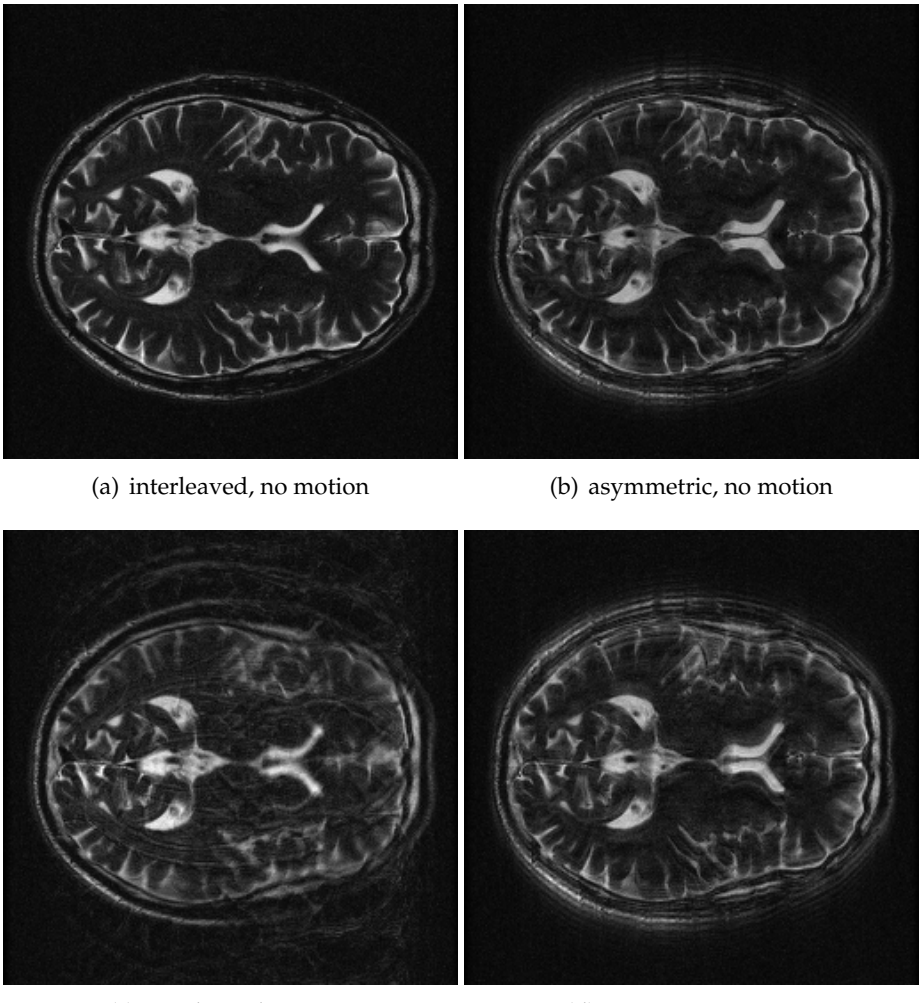

(a) interleaved, no motion (b) asymmetric, no motion

(c) interleaved, motion (d) asymmetric, motion

Figure 9.6 An in vivo comparison between the interleaved FSE sequence (images (a) and (c)) and the proposed asymmetric sequential sequence (images (b) and (d)). The subject was instructed to stay still in (a) and (b) and move slightly throughout the scan in (c) and (d).

The only problem observed when implementing the asymmetric sequential acquisition in practice was a lack of flexibility over the effective echo time, TE_{eff}. The TE_{eff} affects image contrast and is determined by which echo in the echo train acquires the centre of *k*-space (the centre of *k*-space provides most contrast information). Using the standard interleaved

sequence, acquisition does not necessarily need to begin at the top of *k*-space; rather, it can be shifted depending on the desired TE_{eff}. This is not possible with the asymmetric sequential view order as, under a large shift, it will reduce to the view ordering shown in Fig. 9.2(c) and will suffer from T_2 induced blurring. Clinically, this may be a limitation in some cases.

9.4 Conclusions

Fast spin echo imaging in MRI is sensitive to motion and T_2 artifacts. Modifying the view order changes the sensitivity of the technique to these effects. A standard interleaved sequence produces good quality images in the absence of motion. The asymmetric sequential acquisition shown here, however, offers a significant advantage in the presence of either or both rigid-body and deformable motion. Disadvantages of the technique include increased artifacts from T_2 effects and a lack of flexibility in setting the effective echo time.

Chapter 10

Conclusions and Future Work

This chapter summarises the main contributions made by this thesis and draws conclusions from the research performed. Recommendations are then made concerning future work in the area.

10.1 Thesis summary and conclusions

This thesis aims to answer one particular question in the field of motion correction in MRI, namely, 'is it possible to develop a motion correction system that requires no external hardware and uses all collected data for both image reconstruction and the estimation of motion parameters?'. The development of TRELLIS answers this question. Examination of TRELLIS results shows that data in the outer part of *k*-space is still useful for motion estimation, despite poor SNR. Strips in these regions can therefore be motion corrected and thus contribute to the final image.

The TRELLIS algorithm is unique in that it acquires data in a series of overlapping strips, and then forms and solves a system of equations linking all motion estimation information together. Unlike existing techniques such as PROPELLER, all collected data is used for both motion detection and image reconstruction and excessive oversampling of the centre of *k*-space is avoided. It is likely, however, that this advantage is gained at a cost of decreased motion detection accuracy compared to PROPELLER. Nevertheless, the accuracy of the TRELLIS algorithm is sufficient to enable accurate motion estimation in simulations and it has proved effective at reducing motion artifacts for both a moving phantom and human subjects.

The sampling of *k*-space in TRELLIS is uniform which effectively achieves a $\sqrt{2}$ improvement in SNR everywhere. This means that the integrity of high spatial frequencies is more

likely to be preserved (and result in better detail in the image) when compared to PROPELLER, which samples the centre of *k*-space much more densely than the outer regions. The fast TRELLIS algorithm trades this advantage for a 50 % reduction in acquisition time. This may be a worthwhile trade-off in most cases. This gives fast TRELLIS an acquisition time equal to that of a standard FSE sequence (with an equivalent echo train length) and therefore less than that required by the original implementation of PROPELLER.

A means of simulating motion has been developed using the analytical Shepp-Logan head phantom and a physical Shepp-Logan phantom has been built to confirm that these simulations are reasonable. To the knowledge of the author, this is the first time that an MR-phantom closely resembling the simulated Shepp-Logan head phantom has been constructed. It has the potential to produce a number of interesting results. To test the effect of motion, a MR-safe platform has been constructed capable of moving a phantom in a reproducible manner. The DBE metric has also been developed and tested and has been valuable for optimising the TRELLIS algorithm.

Several practical problems have been solved in the implementation of TRELLIS: a means of correcting T_2 blurring artifacts has been developed; the phase-correlation method has been extended to provide sub-pixel displacement information; and, using this, a means of aligning *k*-space data accurately has been demonstrated. These developments could be applied to algorithms other than TRELLIS.

As well as the TRELLIS algorithm, two other data acquisition techniques are proposed in this thesis. The first is the asymmetric sequential acquisition in Chapter 9. This is very motion tolerant while resulting in images with fewer T_2 artifacts than a standard sequential acquisition using FSE. Finally, the experiment undertaken by the author to correct motion using parallel imaging (Appendix A) shows promising results. The possibility of developing this into a convenient and robust motion correction technique has been demonstrated. A key advantage of this technique is that a standard reconstruction and a motion-corrected reconstruction can be generated from the same acquired data.

10.2 Suggested future work

As well as the development of TRELLIS, this thesis has introduced systems to test motion correction algorithms. Given ample time on an MRI scanner, there are now a number of experiments that could be performed based on this development work. These include more thorough testing of TRELLIS using the moving phantom with different amounts of translation and rotation, and modifying the various TRELLIS parameters. Ideally these experiments should be performed simultaneously with optical tracking of the phantom.

The study shown in Appendix B could be repeated with subjects more prone to motion than the healthy volunteers tested. This data could be applied to constrain the motion estimates in TRELLIS. Incorporating prior knowledge of the maximum possible values of velocity or acceleration, for example, would further improve results. This was demonstrated to some extent in Section 7.4.

The use of information from all slices in an acquired data set could greatly improve the robustness of the algorithm. As neighbouring slices are affected by motion with similar parameters, combining this motion information when correcting a single slice could be beneficial. It is anticipated that this extra information would be best included before solving the system of equations for rotation and translation. Instead of a single measurement of rotation between two strips, several measurements could be obtained. These could be averaged prior to solving the system of equations and the inverse variance between measurements used as a weighting function. A similar approach could be applied to PROPELLER.

The FSE implementation of TRELLIS described here incorporates T_2 correction. Slight artifacts caused by T_2 decay remain, however. Application of the work on short axis PROPELLER by Skare et al. [69] (discussed in Section 8.1.2) could possibly solve this problem. Artifacts caused by fat/water chemical shift effects could probably be reduced by using high-bandwidth sequences: this is worth investigating.

This focus of this thesis has been on the initial development of TRELLIS rather than its optimisation for clinical use or comparisons of TRELLIS to other techniques. These are major areas that require further study. A thorough theoretical investigation on the effect on image resolution and spectral SNR of the relative sampling patterns methods used by TRELLIS and PROPELLER is required. Work by Newbould et al. [80] is recommended as a good starting point.

The author is often asked whether TRELLIS could be applied to imaging in three dimensions. Unfortunately, the concept of implementing the current version of TRELLIS using solid 'rods' in three-dimensional space, rather than strips in two dimensions, is not very practical. The key principle of 'no motion within a strip' (or within a rod in this case) would be violated if the rod was a useful size. The general concept, however, of estimating relative motion parameters between segments of collected data, and then combining this information using a linear system of equations, could perhaps be applied to three dimensions. It would be interesting to examine this possibility more closely.

The DBE metric could be developed further. It would be worthwhile deriving a theoretical justification for performance of the metric to strengthen the qualitative explanation given here. As seen in this thesis, the DBE metric has some useful properties. It would be interesting, however, to see if it can be extended to remove its reliance on a reference image.

Given knowledge of the SNR it would be possible to calculate how much energy *should* lie out the support region and to compare this to the measured amount. A metric that could quantify artifact levels in an MR image without a reference image would be valuable.

The asymmetrical sequential sequence needs to be investigated further. If techniques to further reduce T_2 effects could be applied to it, then it may be worthwhile comparing it to other motion-resistant sequences such as spiral imaging. Similarly, the author has shown that motion correction using parallel imaging is both desirable and possible. Little has been done, however, to progress this idea beyond its original concept. This is a major area that could be examined in more detail.

Appendix A

Motion Correction using Parallel Imaging

Parallel image reconstruction techniques are a relatively recent innovation in MRI and are used mainly to reduce acquisition time. The author has, however, briefly experimented with the application of parallel imaging to motion correction. Results are given here. This work is attached as an appendix as it does not constitute a chapter in its own right; rather, it is a single brief experiment that demonstrates the merit of further work in this area.

A.1 Background

In general, 'parallel imaging' describes the use of multiple receive coils to obtain extra spatial information. This can reduce the number of phase-encode steps required to form an image. The extra spatial information is obtained through knowledge of the spatially-varying sensitivity of each individual coil, often referred to as a *coil sensitivity map*.

The first practical implementation of parallel imaging was in 1997 by Sodickson et al. [138] using their technique known as SMASH (simultaneous acquisition of spatial harmonics). SMASH estimates unsampled k-space lines based on adjacent sampled lines and knowledge of the coil sensitivity function. In 1999, a technique named SENSE (sensitivity encoding) was introduced by Pruessmann et al. [139]. Unlike SMASH, SENSE operates directly in the image domain.

Parallel imaging has been applied to motion correction before. In 2002, Bydder et al. [140] proposed a technique that generates multiple copies of k-space using SENSE, compares these copies, discards suspect data, and rejects lines that are found to have been corrupted.

A final version of *k*-space is then generated using SMASH to estimate data in discarded lines, and an image reconstructed. This technique has the disadvantage that data is being discarded, hence there is a SNR loss if motion occurs. Also, in cases of severe or continuous motion, there may not be enough uncorrupted data to form an artifact-free image.

An optimisation technique has been presented by Atkinson et al. [94] that iteratively modifies estimates of the coil sensitivity maps to reduce artifacts in the final image. This is achieved using a nonlinear least-squares optimisation process. Results are promising although the algorithm is very computationally intensive, which may be a limitation.

Parallel imaging has also been used in conjunction with other motion-estimating techniques. Bammer et al. [141, 53] have used SENSE to synthesise missing data after motion estimation and correction using navigator echoes. Another method, reported by Chen et al. [142], used a recent parallel imaging technique known as GRAPPA (generalized autocalibrating partially parallel acquisitions) [143] for motion correction. GRAPPA was applied to rapidly obtain individual images. Imaging was done on a phantom that was manually shifted between each scan, meaning motion was not continuous. Another limitation was the repeated sampling of the centre of *k*-space that was required for motion estimation. This reduces the technique to that of a simple navigator echo system and increases acquisition time over a standard scan.

Here the author proposes a technique that, along the theme of this thesis, uses all collected data for image reconstruction and motion correction. Motion-corrupted data is not discarded, but instead corrected. Navigator echoes as such are not used: the technique is 'self-navigated'.

A.2 Method

The method used is illustrated in Fig. A.1. Data were collected using an 8-channel head coil and a modified FSE sequence with $N_{etl} = 32$. The number of lines acquired in the PE direction was chosen to be 128; therefore, 4 shots were required to fill *k*-space. The image resolution in FE direction was 256; this does not significantly affect imaging time so the extra resolution comes at little cost.

Images were reconstructed using two different techniques: directly from the full *k*-space data set, and using the parallel motion correction technique proposed here. This reconstructs four images independently: one from each shot of acquired data. As the acquisition time of a single shot is very rapid, the amount of motion occurring within this interval is assumed to be minimal.

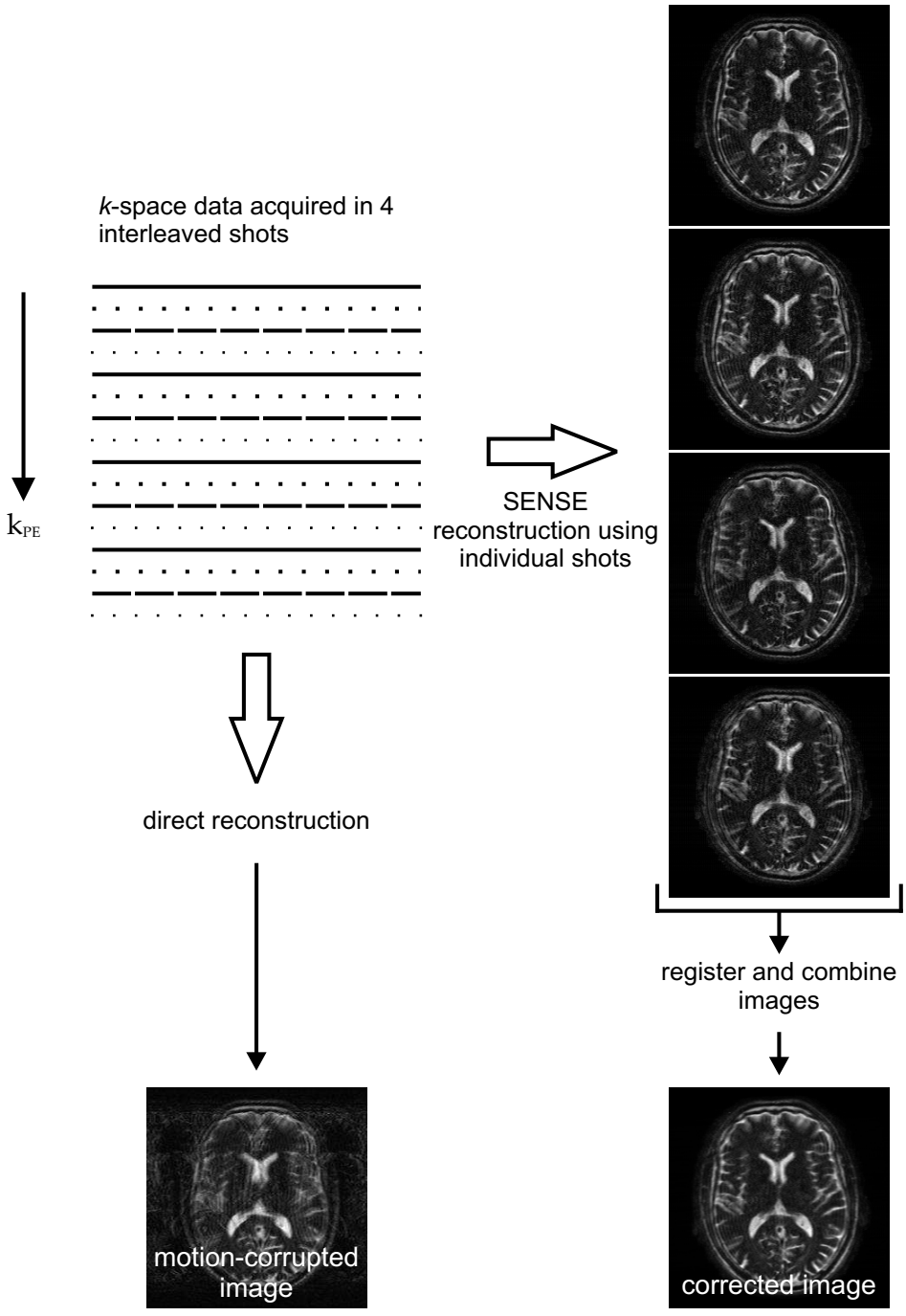

Figure A.1 The motion correction technique using SENSE tested here. Actual *k*-space dimensions used were 128 (PE direction) and 256 (FE direction) with $N_{etl} = 32$. Two different reconstructions were produced from each data set as shown.

The parallel reconstruction method used is SENSE, incorporating the support constraint of the object to improve the SNR in the reconstructed image as described by Pruessmann et al. [139]. The SENSE implementation used here was that written by Bing Wu at the University of Canterbury; Bing's expertise in parallel imaging reconstruction methods have been essential to this work.

To reconstruct an image free of aliasing, SENSE requires coil sensitivity maps for each coil. These were estimated using a low-resolution 32×32 image, acquired when the patient was stationary. This was same data set used to obtain knowledge of the support region of the object. This data set is small enough to be acquired in a single shot, reducing any problems caused by motion. As the coil sensitivity profiles for each coil are fairly smooth, a polynomial function was fitted to each sensitivity map allowing extrapolation of the map slightly beyond the boundaries of the object. This is necessary as, with motion, part of the patient may move outside the region over which the coil sensitivity map is directly estimated.

Image registration of the four images was performed using MATLAB® code written by the author. Techniques similar to those used in TRELLIS were applied. Rotation estimation was performed in the Fourier domain using the *k*-space magnitude (in polar coordinates). An angular search increment of 0.1° was used. Rotation correction was then performed in image-space by rotating the coordinate system and regridding using bilinear interpolation. Translation estimation was performed using the phase correlation method. A phase ramp was added in *k*-space to correct for any translation errors found. Finally, the four images were combined in the image-domain by taking the sum of their magnitudes. The execution time of the algorithm was less than 10 seconds for a single slice.

A.3 Results and discussion

Only a single study has been carried out to date. Imaging was performed on a normal volunteer. The subject was told to move different amounts during each of three scans: first, to stay as still as possible; second, to move slightly once; and third, to move more continuously. The resulting images, reconstructed from one slice, are shown in Fig. A.2. Gibbs ringing is evident in the PE direction (horizontal) in all images shown. This is due to zero-padding in *k*-space, performed to make the images square to simplify image registration.

The maximum motion detected between any two of the four images reconstructed from the first scan (no motion) was 0° rotation, 0.02 pixels in the x-direction and 0.01 pixels in the y-direction. For the second scan (slight motion), these figures rose to 2.6°, 3.21 pixels (x-direction) and 0.65 pixels (y-direction). In the third scan (continuous motion), maximum detected motion was 3.9°, 5.49 pixels (x-direction) and 1.00 pixels (y-direction).

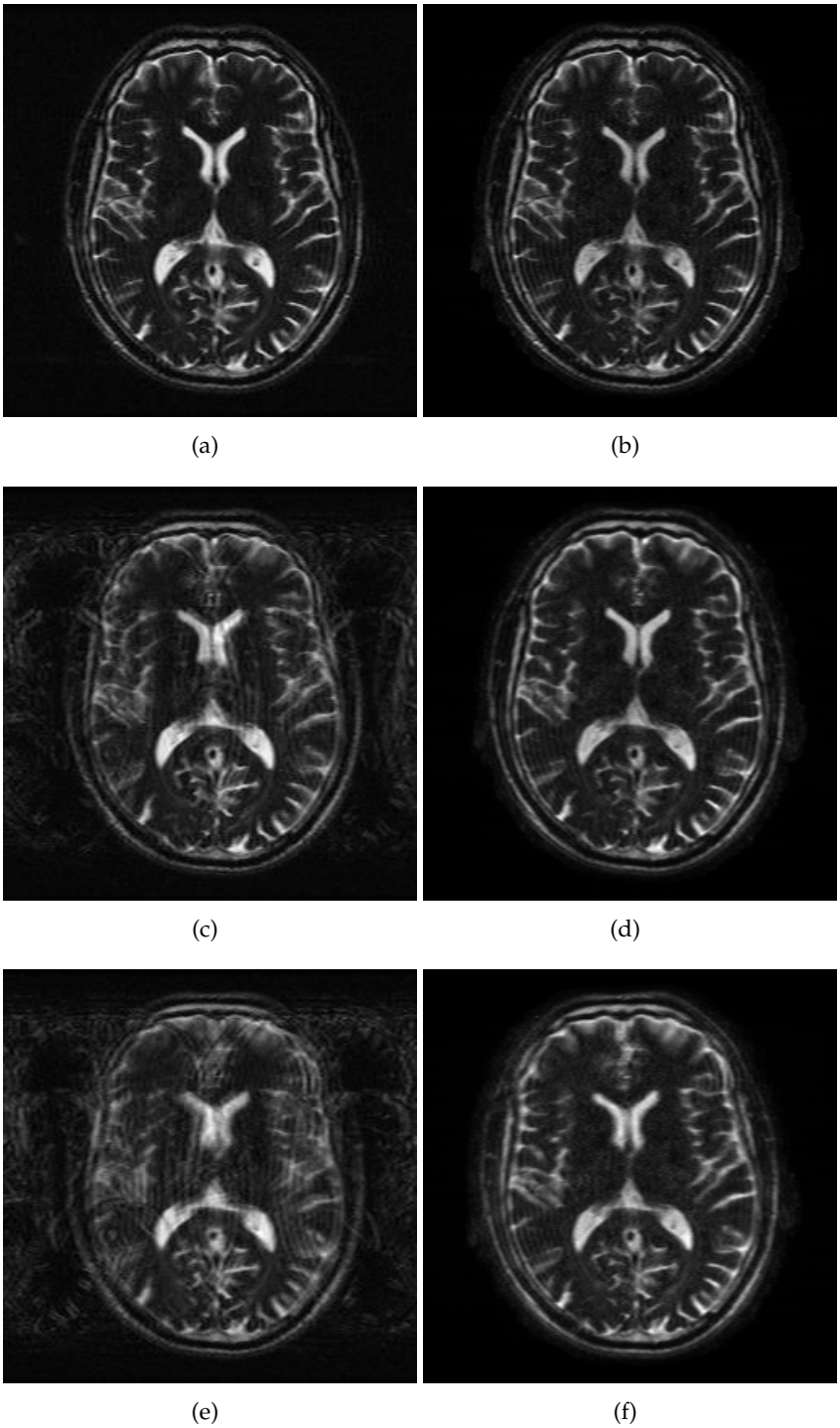

(a) (b)

(c) (d)

(e) (f)

Figure A.2 In vivo experimental results for no motion, (a) and (b), slight motion, (c) and (d), and more significant motion, (e) and (f). Images (a), (c) and (e) are reconstructed by inverse Fourier transform of the full k-space data set. Images (b), (d) and (f) are reconstructed from the same data as (a), (c) and (e), respectively, but the parallel reconstruction and image registration scheme described is used.

An SNR drop is noticeable when using the parallel reconstruction technique rather than the direct reconstruction. It is difficult to quantify this as the background in Fig. A.2(b) has effectively been masked by the application of the support constraint in the reconstruction: the SNR can therefore not be computed from the background noise. In some respects the reduced SNR is inherent to SENSE, and is related to factors such as the coil geometry, as described in [139]. The author suggests, however, that the drop in SNR in this case is also due to errors in the coil sensitivity map. Small errors in the map are expected to result in larger errors in the final image as reconstruction involves a matrix inversion.

An advantage of the approach demonstrated here is that motion correction reduces to the problem of registering a number of images. This is straightforward compared to the complexity of TRELLIS or PROPELLER as far as image reconstruction is concerned. A further advantage is that corrected data can be combined in the image domain meaning no interpolation of *k*-space is required. Another important strength of the technique is the ability to generate two images from the same collected data. The first of these is essentially a standard interleaved FSE scan; the second is motion corrected. This gives the end user a choice: the image acquired using the standard sequence would be the preferred option if no motion occurred, as it would achieve a better SNR.

Only an 8-channel head coil was available for this experiment. If a 16-channel or 32-channel coil could be used, it might be possible to extend the FOV up to a full 256×256 resolution (rather than zero-padding), making the images of much greater clinical utility.

In conclusion, the results shown here are very promising. The author strongly recommends that this approach be investigated further.

Appendix B

Motion Quantification Experiment

To develop and test algorithms for motion estimation and correction in MRI, it is useful to know as much as possible about the nature of the motion likely to occur during scanning. Quantifying head motion in MRI is a little-researched area, so the author carried out a simple experiment to obtain some preliminary data on normal subjects and to determine the merits of future work in this area.

B.1 Previous work

In a study by Atkins and Menke [144], head motion was measured during positron emission tomography (PET) scans. Two fixed cameras recorded the position of infrared reflectors attached to a mouthpiece and a custom-made tooth splint, held in the patient's mouth. Motion information was obtained in three dimensions over 10 min and 30 min scans. Patient motion of up to 10 mm was observed (the measurement accuracy of this system is claimed to be around 0.2 mm). Although PET and MRI are completely different imaging modalities, the patient, lying supine, must hold their head still for a substantial period of time in both. Thus, these results may be applicable to MRI.

Seto et al. [145] used a Polaris tracking system (Northern Digital Inc., Ontario, Canada) to quantify subject head motion in a simulated fMRI scan. Eight stroke subjects were recruited for this experiment. Although selection criteria included the ability to stay reasonably still, the stroke subjects exhibited approximately twice the head motion of age-matched controls and moved by around 2 mm during a simulated fMRI task.

B.2 Tracking device

The tracking system used in the study reported here was developed at the University of Canterbury by Porer [146], but is unrelated to this thesis work.

A three-dimensional marker (Fig. B.1) is attached to the head and is monitored using a simple webcam at a distance of 1 m. The marker consists of black and white components to achieve maximum contrast. It includes a sphere of known diameter (19 mm); this is used to determine the relationship between pixels in the image and the physical size of the object. A sphere is used because its appearance is unaffected by the angle at which it is viewed. The white octagon shown in Fig. B.1 is used to determine rotation parameters in the x-y plane.

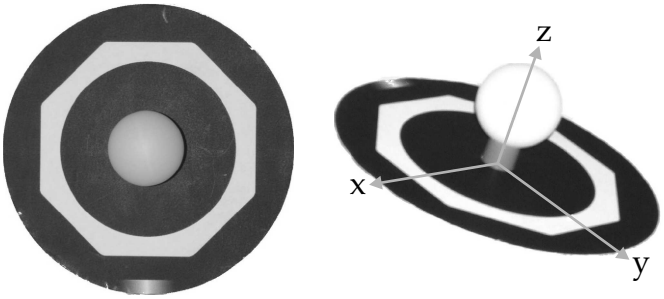

Figure B.1 The marker shown from the top (left) and from an angle (right). The diameter of the sphere is 19 mm. Images are modified from [146].

The system produces five parameters which quantify five components of rigid-body motion: translation in the x- and y-directions and rotation about the x-, y-, and z-axis. The sixth parameter, translation in the z-direction, can not be accurately obtained using the system; z-direction translation corresponds to movement away from the camera. The system has been shown to be accurate to within 0.1 mm [146] for translation and 0.06° for rotation. The camera currently used limits the frame rate to 15 frames/s (sufficient for the experiment described here).

B.3 Experiment description

The aim of this experiment was to determine whether the system described above is suitable for quantifying patient motion in MRI and to identify the range of in-plane motion likely for healthy subjects.

Four volunteers aged between 25 and 33 were told to lie in a supine position on a horizontal table and place their head on a cushion similar to that normally used in an MR scanner. The marker shown in Fig. B.1 was attached to the head of each subject using elastic strap. Subjects were instructed to keep their head as motionless as possible for 10 minutes, as if

they were having a real scan.

The position of the marker was tracked over the 10 minute period using the system described.

B.4 Results and discussion

When imaging axially, in-plane rotation corresponds to rotation around the z-axis. This was measured and the resulting relative angular position of the marker, $\delta\theta$, for each subject is shown in Fig. B.2. The position is relative to the mean angular position around the z-axis of the marker over the duration of the experiment.

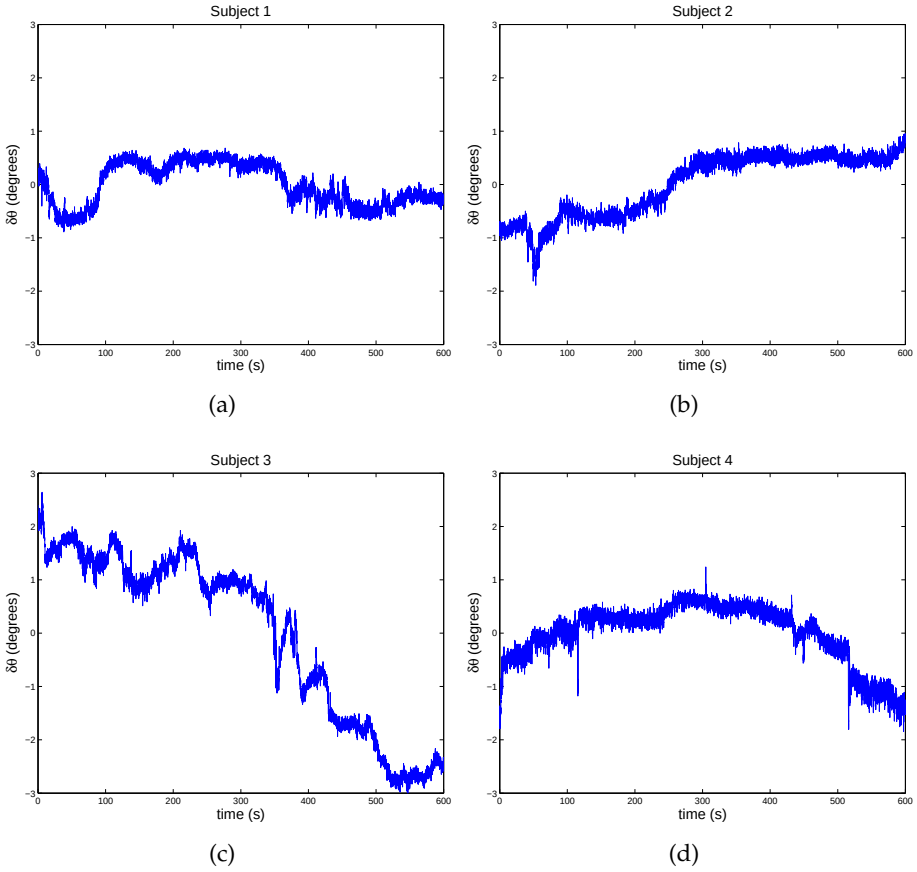

Figure B.2 The in-plane rotation of the marker attached to the head of each subject.

The rotation range for each subject during the experiment was 1.6°, 2.8°, 5.6° and 3.1° for subjects 1–4, respectively. This was greater than expected by the author. The angle measured, however, generally varies slowly over time. Thus, the angular difference in the position of the marker between two points close together in time is relatively low. The

spikes in Fig. B.2(d) are an exception to this, and are thought to be caused by involuntary swallowing of the subject, perhaps due to the elastic strap under his chin holding the marker in place. This swallowing produces a movement of the jaw which, in turn, causes a movement of the marker that is much greater than the corresponding motion of the skull. The author suggests, therefore, that these spikes can be ignored.

Measurements of relative translation in the x-direction, δx, (corresponding to motion in a horizontal direction) are shown in Fig. B.3. The range of translation for each subject during the experiment was 3.3 mm, 5.8 mm, 13.4 mm and 5.4 mm for subjects 1–4, respectively. The spikes in Fig. B.2(d) are much less apparent in Fig. B.3(d). This is unsurprising: jaw motion in a subject lying in the supine position does not cause any visible x-direction translation of the marker.

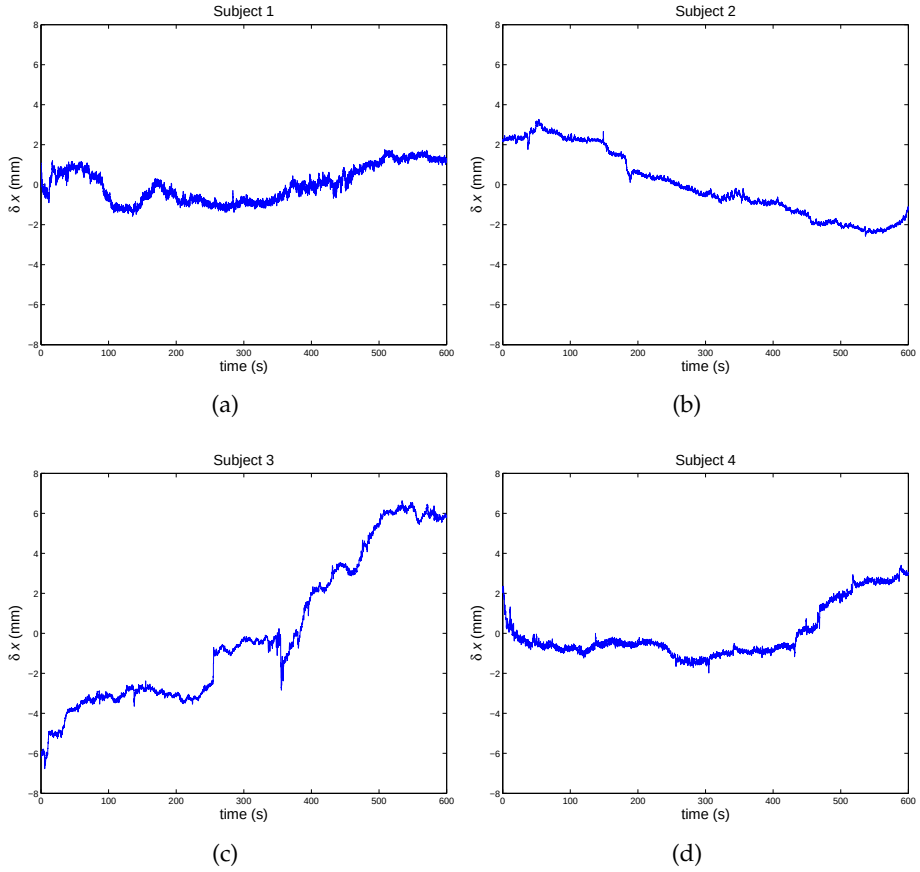

Figure B.3 The x-position of the marker attached to the head of each subject.

Measurements of relative translation in the y-direction, δy, (corresponding to motion in a vertical direction) are shown in Fig. B.4. The range of translation for each subject during the experiment was 2.2 mm, 4.2 mm, 8.8 mm and 6.7 mm for subjects 1–4, respectively. As expected, spikes assumed to be caused by swallowing are obvious in Fig. B.4(d). Apart

from these spikes, and those in Fig. B.4(c), measured motion is generally much less in the y-direction than in the x-direction.

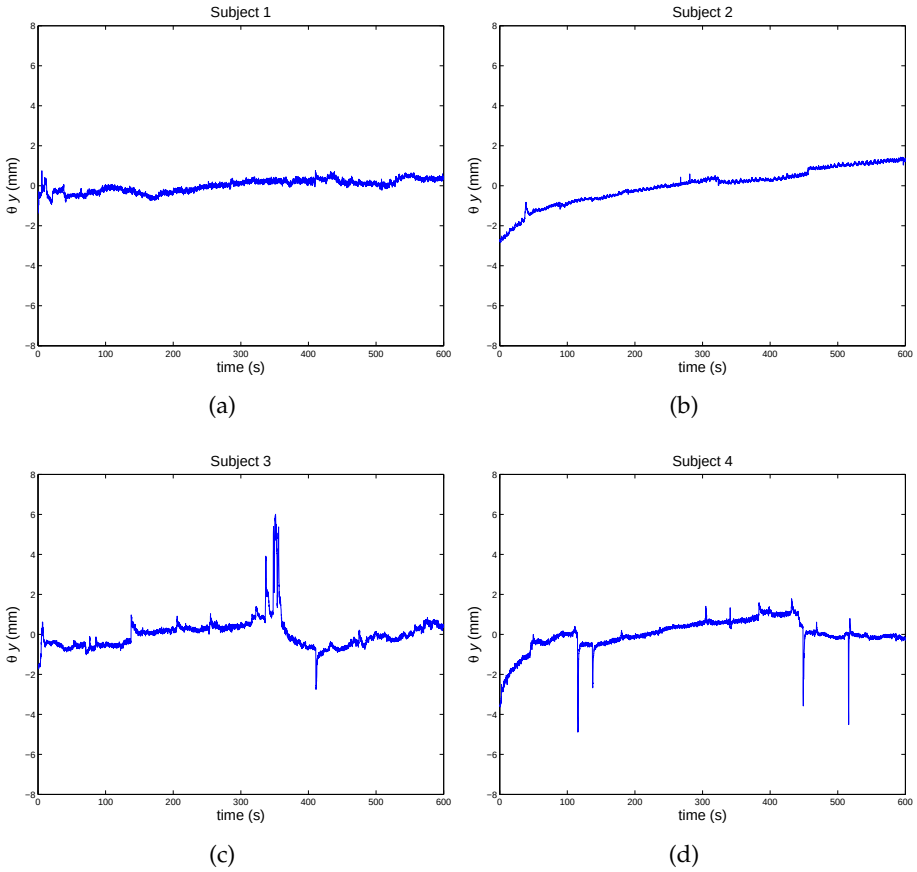

Figure B.4 The y-position of the marker attached to the head of each subject.

The experiment described was simple and easy to perform, yet effectively quantifies in-plane head motion for the four normal volunteers. In future, a means of fastening the marker that does not involve attaching a strap under the jaw should be used. This might avoid the spikes in the recorded data caused by swallowing. The author suggests that instead of using the elastic strap, the marker be attached to a tight rubber swimming cap that can then be worn by the subject.

It would be interesting to repeat the same experiment with stroke or Parkinson's patients, the elderly, or with the neonates discussed in Section 3.1.2. Having done this, the data collected could be analysed to form a statistical model of motion over time. This information could be used directly in TRELLIS to limit the range of estimated rotation or translation between strips using the maximum likely values of motion.

Appendix C

Direct Solution for T2 Blurring Correction

In Section 8.2.2, a method for estimating the modulation of *k*-space data in TRELLIS due to T_2 effects is presented. An alternative direct solution for Eq. (8.6) is derived here. The least squares solution of Eq. (8.6) is given by

$$\mathbf{x} = \left(\mathbf{A}^T\,\mathbf{A}\right)^{-1}\,\mathbf{A}^T\,\mathbf{b}. \tag{C.1}$$

The product $\mathbf{A}^T\,\mathbf{A}$ has a simple form with dimensions $2N \times 2N$, that is,

$$\mathbf{A}^T\,\mathbf{A} = \begin{pmatrix} N & 0 & \cdots & 0 & -1 & -1 & \cdots & -1 \\ 0 & N & \cdots & 0 & -1 & -1 & \cdots & -1 \\ \vdots & \vdots & \ddots & \vdots & \vdots & \vdots & & \vdots \\ 0 & 0 & \cdots & N & -1 & -1 & \cdots & -1 \\ -1 & -1 & \cdots & -1 & N & 0 & \cdots & 0 \\ -1 & -1 & \cdots & -1 & 0 & N & \cdots & 0 \\ \vdots & \vdots & & \vdots & \vdots & \vdots & \ddots & \vdots \\ -1 & -1 & \cdots & -1 & 0 & 0 & \cdots & N \end{pmatrix},$$

which is poorly conditioned because of rank deficiency. A modified version of the system matrix, $\hat{\mathbf{A}}$, which is dimensioned $N^2 \times (2N-1)$ and sets $m_H(1)$ to 1, generates the $(2N-1) \times (2N-1)$ product

$$\hat{\mathbf{A}}^T\,\hat{\mathbf{A}} \;=\; \begin{pmatrix} N & 0 & \cdots & 0 & -1 & -1 & \cdots & -1 \\ 0 & N & \cdots & 0 & -1 & -1 & \cdots & -1 \\ \vdots & \vdots & \ddots & \vdots & \vdots & \vdots & & \vdots \\ 0 & 0 & \cdots & N & -1 & -1 & \cdots & -1 \\ -1 & -1 & \cdots & -1 & N & 0 & \cdots & 0 \\ -1 & -1 & \cdots & -1 & 0 & N & \cdots & 0 \\ \vdots & \vdots & & \vdots & \vdots & \vdots & \ddots & \vdots \\ -1 & -1 & \cdots & -1 & 0 & 0 & \cdots & N \end{pmatrix},$$

which is much better conditioned. By observation, the inverse $\left(\hat{\mathbf{A}}^T\,\hat{\mathbf{A}}\right)^{-1}$ is a close approximation to the form

$$\left(\hat{\mathbf{A}}^T\,\hat{\mathbf{A}}\right)^{-1} \;\cong\; \begin{pmatrix} 2a & a & a & \cdots & \cdots & a & a & a \\ a & 2a & a & \cdots & \cdots & a & a & a \\ \vdots & \vdots & \ddots & & & \vdots & \vdots & \vdots \\ a & a & \cdots & 2a & a & a & \cdots & a \\ b & b & \cdots & b & 2b & b & \cdots & b \\ b & b & \cdots & b & b & 2b & \cdots & b \\ \vdots & \vdots & & \vdots & \vdots & \vdots & \ddots & \vdots \\ b & b & \cdots & b & b & b & \cdots & 2b \end{pmatrix},$$

where $a \cong 1/N$ and $b \cong 1/(N+1)$.

As a result $\mathbf{\Lambda} = \left(\hat{\mathbf{A}}^T\,\hat{\mathbf{A}}\right)^{-1}\,\hat{\mathbf{A}}^T$, of dimension $(2N-1) \times N^2$, also has a relatively simple form,

$$\mathbf{\Lambda} \cong \begin{pmatrix} -a & -a & \cdots & -a & a & a & \cdots & a & 0 & 0 & \cdots & \cdots & 0 & 0 \\ -a & -a & \cdots & -a & 0 & 0 & \cdots & 0 & a & a & \cdots & \cdots & 0 & 0 \\ \vdots & & & & \vdots & & & & & & & & \vdots & \vdots \\ -a & -a & \cdots & -a & 0 & 0 & \cdots & 0 & 0 & 0 & \cdots & \cdots & a & a \\ -2b & -b & \cdots & -b & -b & c & \cdots & c & -b & c & \cdots & \cdots & c & c \\ -b & -2b & \cdots & -b & c & -b & \cdots & c & c & -b & \cdots & \cdots & c & c \\ \vdots & & \ddots & & \vdots & & \ddots & & & & \ddots & & \vdots & \vdots \\ -b & -b & \cdots & -2b & c & c & \cdots & -b & c & c & \cdots & \cdots & c & -b \end{pmatrix},$$

where $c \cong 1/N^2$.

Recalling from Eq. (C.1) that $\mathbf{\Lambda}$ is multiplied by $\mathbf{b}$ to form the least-squares solution, $\mathbf{x}$, a $(2N-1) \times 1$ column vector, and noting from Eq. (8.8) that

$$b_i = \ln(|H(i)|) - \ln(|V(i)|), i \in \Lambda,$$

it can be seen that each element of $\mathbf{x}$ is a weighted average of one or more rows of the $\mathbf{H}$ and $\mathbf{V}$ data sets and therefore

$$x_1 = \frac{1}{N}\left[\sum_{n=1}^{N}\ln(|H(2,n)|) - \sum_{n=1}^{N}\ln(|H(1,n)|) - \sum_{n=1}^{N}\ln(|V(2,n)|) + \sum_{n=1}^{N}\ln(|V(1,n)|)\right]$$

$$x_2 = \frac{1}{N}\left[\sum_{n=1}^{N}\ln(|H(3,n)|) - \sum_{n=1}^{N}\ln(|H(1,n)|) - \sum_{n=1}^{N}\ln(|V(3,n)|) + \sum_{n=1}^{N}\ln(|V(1,n)|)\right]$$

$$x_{N-1} = \frac{1}{N}\left[\sum_{n=1}^{N}\ln(|H(N,n)|) - \sum_{n=1}^{N}\ln(|H(1,n)|) - \sum_{n=1}^{N}\ln(|V(N,n)|) + \sum_{n=1}^{N}\ln(|V(1,n)|)\right]$$

$$\begin{aligned} x_N = \frac{1}{N+1}&\left[\sum_{m=1}^{N}\ln(|V(m,1)|) + \sum_{n=1}^{N}\ln(|V(1,n)|)\right. \\ &\left. - \sum_{m=1}^{N}\ln(|H(m,1)|) - \sum_{n=1}^{N}\ln(|H(1,n)|)\right] \\ &+ \frac{1}{N^2}\left[\sum_{n=1}^{N}\sum_{m=1}^{N}\ln(|H(m,n)|) - \sum_{n=1}^{N}\sum_{m=1}^{N}\ln(|V(m,n)|)\right] \end{aligned}$$

$$\begin{aligned} x_{2N-1} = \frac{1}{N+1}&\left[\sum_{m=1}^{N}\ln(|V(m,N)|) + \sum_{n=1}^{N}\ln(|V(1,n)|)\right. \\ &\left. - \sum_{m=1}^{N}\ln(|H(m,N)|) - \sum_{n=1}^{N}\ln(|H(1,n)|)\right] \\ &+ \frac{1}{N^2}\left[\sum_{n=1}^{N}\sum_{m=1}^{N}\ln(|H(m,n)|) - \sum_{n=1}^{N}\sum_{m=1}^{N}\ln(|V(m,n)|)\right] \end{aligned}$$

This implementation allows the evaluation of Eq. (8.6) in only a few seconds, rather than minutes using MATLAB®'s *lscov* function.

Appendix D

Consent Form and Information Sheet

The following two forms were given to each volunteer before scanning. This was a condition of the ethics committee approval gained for this research.

UNIVERSITY OF CANTERBURY
Te Whare Wānanga o Waitaha
CHRISTCHURCH NEW ZEALAND

Consent Form

Correction of Motion Artifacts in Magnetic Resonance Imaging (MRI)

I have read and I understand the information sheet dated 10/1/06 for volunteers taking part in the study designed to test a technique to help prevent motion artifacts in MRI. I have had the opportunity to discuss this study and am satisfied with the answers I have been given. I have had the opportunity to use the support of family or friends to help me understand this study. I have had time to consider whether to take part.

I understand that taking part in this study is voluntary (my choice), that I may withdraw at any time without giving a reason and that my withdrawal will not affect my future health care, academic progress or employment prospects.

I understand that my participation in this study is confidential and that no material which could identify me will be used in any reports on this study.

I know who to contact if I have any side effects to the study or if I have any questions about the study.

I understand the compensation provisions for this study.

I wish to receive a copy of the results of this study. I am aware that a significant delay may occur between data collection and publication of the results. **YES/NO**

I, _____ (full name), hereby consent to take part in this study.

Signature of participant _____

Date _____

Project explained by _____

Signature _____

Date _____

Names and contact numbers of researchers:

Mr Julian Maclaren
(03) 364 7001 ext. 7118

Dr Richard Watts
(03) 364 2987 ext. 7559

Assoc. Prof. Philip Bones
(03) 364 2987 ext. 7275

Prof. Rick Millane
(03) 364 2987 ext 4918

(*Note: A copy of the consent form to be retained by participant and a copy to be placed on file)*

Version 2, 10/1/06

UNIVERSITY OF CANTERBURY
Te Whare Wānanga o Waitaha
CHRISTCHURCH NEW ZEALAND

Correction of Motion Artifacts in Magnetic Resonance Imaging (MRI)

Investigators: Mr Julian Maclaren, Dr Richard Watts, Assoc. Prof. Philip Bones, Prof. Rick Millane

Version 2: 10/1/06

You are invited to participate in a study to help determine the effectiveness of a motion-correction system for use in MRI. This study will contribute to an academic qualification (the doctoral research of the principal investigator, Mr Julian Maclaren). In order to decide whether you wish to participate, you should understand enough about the possible risks and benefits to make an informed decision.

Introduction

MRI is a valuable tool for diagnosis of a range of medical conditions. However it is a requirement that the patient must hold themselves still during scanning. Obviously this is difficult for some people. A technique has been developed to help solve this problem and we would like to run some preliminary tests to determine its effectiveness.

What will you have to do if you participate in this study?

If you choose to participate in the study you will be required for a period of around 30 minutes to undergo several MRI scans. The exact time and date of the appointment will be made to suit both your schedule and that of the MRI technician whose presence will be required to operate the MRI scanner. During the test you will be placed inside the MRI scanner and for the first scan will be required only to lie still. During the second scan you will be required to move your head slightly in order to generate some motion artifacts in the final image.

Please wear comfortable clothes without metal if possible. You will also need to remove any metallic objects from your person. There is no need to stop medication for the examination, and you may eat and drink normally unless instructed otherwise.

What is involved in an MRI scan?

MRI is a very good means of obtaining detailed images of the body without the use of X-rays. Instead it uses a very powerful magnet and radio waves with similar frequencies to those used by FM radio stations.

You will be asked to lie on our examination bed, which will be raised up and into the magnetic field. You will find yourself in a well-lit, open-ended cylinder just over a metre in length. It remains open at both ends for the entire duration of your scan; however the experience can still be slightly claustrophobic. You will hear a variety of loud noises during the scan but we will provide you with either earphones or earplugs to compensate for this.

What are the possible risks of participating in this study?
MRI is one of the safest medical imaging techniques available and does not involve any radioactive materials or harmful radiation. The only potential danger involved in the scanning procedure arises due to the high magnetic field. This occurs when metallic objects such as a watch or hair clip is worn inside the scanner or if you have a pace-maker or metallic implant. However, before being allowed to enter the scanner, the MRI technicians will inform you of these potential dangers and make sure that you do not take in anything metallic.

Will my results be assessed in any way?
Your scan results will not be assessed by a radiologist in any formal sense.

Compensation
In the unlikely event of a physical injury as a result of your participation in this study, you may be covered by ACC under the Injury Prevention, Rehabilitation and Compensation Act. ACC cover is not automatic and your case will need to be assessed by ACC according to the provisions of the 2002 Injury Prevention Rehabilitation and Compensation Act. If your claim is accepted by ACC, you still might not get any compensation. This depends on a number of factors such as whether you are an earner or non-earner. ACC usually provides only partial reimbursement of costs and expenses and there may be no lump sum compensation payable. There is no cover for mental injury unless it is a result of physical injury. If you have ACC cover, generally this will affect your right to sue the investigators. If you have any questions about ACC, contact your nearest ACC office or the investigator.

Participation
Participation in the study is voluntary (your choice). Your family may be involved in the decision on whether to take part. If you do agree to participate, you are free to withdraw from the project at any stage and do not have to give a reason.

Confidentiality
No material which could personally identify you will be used in any reports on this study. If you would like a copy of your scan in digital form, please mention this at the time of the examination. The data will be stored for a number of years, but no permanent record connecting you to any particular data set will be kept.

Publication of Results
It is expected that the results of the study when completed will appear as an article in a scientific journal. A copy of this article can be sent to you if you wish.

Further Information
For further information you can ask Mr Julian Maclaren (03 3667001 ext. 7118) or Dr Richard Watts (03 364 2987 ext. 7559). If you have any queries or concerns regarding your rights as a participant in this study you may wish to contact a Health and Disability Advocate, telephone (03) 377 7501.

This study has received ethical approval from the Upper South B Ethics Committee.

References

[1] D. W. McRobbie, *MRI from Picture to Proton*. Cambridge, UK ; New York: Cambridge University Press, 2003.

[2] J. P. Hornak, *The Basics of MRI*. Rochester, New York: J. P. Hornak, 2007.

[3] D. G. Nishimura, *Principles of Magnetic Resonance Imaging*. Stanford University: D. G. Nishimura, 1996.

[4] M. A. Bernstein, K. F. King, and X. J. Zhou, *Handbook of MRI Pulse Sequences*. Amsterdam; Boston: Elsevier Academic Press, 2004.

[5] P. Mansfield, "Snapshot magnetic resonance imaging (Nobel Lecture)," *Angewandte Chemie International Edition*, vol. 43, no. 41, pp. 5456–5464, 2004.

[6] Z.-P. Liang and P. C. Lauterbur, *Principles of Magnetic Resonance Imaging: A Signal Processing Perspective*. New York: IEEE Press, 2000.

[7] T. M. Peters, J. C. Williams, and J. H. T. Bates, *The Fourier Transform in Biomedical Engineering*. Boston: Birkhuser, 1998.

[8] F. Bloch, "Nuclear induction," *Physical Review*, vol. 70, no. 7-8, p. 460, 1946.

[9] E. M. Purcell, H. C. Torrey, and R. V. Pound, "Resonance absorption by nuclear magnetic moments in a solid," *Physical Review*, vol. 69, no. 1-2, p. 37, 1946.

[10] I. Young, "Significant events in the development of MRI," *Journal of Magnetic Resonance Imaging*, vol. 20, no. 2, pp. 183–186, 2004.

[11] E. Odeblad, B. N. Bhar, and G. Lindstrom, "Proton magnetic resonance of human red blood cells in heavy-water exchange experiments," *Archives of Biochemistry and Biophysics*, vol. 63, no. 1, pp. 221–225, 1956.

[12] P. C. Lauterbur, "Image formation by induced local interactions: Examples employing nuclear magnetic resonance," *Nature*, vol. 242, no. 5394, pp. 190–191, 1973.

[13] Nobelprize.org, "Press Release: The 2003 Nobel Prize in Physiology or Medicine," 2003.

[14] K. K. Kwong, J. W. Belliveau, D. A. Chesler, I. E. Goldberg, R. M. Weisskoff, B. P. Poncelet, D. N. Kennedy, B. E. Hoppel, M. S. Cohen, R. Turner, H. M. Cheng, T. J. Brady, and B. R. Rosen, "Dynamic magnetic resonance imaging of human brain activity during primary sensory stimulation," *Proceedings of the National Academy of Sciences of the USA*, vol. 89, no. 12, pp. 5675–5679, 1992.

[15] V. A. Diwadkar and M. S. Keshavan, "Newer techniques in magnetic resonance imaging and their potential for neuropsychiatric research," *Journal of Psychosomatic Research*, vol. 53, no. 2, pp. 677–685, 2002.

[16] E. M. Haacke, *Magnetic Resonance Imaging : Physical Principles and Sequence Design*. New York: Wiley, 1999.

[17] T. R. Brown, B. M. Kincaid, and K. Ugurbil, "NMR chemical shift imaging in three dimensions," *Proceedings of the National Academy of Sciences of the USA*, vol. 79, no. 11, pp. 3523–6, 1982.

[18] R. Mir, A. Guesalaga, J. Spiniak, M. Guarini, and P. Irarrazaval, "Fast three-dimensional k-space trajectory design using missile guidance ideas," *Magnetic Resonance in Medicine*, vol. 52, no. 2, pp. 329–336, 2004.

[19] R. Watts, C. Liston, S. Niogi, and A. M. Ulug, "Fiber tracking using magnetic resonance diffusion tensor imaging and its applications to human brain development," *Mental Retardation and Developmental Disabilities Research Reviews*, vol. 9, no. 3, pp. 168–177, 2003.

[20] C. B. Paschal and H. D. Morris, "K-space in the clinic," *Journal of Magnetic Resonance Imaging*, vol. 19, no. 2, pp. 145–159, 2004.

[21] R. N. Bracewell, *The Fourier Transform and Its Applications*, 2nd ed., ser. McGraw-Hill series in electrical engineering. Circuits and systems. New York: McGraw-Hill, 1986.

[22] ——, *Fourier Analysis and Imaging*. New York: Kluwer Academic/Plenum Publishers, 2003.

[23] R. L. Ehman, M. T. McNamara, M. Pallack, H. Hricak, and C. B. Higgins, "Magnetic resonance imaging with respiratory gating: techniques and advantages," *American Journal of Roentgenology*, vol. 143, no. 6, pp. 1175–82, 1984.

[24] D. R. Bailes, D. J. Gilderdale, G. M. Bydder, A. G. Collins, and D. N. Firmin, "Respiratory ordered phase encoding (ROPE): a method for reducing respiratory motion

artefacts in MR imaging," *Journal of Computer Assisted Tomography*, vol. 9, no. 4, pp. 835–8, 1985.

[25] P. Lanzer, C. Barta, E. H. Botvinick, H. U. Wiesendanger, G. Modin, and C. B. Higgins, "ECG-synchronized cardiac MR imaging: method and evaluation," *Radiology*, vol. 155, no. 3, pp. 681–6, 1985.

[26] E. M. Bellon, E. M. Haacke, P. E. Coleman, D. C. Sacco, D. A. Steiger, and R. E. Gangarosa, "MR artifacts: a review," *American Journal of Roentgenology*, vol. 147, no. 6, pp. 1271–81, 1986.

[27] D. Le Bihan, C. Poupon, A. Amadon, and F. Lethimonnier, "Artifacts and pitfalls in diffusion MRI," *Journal of Magnetic Resonance Imaging*, vol. 24, no. 3, pp. 478–488, 2006.

[28] S. Thesen, O. Heid, E. Mueller, and L. R. Schad, "Prospective acquisition correction for head motion with image-based tracking for real-time fMRI," *Magnetic Resonance in Medicine*, vol. 44, no. 3, pp. 457–463, 2000.

[29] J. R. Foster, D. A. Hall, A. Q. Summerfield, A. R. Palmer, and R. W. Bowtell, "Sound-level measurements and calculations of safe noise dosage during EPI at 3 T," *Journal of Magnetic Resonance Imaging*, vol. 12, no. 1, pp. 157–163, 2000.

[30] Y. Hattori, H. Fukatsu, and T. Ishigaki, "Measurement and evaluation of the acoustic noise of a 3 tesla MR scanner," *Nagoya Journal of Medical Science*, vol. 69, no. 1-2, pp. 23–8, 2007.

[31] V. Bettinardi, R. Scardaoni, M. C. Gilardi, G. Rizzo, D. Perani, E. Paulesu, G. Striano, F. Triulzi, and F. Fazio, "Head holder for PET, CT, and MR studies," *Journal of Computer Assisted Tomography*, vol. 15, no. 5, pp. 886–92, 1991.

[32] V. Menon, K. O. Lim, J. H. Anderson, J. Johnson, and A. Pfefferbaum, "Design and efficacy of a head-coil bite bar for reducing movement-related artifacts during functional MRI scanning," *Behavior Research Methods Instruments and Computers*, vol. 29, no. 4, pp. 589–594, 1997.

[33] V. Edward, C. Windischberger, R. Cunnington, M. Erdler, R. Lanzenberger, D. Mayer, W. Endl, and R. Beisteiner, "Quantification of fMRI artifact reduction by a novel plaster cast head holder," *Human Brain Mapping*, vol. 11, no. 3, pp. 207–213, 2000.

[34] S. Malviya, T. Voepel-Lewis, O. P. Eldevik, D. T. Rockwell, J. H. Wong, and A. R. Tait, "Sedation and general anaesthesia in children undergoing MRI and CT: adverse events and outcomes," *British Journal of Anaesthesia*, vol. 84, no. 6, pp. 743–748, 2000.

[35] A. M. Hubbard, R. I. Markowitz, B. Kimmel, M. Kroger, and M. B. Bartko, "Sedation for pediatric patients undergoing CT and MRI," *Journal of Computer Assisted Tomography*, vol. 16, no. 1, pp. 3–6, 1992.

[36] K. J. Slifer, M. F. Cataldo, M. D. Cataldo, A. M. Llorente, and A. C. Gerson, "Behavior analysis of motion control for pediatric neuroimaging," *Journal of Applied Behavior Analysis*, vol. 26, no. 4, pp. 469–470, 1993.

[37] T. Li and S. A. Mirowitz, "Comparative study of fast MR imaging: quantitative analysis on image quality and efficiency among various time frames and contrast behaviors," *Magnetic Resonance Imaging*, vol. 20, no. 6, pp. 471–478, 2002.

[38] J. Hennig, A. Nauerth, and H. Friedburg, "RARE imaging: A fast imaging method for clinical MR," *Magnetic Resonance in Medicine*, vol. 3, no. 6, pp. 823–833, 1986.

[39] P. Mansfield, "Multi-planar image-formation using NMR spin echoes," *Journal of Physics C - Solid State Physics*, vol. 10, no. 3, pp. L55–L58, 1977.

[40] G. E. Sarty, "Single trajectory radial (STAR) imaging," *Magnetic Resonance in Medicine*, vol. 51, no. 3, pp. 445–451, 2004.

[41] J. G. Pipe, "An optimized center-out k-space trajectory for multishot MRI: comparison with spiral and projection reconstruction," *Magnetic Resonance in Medicine*, vol. 42, no. 4, pp. 714–720, 1999.

[42] J. I. Jackson, D. G. Nishimura, and A. Macovski, "Twisting radial lines with application to robust magnetic resonance imaging of irregular flow," *Magnetic Resonance in Medicine*, vol. 25, no. 1, pp. 128–139, 1992.

[43] G. E. Sarty, "Critical sampling in ROSE scanning," *Magnetic Resonance in Medicine*, vol. 44, no. 1, pp. 129–136, 2000.

[44] K. Pandey and D. Noll, "Improved activation detection in fMRI studies using acquisition and reconstruction methods robust to susceptibility and motion artifacts," in *Proceedings of the International Society for Magnetic Resonance in Medicine*, Seattle, 2006, p. 2992.

[45] J. G. Pipe and E. Ahunbay, "Effects of interleaf order for spiral MRI of dynamic processes," *Magnetic Resonance in Medicine*, vol. 41, no. 2, pp. 417–422, 1999.

[46] Y. H. Shu, S. J. Riederer, and M. A. Bernstein, "Three-dimensional MRI with an undersampled spherical shells trajectory," *Magnetic Resonance in Medicine*, vol. 56, no. 3, pp. 553–562, 2006.

[47] E. Ahunbay and J. G. Pipe, "Rapid method for deblurring spiral MR images," *Magnetic Resonance in Medicine*, vol. 44, no. 3, pp. 491–494, 2000.

[48] R. L. Ehman and J. P. Felmlee, "Adaptive technique for high-definition MR imaging of moving structures," *Radiology*, vol. 173, no. 1, pp. 255–263, 1989.

[49] H. W. Korin, J. P. Felmlee, R. L. Ehman, and S. J. Riederer, "Adaptive technique for three-dimensional MR imaging of moving structures," *Radiology*, vol. 177, no. 1, pp. 217–221, 1990.

[50] D. Atkinson and D. L. G. Hill, "Reconstruction after rotational motion," *Magnetic Resonance in Medicine*, vol. 49, pp. 183–187, 2003.

[51] H. Moriguchi, J. S. Lewin, and J. L. Duerk, "Novel interleaved spiral imaging motion correction technique using orbital navigators," *Magnetic Resonance in Medicine*, vol. 50, no. 2, pp. 423–428, 2003.

[52] M. Bydder, D. Atkinson, D. J. Larkman, D. L. G. Hill, and J. V. Hajnal, "SMASH navigators," *Magnetic Resonance in Medicine*, vol. 49, no. 3, pp. 493–500, 2003.

[53] R. Bammer, M. Aksoy, and C. Liu, "Augmented generalized SENSE reconstruction to correct for rigid body motion," *Magnetic Resonance in Medicine*, vol. 57, no. 1, pp. 90–102, 2007.

[54] Y. M. Kadah, A. A. Abaza, A. S. Fahmy, A. B. M. Youssef, K. Heberlein, and X. P. P. Hu, "Floating navigator echo (FNAV) for in-plane 2D translational motion estimation," *Magnetic Resonance in Medicine*, vol. 51, no. 2, pp. 403–407, 2004.

[55] A. F. Costa, D. W. Petrie, Y. F. Yen, and M. Drangova, "Using the axis of rotation of polar navigator echoes to rapidly measure 3D rigid-body motion," *Magnetic Resonance in Medicine*, vol. 53, no. 1, pp. 150–158, 2005.

[56] E. B. Welch, P. J. Rossman, J. P. Felmlee, and A. Manduca, "Self-navigated motion correction using moments of spatial projections in radial MRI," *Magnetic Resonance in Medicine*, vol. 52, no. 2, pp. 337–345, 2004.

[57] J. G. Pipe, "Motion correction with PROPELLER MRI: application to head motion and free-breathing cardiac imaging," *Magnetic Resonance in Medicine*, vol. 42, no. 5, pp. 963–969, 1999.

[58] A. B. Cheryauka, J. N. Lee, A. A. Samsonov, M. Defrise, and G. T. Gullberg, "MRI diffusion tensor reconstruction with PROPELLER data acquisition," *Magnetic Resonance Imaging*, vol. 22, no. 2, pp. 139–148, 2004.

[59] A. A. Tamhane and K. Arfanakis, "Evaluation of in-plane motion correction in PROPELLER-MRI," in *Proceedings of the International Society for Magnetic Resonance in Medicine*, Miami, 2005, p. 2237.

[60] K. P. N. Forbes, J. G. Pipe, C. R. Bird, and J. E. Heiserman, "PROPELLER MRI: clinical testing of a novel technique for quantification and compensation of head motion," *Journal of Magnetic Resonance Imaging*, vol. 14, no. 3, pp. 215–222, 2001.

[61] K. Arfanakis, A. A. Tamhane, J. G. Pipe, and M. A. Anastasio, "K-space undersampling in PROPELLER imaging," *Magnetic Resonance in Medicine*, vol. 53, no. 3, pp. 675–683, 2005.

[62] S. K. Patch, M. Hartley, A. Gaddipati, R. Peters, K. Gould, J. G. Pipe, and K. F. King, "Improved propeller translation correction," in *Proceedings of the International Society for Magnetic Resonance in Medicine*, Miami, 2005, p. 2317.

[63] B. Welch, "Translation first PROPELLER MRI correction," in *Proceedings of the International Society for Magnetic Resonance in Medicine*, Seattle, 2006, p. 3207.

[64] A. Tamhane, J. Pipe, and K. Arfanakis, "PROPELLER and turboprop acquisition parameters for optimal motion correction," in *Proceedings of the International Society for Magnetic Resonance in Medicine*, Seattle, 2006, p. 1037.

[65] J. P. Karis and J. G. Pipe, "ASSET enabled turboprop: an improved PROPELLER sequence for motion-corrected T2 imaging," in *Proceedings of the International Society for Magnetic Resonance in Medicine*, Miami, 2005, p. 2235.

[66] M. Blaimer, K. Barkauskas, S. Kannengiesser, F. Breuer, P. Jakob, J. Duerk, and M. Griswold, "Artifact reduction in undersampled BLADE/PROPELLER MRI by k-space extrapolation using parallel imaging," in *Proceedings of the International Society for Magnetic Resonance in Medicine*, Seattle, 2006, p. 5.

[67] F. N. Wang, T. Y. Huang, F. H. Lin, T. C. Chuang, N. K. Chen, H. W. Chung, C. Y. Chen, and K. K. Kwong, "PROPELLER EPI: An MRI technique suitable for diffusion tensor imaging at high field strength with reduced geometric distortions," *Magnetic Resonance in Medicine*, vol. 54, no. 5, pp. 1232–1240, 2005.

[68] J. G. Pipe and N. Zwart, "Turboprop: improved PROPELLER imaging," *Magnetic Resonance in Medicine*, vol. 55, no. 2, pp. 380–385, 2006.

[69] S. Skare, R. D. Newbould, D. B. Clayton, and R. Bammer, "Propeller EPI in the other direction," *Magnetic Resonance in Medicine*, vol. 55, no. 6, pp. 1298–1307, 2006.

[70] J. G. Pipe, "Motion corrected T1-weighted PROPELLER FSE," in *Proceedings of the International Society for Magnetic Resonance in Medicine*, Miami, 2005, p. 2236.

[71] Y. Feng and W. Chen, "New algorithm for extracting motion information from PROPELLER data and head motion correction in T1-weighted MRI," in *Proceedings of the IEEE Engineering in Medicine and Biology Society*, Shanghai, 2005, pp. 1378–1381.

[72] J. G. Pipe, "Multishot diffusion weighted FSE with PROPELLER," in *Proceedings of the International Society for Magnetic Resonance in Medicine*, Glasgow, 2001, p. 289.

[73] J. G. Pipe, V. G. Farthing, and K. P. Forbes, "Multishot diffusion-weighted FSE using PROPELLER MRI," *Magnetic Resonance in Medicine*, vol. 47, no. 3, pp. 42–52, 2002.

[74] J. Debbins, J. Karis, and J. Pipe, "Advantages of fast spin-echo diffusion weighted imaging in detecting small stroke lesions," in *Proceedings of the International Society for Magnetic Resonance in Medicine*, Seattle, 2006, p. 140.

[75] C. Kunesh and J. Pipe, "Improved sampling density correction for PROPELLER MRI," in *Proceedings of the International Society for Magnetic Resonance in Medicine*, Seattle, 2006, p. 2360.

[76] H. Seo, T. Masui, M. Katayama, K. Satou, N. Yoshizawa, T. Kosugi, and A. Nozaki, "Comparison of PROPELLER fast spin echo, respiratory-triggered fast spin echo and single-shot fast spin echo sequences for transverse T2-weighted magnetic resonance imaging of the female pelvis," in *Proceedings of the International Society for Magnetic Resonance in Medicine*, Miami, 2005, p. 2698.

[77] J. Deng, F. Miller, A. Larson, R. Salem, T. Rhee, D. Li, A. Stemmer, and R. Omary, "Multi-shot diffusion-weighted PROPELLER MRI of the abdomen," in *Proceedings of the International Society for Magnetic Resonance in Medicine*, Seattle, 2006, p. 856.

[78] K. P. Forbes, J. G. Pipe, J. P. Karis, V. Farthing, and J. E. Heiserman, "Brain imaging in the unsedated pediatric patient: comparison of periodically rotated overlapping parallel lines with enhanced reconstruction and single-shot fast spin-echo sequences," *American Journal of Neuroradiology*, vol. 24, no. 5, pp. 796–798, 2003.

[79] S. Chang, M. Hartley, A. Gaddipati, and D. Gui, "Reduced ring artifacts for PROPELLER using an analytical density compensation algorithm during regridding into Cartesian k-space," in *Proceedings of the International Society for Magnetic Resonance in Medicine*, Seattle, 2006, p. 3188.

[80] R. Newbould, R. Bammer, and C. Liu, "Colored noise and effective resolution: data considerations for non-uniform k-space sampling reconstructions," in *Proceedings of the International Society for Magnetic Resonance in Medicine*, Seattle, 2006, p. 2939.

[81] A. Tamhane, K. Arfanakis, and M. Anastasio, "Image noise considerations for PROPELLER k-space sampling," in *Proceedings of the International Society for Magnetic Resonance in Medicine*, Seattle, 2006, p. 1025.

[82] H. Eviatar, J. Saunders, and D. Hoult, "Motion compensation by gradient adjustment," in *Proceedings of the International Society for Magnetic Resonance in Medicine*, Vancouver, 1997, p. 1898.

[83] J. A. Derbyshire, G. A. Wright, R. M. Henkelman, and R. S. Hinks, "Dynamic scan-plane tracking using MR position monitoring," *Journal of Magnetic Resonance Imaging*, vol. 8, no. 4, pp. 924–932, 1998.

[84] H. Eviatar, B. Schattka, J. Sharp, J. Rendell, and M. Alexander, "Real time head motion correction for functional MRI," in *Proceedings of the International Society for Magnetic Resonance in Medicine*, Philadelphia, 1999, p. 269.

[85] A. Peshkovsky, K. H. Knuth, and J. A. Helpern, "Motion correction in MRI using an apparatus for dynamic angular position tracking (ADAPT)," *Magnetic Resonance in Medicine*, vol. 49, no. 1, pp. 138–143, 2003.

[86] M. Guenther and D. A. Feinberg, "Ultrasound-guided MRI: preliminary results using a motion phantom," *Magnetic Resonance in Medicine*, vol. 52, no. 1, pp. 27–32, 2004.

[87] M. Tremblay, F. Tam, and S. J. Graham, "Retrospective coregistration of functional magnetic resonance imaging data using external monitoring," *Magnetic Resonance in Medicine*, vol. 53, no. 1, pp. 141–149, 2005.

[88] M. Zaitsev, C. Dold, G. Sakas, J. Hennig, and O. Speck, "Magnetic resonance imaging of freely moving objects: prospective real-time motion correction using an external optical motion tracking system," *Neuroimage*, vol. 31, no. 3, pp. 1038–1050, 2006.

[89] C. Dold, M. Zaitsev, O. Speck, E. A. Firle, J. Hennig, and G. Sakas, "Advantages and limitations of prospective head motion compensation for MRI using an optical motion tracking device," *Academic Radiology*, vol. 13, no. 9, pp. 1093–1103, 2006.

[90] M. Kanowski, J. W. Rieger, T. Noesselt, C. Tempelmann, and H. Hinrichs, "Endoscopic eye tracking system for fMRI," *Journal of Neuroscience Methods*, vol. 160, no. 1, pp. 10–15, 2007.

[91] W. F. Yang and M. R. Smith, "Using an MRI distortion transfer function to characterize the ghosts in motion-corrupted images," *IEEE Transactions on Medical Imaging*, vol. 19, no. 6, pp. 577–584, 2000.

[92] M. E. Bourgeois, F. T. A. W. Wajer, M. Roth, A. Briguet, M. Decorps, D. v. Ormondt, C. Segebarth, and D. Graveron-Demilly, "Retrospective intra-scan motion correction," *Journal of Magnetic Resonance*, vol. 163, no. 2, pp. 277–287, 2003.

[93] D. Atkinson, D. L. G. Hill, P. N. R. Stoyle, P. E. Summers, S. Clare, R. Bowtell, and S. F. Keevil, "Automatic compensation of motion artifacts in MRI," *Magnetic Resonance in Medicine*, vol. 41, no. 1, pp. 163–170, 1999.

[94] D. Atkinson, D. J. Larkman, P. G. Batchelor, D. L. G. Hill, and J. V. Hajnal, "Coil-based artifact reduction," *Magnetic Resonance in Medicine*, vol. 52, no. 4, pp. 825–830, 2004.

[95] P. G. Batchelor, D. Atkinson, P. Irarrazaval, D. L. G. Hill, J. Hajnal, and D. Larkman, "Matrix description of general motion correction applied to multishot images," *Magnetic Resonance in Medicine*, vol. 54, no. 5, pp. 1273–1280, 2005.

[96] L. A. Shepp and B. F. Logan, "Fourier reconstruction of a head section," *IEEE Transactions on Nuclear Science*, vol. NS21, no. 3, pp. 21–43, 1974.

[97] S. Pan and A. Kak, "A computational study of reconstruction algorithms for diffraction tomography: interpolation versus filtered-backpropagation," *IEEE Transactions on Acoustics, Speech, and Signal Processing*, vol. 31, no. 5, pp. 1262–1275, 1983.

[98] N. D. Blakeley, "Sampling strategies and reconstruction techniques for magnetic resonance imaging : a thesis presented for the degree of Doctor of Philosophy," Ph.D. dissertation, University of Canterbury, 2003.

[99] Y. Abe, Y. Yamashita, Y. Tang, T. Namimoto, and M. Takahashi, "Calculation of T2 relaxation time from ultrafast single shot sequences for differentiation of liver tumors: comparison of echo-planar, HASTE, and spin-echo sequences," *Radiation Medicine*, vol. 18, pp. 7–14, 2000.

[100] R. Archibald and A. Gelb, "A method to reduce the Gibbs ringing artifact in MRI scans while keeping tissue boundary integrity," *IEEE Transactions on Medical Imaging*, vol. 21, no. 4, pp. 305–319, 2002.

[101] M. Drangova, B. Bowman, and N. J. Pelc, "Physiologic motion phantom for MRI applications," *Journal of Magnetic Resonance Imaging*, vol. 6, no. 3, pp. 513–518, 1996.

[102] G. Leung and D. B. Plewes, "Retrospective motion compensation using variable-density spiral trajectories," *Journal of Magnetic Resonance Imaging*, vol. 22, no. 3, pp. 373–380, 2005.

[103] M. E. Huber, M. Stuber, R. M. Botnar, P. Boesiger, and W. J. Manning, "Low-cost MR-compatible moving heart phantom," *Journal of Cardiovascular Magnetic Resonance*, vol. 2, no. 3, pp. 181–187, 2000.

[104] A. J. W. van der Kouwe, T. Benner, and A. M. Dale, "Real-time rigid body motion correction and shimming using cloverleaf navigators," *Magnetic Resonance in Medicine*, vol. 56, no. 5, pp. 1019–1032, 2006.

[105] P. J. Bones, J. R. Maclaren, R. P. Millane, and R. Watts, "Quantifying and correcting motion artifacts in MRI," in *SPIE: Image Reconstruction from Incomplete Data IV*, vol. 6316. SPIE, 2006, pp. 6316–08.

[106] K. P. N. Forbes, J. G. Pipe, C. R. Bird, and J. E. Heiserman, "PROPELLER MRI: clinical testing of a novel technique for quantification and compensation of head motion,"

in *Proceedings of the International Society for Magnetic Resonance in Medicine*, Glasgow, 2001, p. 289.

[107] D. Atkinson, D. L. G. Hill, P. N. R. Stoyle, P. E. Summers, and S. F. Keevil, "Automatic correction of motion artifacts in magnetic resonance images using an entropy focus criterion," *IEEE Transactions on Medical Imaging*, vol. 16, no. 6, pp. 903–910, 1997.

[108] Z. Wang and A. C. Bovik, "A universal image quality index," *IEEE Signal Processing Letters*, vol. 9, no. 3, pp. 81–84, 2002.

[109] Z. Wang, A. C. Bovik, H. R. Sheikh, and E. P. Simoncelli, "Image quality assessment: from error visibility to structural similarity," *IEEE Transactions on Image Processing*, vol. 13, no. 4, pp. 600–612, 2004.

[110] A. Armstrong, S. Beesley, C. Grecos, and D. Parish, " Directionally sensitive bilinear concealment for H264," in *Proceedings of the Fifth IASTED International Conference on Visualization, Imaging and Image Processing*, Benidorm, 2005, pp. 304–308.

[111] P. Marziliano, F. Dufaux, S. Winkler, and T. Ebrahimi, "A no-reference perceptual blur metric," in *Proceedings of the IEEE International Conference on Image Processing*, vol. 3, 2002, pp. 57–60.

[112] J. Canny, "A computational approach to edge-detection," *IEEE Transactions on Pattern Analysis and Machine Intelligence*, vol. 8, no. 6, pp. 679–698, 1986.

[113] J. R. Maclaren, P. J. Bones, R. P. Millane, and R. Watts, "MRI with TRELLIS: A novel approach to motion correction," *Magnetic Resonance Imaging*, in press.

[114] P. J. Bones and J. R. Maclaren, "Improved bulk rotation detection and correction in MRI," in *Proceedings of the IEEE Engineering in Medicine and Biology Society*, Lyon, 2007, pp. 2106–2109.

[115] J. Maclaren, P. Bones, R. Millane, and R. Watts, "TRELLIS MRI: a novel approach to motion correction," in *Proceedings of the International Society for Magnetic Resonance in Medicine*, Seattle, 2006, p. 3194.

[116] L. E. Ghaoui and H. Lebret, "Robust solutions to least-squares problems with uncertain data," *SIAM J. Matrix Anal. Appl.*, vol. 18, no. 4, pp. 1035–1064, 1997.

[117] J. Maclaren, P. Bones, R. Millane, and R. Watts, "Correction of translational motion artifacts in magnetic resonance imaging," in *Proceedings of the Fifth IASTED International Conference on Visualization, Imaging, and Image Processing*, Benidorm, 2005, pp. 448–452.

[118] ——, "Correcting motion artifacts in magnetic resonance images," in *Proceedings of Image and Vision Computing New Zealand*, Dunedin, 2005, pp. 120–125.

[119] P. Bones, J. Maclaren, R. Millane, and R. Watts, "An extension to the phase-correlation method applied to MRI motion correction," in *Australasian Physical and Engineering Sciences in Medicine*, vol. 28(4), Adelaide, 2005, p. 286.

[120] D. C. Ghiglia and M. D. Pritt, *Two-Dimensional Phase Unwrapping: Theory, Algorithms, and Software*. New York: Wiley, 1998.

[121] C. D. Kuglin and D. C. Hines, "The phase correlation image alignment method," in *Proceedings of the IEEE International Conference on Cybernetics and Society*, 1975, pp. 163–165.

[122] Q. X. Wu, P. J. Bones, and R. H. T. Bates, "Translational motion compensation for coronary angiogram sequences," *IEEE Transactions on Medical Imaging*, vol. 8, no. 3, pp. 276–282, 1989.

[123] B. Wilson, P. Bones, and R. Jones, "Weighted phase-correlation," in *Proceedings of Image and Vision Computing New Zealand*, Palmerston North, 1994, pp. 1.8.1 – 1.8.8.

[124] Y. L. Zhang, J. Yang, H. T. Wu, and Y. F. Xue, "Phase-correlation based registration of swipe fingerprints," in *Advances in Biometric Person Authentication, Proceedings*, ser. Lecture Notes in Computer Science, 2004, vol. 3338, pp. 506–515.

[125] J. G. Pipe and P. Menon, "Sampling density compensation in MRI: rationale and an iterative numerical solution," *Magnetic Resonance in Medicine*, vol. 41, no. 1, pp. 179–186, 1999.

[126] J. G. Pipe, "Reconstructing MR images from undersampled data: data-weighting considerations," *Magnetic Resonance in Medicine*, vol. 43, no. 6, pp. 867–875, 2000.

[127] R. E. Gabr, P. Aksit, P. A. Bottomley, A. M. Youssef, and Y. M. Kadah, "Deconvolution-interpolation gridding (DING): accurate reconstruction for arbitrary k-space trajectories," *Magnetic Resonance in Medicine*, vol. 56, no. 6, pp. 1182–1191, 2006.

[128] R. M. Henkelman, "Measurement of signal intensities in the presence of noise in MR Images," *Medical Physics*, vol. 12, no. 2, pp. 232–233, 1985.

[129] W. A. Edelstein, G. H. Glover, C. J. Hardy, and R. W. Redington, "The intrinsic signal-to-noise ratio in NMR imaging," *Magnetic Resonance in Medicine*, vol. 3, no. 4, pp. 604–618, 1986.

[130] R. Watts and Y. Wang, "K-space Interpretation of the Rose model: noise limitation on the detectable resolution in MRI," *Magnetic Resonance in Medicine*, vol. 48, no. 3, pp. 550–554, 2002.

[131] J. Maclaren, P. Bones, R. Millane, and R. Watts, "TRELLIS motion correction: initial results in vivo," in *Proceedings of the International Society for Magnetic Resonance in Medicine*, Berlin, 2007, p. 3426.

[132] H. Chen, H. Avram, L. Kaufman, J. Hale, and D. Kramer, "T2 restoration and noise suppression of hybrid MR images using Wiener and linear prediction techniques," *IEEE Transactions on Medical Imaging*, vol. 13, no. 4, pp. 667–676, 1994.

[133] K. Oshio and M. Singh, "Correction of T2 distortion in multi-excitation RARE sequence," *IEEE Transactions on Medical Imaging*, vol. 11, no. 1, pp. 123–128, 1992.

[134] H. Takahashi, K. Ogawa, K. Oshio, and H. Momoshima, "A proposal of removal method for T2 decay effects in RARE sequence," *IEEE Transactions on Nuclear Science*, vol. 42, no. 4, pp. 1343–1347, 1995.

[135] K. Oshio and D. A. Feinberg, "GRASE (Gradient-and Spin-Echo) imaging: a novel fast MRI technique," *Magnetic Resonance in Medicine*, vol. 20, no. 2, pp. 344–349, 1991.

[136] J. R. Maclaren, P. J. Bones, R. P. Millane, and R. Watts, "A modified view ordering for artifact reduction in MRI," in *Proceedings of the IEEE Engineering in Medicine and Biology Society*, Lyon, 2007, pp. 2053–2056.

[137] T. D. Nguyen, G. Ding, R. Watts, and Y. Wang, "Optimization of view ordering for motion artifact suppression," *Magnetic Resonance Imaging*, vol. 19, no. 7, pp. 951–957, 2001.

[138] D. K. Sodickson and W. J. Manning, "Simultaneous acquisition of spatial harmonics (SMASH): fast imaging with radiofrequency coil arrays," *Magnetic Resonance in Medicine*, vol. 38, no. 4, pp. 591–603, 1997.

[139] K. P. Pruessmann, M. Weiger, M. B. Scheidegger, and P. Boesiger, "SENSE: sensitivity encoding for fast MRI," *Magnetic Resonance in Medicine*, vol. 42, no. 5, pp. 952–962, 1999.

[140] M. Bydder, D. J. Larkman, and J. V. Hajnal, "Detection and elimination of motion artifacts by regeneration of k-space," *Magnetic Resonance in Medicine*, vol. 47, no. 4, pp. 677–686, 2002.

[141] R. Bammer, C. Liu, and M. Aksoy, "Improving rigid head motion correction using parallel imaging," in *Proceedings of the International Society for Magnetic Resonance in Medicine*, Seattle, 2006, p. 8.

[142] N. Chen, Y. Chou, and L. Panych, "Identification and correction of the intra-scan motion artifact using parallel imaging," in *Proceedings of the International Society for Magnetic Resonance in Medicine*, Seattle, 2006, p. 3202.

[143] M. A. Griswold, P. M. Jakob, R. M. Heidemann, M. Nittka, V. Jellus, J. Wang, B. Kiefer, and A. Haase, "Generalized autocalibrating partially parallel acquisitions (GRAPPA)," *Magnetic Resonance in Medicine*, vol. 47, no. 6, pp. 1202–1210, 2002.

[144] M. S. Atkins and M. Menke, "Effects of head movements measured during PET scans," in *IEEE Nuclear Science Symposium and Medical Imaging Conference Record*, vol. 3, 1995, pp. 1776–1780.

[145] E. Seto, G. Sela, W. E. McIlroy, S. E. Black, W. R. Staines, M. J. Bronskill, A. R. McIntosh, and S. J. Graham, "Quantifying head motion associated with motor tasks used in fMRI," *Neuroimage*, vol. 14, no. 2, pp. 284–297, 2001.

[146] M. Porer, "Development of an MRI-compatible head motion tracking system," University of Canterbury, PHYS493 Project Report, 21 Feb. 2007.